THE INFLUENCE OF HIGH ELECTRIC FIELDS ON WATER AND METHANOL SURFACE ELECTROCHEMISTRY

by

Christopher John Rothfuss

A dissertation submitted in partial fulfillment
of the requirements for the degree of

Doctor of Philosophy

University of Washington

2002

Program Authorized to Offer Degree:
Department of Chemical Engineering

University of Washington
Graduate School

This is to certify that I have examined this copy of a doctoral dissertation by

Christopher John Rothfuss

and have found that it is complete and satisfactory in all respects,
and that any and all revisions required by the final
examining committee have been made.

Chair of Supervisory Committee:

_____
Eric M. Stuve

Reading Committee:

_____
Eric M. Stuve

_____
Sam C. Fain

_____
Bruce D. Kay

Date: _____

In presenting this dissertation in partial fulfillment of the requirements for the doctoral degree at the University of Washington, I agree that the Library shall make its copies freely available for inspection. I further agree that extensive copying of the dissertation is allowable only for scholarly purposes, consistent with "fair use" as prescribed in the U.S. Copyright Law. Requests for copying or reproduction of this dissertation may be referred to Proquest Information and Learning, 300 North Zeeb Road, Ann Arbor, MI 48106-1346, to whom the author has granted "the right to reproduce and sell (a) copies of the manuscript in microform and/or (b) printed copies of the manuscript made from microform."

Signature_____

Date_____

University of Washington

Abstract

THE INFLUENCE OF HIGH ELECTRIC FIELDS ON WATER AND METHANOL SURFACE ELECTROCHEMISTRY

by

Christopher John Rothfuss

Chairperson of the Supervisory Committee: Professor Eric M. Stuve
Department of Chemical Engineering

Understanding the behavior of molecules in high electric fields, particularly near catalyst surfaces, is of fundamental importance to electrochemistry and high field surface chemistry. This study focuses on the behavior of water and methanol molecules adsorbed on a Pt emitter tip in high fields (~1 V/Å) and provides further understanding of dissociation and ion cluster emission. Mass resolved ramped field desorption (RFD) experiments from field adsorbed water layers on Pt have provided field dependencies of specific ion cluster masses for temperatures ranging from 170 to 300 K. Isothermal RFDs showed that as the field increased, water ion clusters $H^+(H_2O)_n$ were emitted, beginning with large n clusters (up to 7) and proceeding through each lower n cluster. The onset field depended on the value of n (lower for higher n), but was relatively independent of temperature; however, ion signal intensity was temperature dependent. Constant field, cyclical temperature experiments provided Arrhenius graphs showing thermal deactivation energies for ion emission from the tip. The observed deactivation corresponds to the thermal desorption of the nth solvating water molecule of the ion cluster with energies of 0.85 eV, 0.76 eV and 0.55 eV for n = 3, 4 and 5, respectively. For RFD experiments with ice, all observed $H^+(H_2O)_n$ ions appeared simultaneously in a flash at a critical onset field, demonstrating a common limiting step. The onset of ionization occurred at a higher field for

109 K RFDs (0.44 V/Å) than for 145 K RFDs (0.32 V/ Å). However, clusters n = 2 and 3, which were dominant at 109 K, were not observed at 145 K. Results suggest a two step dissociative ionization/desorption mechanism in which the strongly temperature dependent dissociative ionization event determines emission onset at low temperatures, while the field dependent ion emission event determines emission onset at higher temperatures. Pulsed time of flight mass spectrometry of field adsorbed water / methanol layers at 165 K demonstrated analogous behavior to the pure water system, but with richer spectra, particularly near mass 33. $H^+(CH_3OH)_m$ clusters were observed for m up to 4. Mixed $H^+(CH_3OH)_m(H_2O)_n$ clusters were also observed.

TABLE OF CONTENTS

TABLE OF CONTENTS i
LIST OF FIGURES iii
LIST OF TABLES v
CHAPTER 1: INTRODUCTION 1
CHAPTER 2: EXPERIMENTAL THEORY 5
2.1 Emitter Tips 5
2.1.1 Characteristics 5
2.1.2 Tip Preparation 6
2.2 Field Emission 7
2.3 Field Ionization 10
2.4 Field Ionization and Desorption Spectrometry 15
2.4.1 ExB Mass Resolution (Wien Filter) 15
2.4.2 Pulsed Time of Flight Mass Spectrometry 18
CHAPTER 3: LITERATURE REVIEW 27
3.1 Water 27
3.1.1 Properties and Phase Behavior 27
3.1.2 Dissociation and Ionization of Water Molecules 30
3.1.3 Protonated Water Clusters 31
3.2 Water / Methanol Systems 33
3.3 Field Emitter Studies 34
CHAPTER 4: EXPERIMENTAL APPARTUS 38
4.1 Ultra High Vacuum Chamber 38
4.2 Tip Assembly 39
4.3 Einzel Lens Assembly 39
4.4 Gas Handling System 40
4.5 Wien Filter Ion Characterization 41
4.6 Time Of Flight 42
CHAPTER 5: ION CLUSTER EMISSION FROM FIELD ADSORBED WATER LAYERS ON PLATINUM 49
5.1 Experimental Procedure 49
5.1.1 Full Spectrum Ramped Field Ionization and Desorption 50
5.1.2 Mass Selected Ramped Field Ionization and Desorption 51
5.1.3 Mass Selected Field Ionization and Desorption with Temperature Cycling 52
5.2 Results 52
5.3 Discussion 55
5.3.1 Ion Cluster Emission 55
5.3.2 Temperature Dependence and Solvation Energy 59
5.4 Conclusions 68

CHAPTER 6: TWO STEP ION CLUSTER DISSOCIATION AND EMISSION 79
6.1 Experimental Procedure 81
6.1.1 Low Temperature Mass Selected Ramped Field Desorption (RFD) ... 82
6.1.2 Direct Ion Imaging 83
6.1.3 Step Desorption Cycles 83
6.2 Results 84
6.3 Discussion 86
6.3.1 Mass Selected Ramped Field Ionization and Desorption of Ice Layers 86
6.3.2 Direct Imaging of Water Ion Cluster Formation 88
6.3.3 The Importance of Solvation 89
6.3.4 Water Ion Cluster Field Emission Mechanism 91
6.3.5 Notes on Low Temperature Cluster Formation 91
6.4 Conclusions 93
CHAPTER 7: FIELD EMISSION OF METHANOL AND WATER / METHANOL MIXTURES 101
7.1 Experimental Procedure 102
7.2 Results 103
7.3 Discussion 105
7.3.1 Ion Cluster Emission Behavior 106
7.3.2 Mass 19 Enhancement 110
7.3.3 Ion Mass Substructure 111
7.3.3 Mass 32 / 33 Ratio 114
7.4 Conclusions 115
CHAPTER 8: UHV SOLID OXID FUEL CELL STUDIES 127
8.1 Technical Approach 127
8.1.1 Field Ionization System 129
8.1.2 UHV SOFC System 130
8.2 Developmental Progress 130
8.2.1 Field Ionization System 130
8.2.2 UHV SOFC System 133
CHAPTER 9: CONCLUDING REMARKS 145
9.1 Summary of Results 145
9.2 Conclusions 148
BIBLIOGRAPHY 154

LIST OF FIGURES

Figure 1- 1: Direct methanol fuel cell. 4
Figure 2- 1: Emitter tip schematic. 19
Figure 2- 2: Field effect on electron emission barrier. 20
Figure 2- 3: Field emission microscope. 21
Figure 2- 4: Experimental images of a Pt(111) oriented field emitter tip. 22
Figure 2- 5: Field ion microscope method of operation..... 23
Figure 2- 6: Field ionization mechanism. 24
Figure 2- 7: Wien filter operating principles. 25
Figure 2- 8: Wien filter separation of mass 19 and mass 37 protonated water clusters..... 26
Figure 4- 1: Experimental UHV chamber setup. 44
Figure 4- 2: Schematic of experimental system. 45
Figure 4- 3: Pt emitter tip assembly. 46
Figure 4- 4: Einzel lens schematic. 47
Figure 4- 5: Wien filter and lens apparatus. 48
Figure 5- 1: Onset of ionization for ramped field desorption of water from Pt emitter tip by temperature..... 70
Figure 5- 2: Mass selected ramped field cluster formation. 71
Figure 5- 3: Mass resolved ramped field ionization of $H^+(H_2O)_4$ for temperatures 180 K to 230 K..... 72
Figure 5- 4: Typical ion cluster formation dependency during temperature cycling. 73
Figure 5- 5: Arrhenius plot of cluster ion formation during temperature cycling demonstrating thermal deactivation of the cluster emission..... 74
Figure 5- 6: Mass resolved ramped field desorption of oxygen from Pt emitter tips for temperatures 180 K through 300 K. 75
Figure 5- 7: Field bending of potential energy barriers to ion cluster emission. 76
Figure 5- 8: Reaction pathways and energies. 77
Figure 6- 1: Previous protonated water cluster emission results. 95
Figure 6- 2: Mass selected ramped field desorption (RFD) of ice layers from a Pt field emitter tip. 96
Figure 6- 3: Field ion micrographs of protonated water cluster H+(H2O)n emission at 180 K and 230 K for a variety of fields selected for favoring particular clusters types..... 97
Figure 6- 4: Step desorption of water clusters from thick ice layers on Pt tip. 98
Figure 6- 5: A comparison of three ramped field desorptions. 99
Figure 6- 6: Idealized model of 2 step ionization / emission mechanism. 100
Figure 7- 1: Wien filter separation of water, methanol and water / methanol ion clusters. 117
Figure 7- 2: Pulsed ToF spectroscopy of protonated methanol clusters. 118

Figure 7- 3: Pulsed ToF spectroscopy of mixed water / methanol clusters. .. 119
Figure 7- 4: Mass complexity near m = 1 protonated methanol cluster. 120
Figure 7- 5: Mass to charge substructure near mass 35. 121
Figure 8- 1: Pt / Oxide / Catalyst emitter tip design. 135
Figure 8- 2: Source assembly schematic for cerium and copper or lithium source. 136
Figure 8- 3: Images of source assembly mounted in vacuum chamber. 137
Figure 8- 4: Source designs. 138
Figure 8- 5: Micrographs depicting cerium deposition on Pt (111) tip. 139
Figure 8- 6: Fowler-Nordheim plot for calculation the change in work function after ceria deposition. 140
Figure 8- 7: Field ion micrographs depicting ceria coating on Pt tip. 141
Figure 8- 8: UHV SOFC macor support apparatus schematic. 142
Figure 8- 9: Top view of SOFC support apparatus. 143
Figure 8- 10: Front view of macor SOFC support apparatus. 144

LIST OF TABLES

Table 5- 1: Ion cluster energies and observed formation fields. 78
Table 7- 1: Ion cluster emission energies for protonated methanol clusters.. 122
Table 7- 2: Excess emission energy Xm,n for protonated water / methanol clusters. 123
Table 7- 3: Possible ions near mass 32. 124
Table 7- 4: Ion count ratio for masses 32 and 33 as a function of pulse height VP. 125
Table 7- 5: Ion count ratio for masses 32 and 33 as a function of MeOH to H2O ratio. 126

ACKNOWLEDGEMENTS

I would like to thank my advisor, Dr. Eric Stuve, for all of his help and guidance over the last four years. I have greatly enjoyed working with him and being a member of his research group. I have learned a great deal and laughed a great deal with him over the years, and greatly appreciate the opportunity.

I would also like to extend my appreciation to my PhD committee members: Dr. Frank Turecek, Dr. Shaoyi Jiang, Dr. Bruce Kay, and Dr. Samuel Fain for supervising my research, and helping me with this dissertation work over the last few years. Dr. Valentin Medvedev has been an incredible resource and a good friend while at UW. I greatly appreciate all of the help and instruction I have received from him. I would also like to thank the rest of my research group, present and past, for their help and thoughtful discussions and Dave Gery who was instrumental in the design and fabrication of the experimental equipment

I would also like to thank the US Office of Naval Research for funding my research and education at the University of Washington.

Finally, I would like to thank my family and my Heather for the countless things I should be thanking them for, but can't possibly list on this page.

CHAPTER 1: INTRODUCTION

The motivation behind this research is to study the behavior of water and methanol in high electric fields. This is of particular interest to our research because of our work on direct methanol fuel cells. A direct methanol fuel cell (shown in Figure 1-1) operates by bringing together water and methanol at the anode side of the cell, which typically contains platinum and ruthenium catalyst. The methanol and water react to produce carbon dioxide, protons and electrons.

$$CH_3OH + H_2O \rightarrow CO_2 + 6H^+ + 6e^- \qquad (1.1)$$

The protons then travel through a proton exchange membrane where they recombine with oxygen and electrons at the cathode (typically contains platinum catalyst) to produce water.

$$3/2\,O_2 + 6H^+ + 6e^- \rightarrow 3H_2O \qquad (1.2)$$

The electron transfer between the anode and cathode can be used to drive a load.

A better understanding of the behavior of water and methanol at the anode surface will be useful in improving the efficiency of the fuel cell. Very near the anode surface (or the cathode), the charge incongruity between the bulk electrolyte and the anode is screened over a very short distance. This screening region is called the electrochemical double layer. Since the potential difference is screened over a very short distance (nanometer scale), the

resulting field is very high, on the order of a volt / ångstrom[1-4]. This field is sufficient for breaking and making bonds and helps to drive the electrochemical reactions. Dissociative ionization of water is fundamental to electrochemistry and is known to be influenced by electric field.

Traditional approaches to studying electrochemical systems have been primarily at the macroscopic level. These include such techniques as cyclic voltammetry, potential step measurements, stripping voltammetry, etc. While often thought of as a continuous, one dimensional feature, the field in the electrochemical double layer is actually quite dynamic and inhomogeneous due to finite size effects of the electrolyte molecules. Unfortunately, directly probing the characteristics of this double layer is quite difficult. Understanding the role of surface electric fields in electrochemistry has been of theoretical interest for a number of years [1-3]. However, experimental studies of the role of surface electric fields are quite few, due in large part to the difficulty of generating such high fields in a reproducible fashion. Planar electrodes, for example, would require a potential difference of 10,000 V across two electrodes spaced 1 μm apart to produce a field of 1 V/Å. Even if the dielectric medium between the two electrodes could withstand such a field (or one had a perfect vacuum), the coulombic attraction between the two electrodes would result in them collapsing upon themselves, regardless of their supports.

Instead, the methodology of ultrahigh vacuum (UHV) double layer modeling was developed to provide information about electrode/electrolyte

interface phenomena[5-7]. This methodology consists of adsorbing relevant electrochemical species on a metal substrate in vacuum to mimic the electrode/electrolyte interface. A number of publications have shown the close relationship of these experiments in simulating the charging of an electrode surface[4, 7-11]. The problem of obtaining high fields is easily overcome using emitter tips. Emitter tips produce fields on the order of several V/Å, up to the limit of the structural integrity of the tip. Field emitter tips provide a small controlled arena for analyzing high field chemical reactions, solvation energies, field induced migration and fundamental chemical properties of adsorbed chemical species under ultra-high vacuum (UHV) conditions.

This study of ion cluster formation and emission from a Pt emitter tip employs pulsed time of flight (ToF) mass spectrometry, Wien filter mass resolution during continuous mode ion emission, and field ion microscopy (FIM) to investigate the behavior of water, methanol and water/methanol mixtures in high fields on a Pt surface. Experimental studies of protons and hydroxyl groups in high fields near surfaces provide insight into the properties of the electrochemical double layer and help to describe in better detail the behavior of ionic species in high fields.

In addition to studies of protonated ion cluster formation and emission, new experimental equipment and techniques have been developed to provide insight into high field surface electrochemistry and electrocatalysis in systems modeled after solid oxide fuel cells (SOFCs).

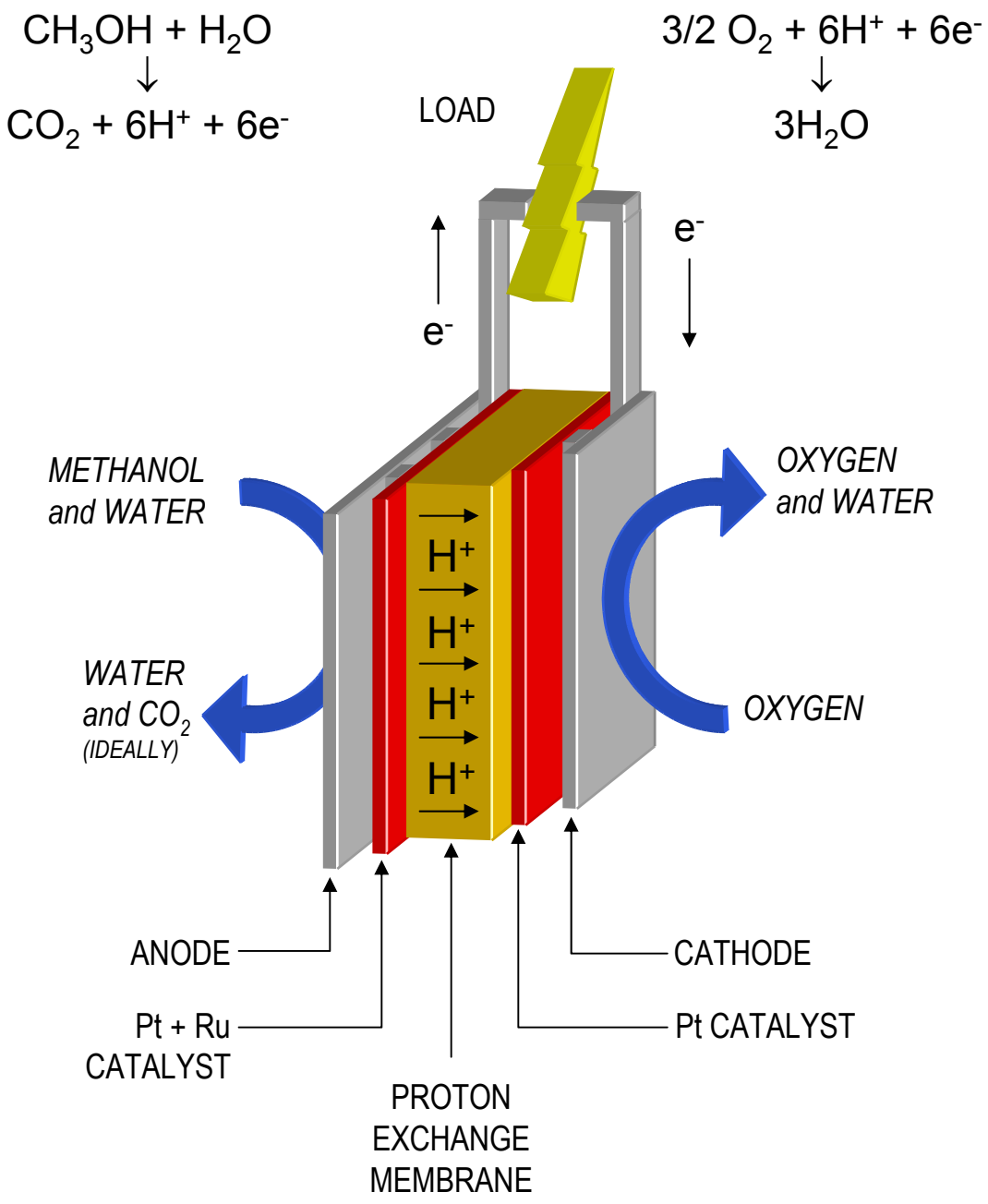

FIGURE 1-1: Direct methanol fuel cell.

CHAPTER 2: EXPERIMENTAL THEORY

2.1 Emitter Tips

The application of high fields is essential to numerous technologies and experimental studies. Since an electric field represents the change of electrical potential with a change in distance, generating high fields requires either very high potentials, or a very small length scale for the change in potential. The latter is easily obtained using emitter tips, allowing fields on the order of one to several V / Å to be obtained at potentials of only a few kV.

Field emitter tips (Figure 2-1) are widely used to produce high local fields for a variety of applications including low temperature cathodes, for field emitter arrays; work function studies using field emission microscopy (FEM)[11]; surface structural analysis through field ion microscopy (FIM)[12]; determining bulk properties and composition through atom probe tomography[13]; and for studying high field surface chemistry with field desorption and field ionization mass spectrometry[12, 14]. Scanning tunneling microscopes employ extremely sharp emitter tips for scanning, often with tip apexes of only a single atom.

2.1.1 Characteristics

Emitter tips are generally sharp needles or whiskers with hemispherical apexes having radii on the order of a few hundred Ångstroms. They are typically made of conductive or semi-conductive materials to allow for the

application of high potentials to the tip. High purity tip materials with well ordered crystalline structures are more capable of sustaining high fields due to the tendency for tip failure to occur at crystal grain boundaries.

The applied field F_{app} at the tip surface can be approximated [11] by

$$F_{app} = \frac{V}{kr_t} \tag{2.1}$$

where V is the potential of the tip, k is a shape factor and r_t is the radius of the tip at the apex. The shape factor (generally taken to be 5[12]) accounts for the deviation from a spherical field model due to the shank of the emitter tip.

A more accurate solution for the field near an emitter tip can be calculated by applying non-integral Legendre functions to the solution of the potential distribution near a sphere mounted on the tip of a cone[15]. This significantly more complicated method results in an equipotential surface a short distance from the sphere / cone model that is very similar in shape to an actual emitter tip. If this equipotential surface is taken to be the tip surface at potential, accurate field calculations may be made.

2.1.2 Tip Preparation

The technique employed for the preparation of an emitter tip varies widely with the emitter tip material. Many recipes and methods are available[12-14]. Preparation of a simple pure metal (e.g. Pt, W, etc.) emitter tip typically begins with a high purity thin wire blank of less than 0.5 mm diameter. The wire may be annealed to help eliminate crystal grain boundaries. The wire is then electrochemically etched under conditions found

to be favorable for the specific emitter type. For example, Pt is etched in a molten mixture of 4 parts $NaNO_3$ and 1 part NaCl with direct current of between 1 and 3 volts, while Ir requires ~10 V AC in a 30% chromic acid aqueous solution.

2.2 Field Emission

Field emission of electrons from an emitter tip was proposed by Fowler and Nordheim[16] in 1928 and first experimentally observed by Müller[17, 18] in 1935. The work function ϕ represents the free energy difference between an electron at the Fermi level and the electron removed to the vacuum level away from the surface. Figure 2-2a is an energy diagram showing the work function for a metal with no applied field. Typical work functions for metals are around 5 eV. Fowler and Nordheim suggested that at sufficient fields, electrons would be able to tunnel through the barrier allowing low temperature field emission. Figure 2-2b illustrates how the applied field reduces and narrows the emission barrier to facilitate electron tunneling.

Fowler and Nordheim provided an exact solution to the Schrödinger equation for a simple triangular barrier to estimate the tunneling probability for an electron. Their solution was the original Fowler-Nordheim (FN) equation. The original equation has been modified to include a more physically accurate barrier (suggested by Schottky) requiring use of the Jeffreys-Wentzel-Kramers-Brillouin (JWKB) approximation for the solution of the Schrödinger equation. The commonly accepted standard form of the FN

equation comes from Murphy and Good[19] in 1956. The standard assumptions [20] for FN theory include:

1. A metal with a free electron band structure
2. Electrons in thermodynamic equilibrium that obey Fermi-Dirac statistics
3. Metal at zero temperature
4. A smooth, flat surface
5. A uniform local work function that is independent of applied field
6. A uniform electric field above the emitting surface
7. Applicability of a classical image potential between the electron and surface
8. Applicability of assumptions inherent to the JWKB approximation

The standard form of the FN equation for the emission current I is

$$I = \frac{A\alpha F^2}{\phi}\exp\left(-\frac{\beta\phi^{3/2}}{F}\right) \tag{2.2}$$

where A is the area of emission, F the applied field, ϕ the work function, and α and β are constants. Rearranging Eq. 2.2 and taking the natural log provides

$$\ln\left(\frac{I}{F^2}\right) = -\beta\phi^{3/2}\left(\frac{1}{F}\right) + \ln\left(\frac{A\alpha}{\phi}\right) \tag{2.3}$$

Substituting Eq. 2.1 into Eq 2.2, assuming a constant emission area, and collecting constant terms gives

$$\ln\left(\frac{I}{V^2}\right) = C_1\phi^{3/2}\left(\frac{1}{V}\right) + \ln\left(\frac{C_2}{\phi}\right) \tag{2.4}$$

where C_1 and C_2 are constants. This is a useful form for determining a change in work function from experimental data. Experimental data for $\ln(I/V^2)$ may be plotted as a function of $1/V$ to determine the slope and intercept for this linearized form. By comparing the slope of a clean tip surface to that of an adsorbate covered surface, the ratio of the two work functions can be estimated. If the work function of the clean tip is known, the change in work function due to the adsorbate may be calculated. Additionally, if the constant terms can be determined for the surface under investigation, the work function may be directly calculated.

The actual geometry of an emitter tip obviously differs greatly from the flat plane assumption. Different crystalline planes of the same emitter tip have different work functions. For example[21], Al (111) has a work function of 4.26 eV, while Al(110) has a work function of 4.06 eV. As a result, field emission current can vary significantly in different locations of the same emitter tip. Field emission microscopy (FEM) is a technique that takes advantage of these differences and provides a visual image of the local emission current from the emitter tip.

The field emission microscope was invented by Erwin Müller in 1936[17]. Figure 2-3a depicts a simple schematic[11] of a field emission microscope. The emitter tip is mounted on a heating loop that is connected to the vacuum feed through. The emitted electrons travel to the anode which is coated with fluorescent materials to provide a viewable image. Modern field emission microscopes make use of chevron multi-channel plates (MCPs) to

amplify the electron signal before exciting a phosphor screen for imaging, but the fundamental method remains unchanged. Figure 2-3b illustrates how the tip geometry is translated into field images such as the field emission micrograph shown in Figure 2-4a. The bright areas in this figure correspond to low work function surfaces on the emitter tip. Field emission microscopes provide typical magnifications on the order of $10^5 - 10^6$. The resolution of the FEM is limited by a combination of the statistical momentum distribution of the emitted electrons and electron diffraction effects. The statistical momentum distribution is usually the dominant limitation, except at very high voltages, and results in a resolution limit of ~ 20 Å for a 1000 Å emitter tip[11]. Tip temperature does not play a significant role in field emission microscopy resolution.

An additional use for electron emission from the tip is ion sputter sharpening of the tip itself. Introducing a small amount (~10^{-4} Torr) of neon or argon into the chamber with the emitter tip results in ion bombardment of the tip apex. Some emitted electrons strike the noble gas molecules and ionize them by knocking loose an electron. The positively charged ions follow the field lines back to the negatively charged tip and bombard it. This can result in a small degree of tip sharpening. A more complete procedural guide to emitter tip ion sputtering is provided by Scovell[22].

2.3 Field Ionization

Field ion microscopy was invented in 1951 by Erwin Müller[23]. This form of microscopy provides spatial resolution of ion emission from an emitter

tip. Figure 2-5 illustrates the mechanism of a field ion microscope for the case of imaging with neon[24]. Neon is introduced into the vacuum chamber to a pressure of 10^{-4} Torr. The potential of the emitter tip is increased (positive) until a clear image is obtained. During imaging, the best imaging voltage (BIV) is recorded and used to estimate the tip radius using Eq. 2.1. At the best imaging potential in neon, the field is known to be 3.75 V/Å[24]. The best imaging voltage depends on the properties of the imaging gas (primarily the ionization potential). Throughout this document, field is reported as the applied field, which is the field that would be present at the tip surface for the applied voltage V_t in the absence of any adsorbate.

Molecules near the positively biased tip surface are polarized by the high field and attracted to the tip. When the imaging gas molecule strikes the surface it will partially thermally accommodate with the surface. By cooling the tip with liquid nitrogen or helium, this thermal accommodation results in an energy loss by the impinging molecule. As the molecule caroms away, it fights polarization attraction along with any dipolar (or higher) attraction that may be present. This may result in further collisions with the tip surface, each reducing the kinetic energy of the imaging molecule and more strongly trapping the molecule within the surface field. During each “hop” along the surface, there is a chance of an electron from the outer shell of the imaging gas molecule tunneling into the tip surface resulting in the ionization of the molecule. This tunneling probability depends (among other things) on the distance the molecule is from the tip surface. If the molecule is too far from

the tip, the tunneling probability is low due to the width of the tunneling barrier. If the molecule is too close, the electron potential would be below the Fermi level of the tip. In this case, there are no states available to receive the tunneling electron, and tunneling is forbidden. As a consequence, molecules may thermally accommodate to an energy that forbids them from hopping to a sufficient distance for tunneling to occur, and they become trapped on the surface. The ideal tunneling distance is known as the critical distance x_c, given by

$$x_c \cong \frac{(I_P - \phi)}{eF} \tag{2.5}$$

where I_P is the ionization potential of the imaging gas molecule[12], assuming the image force on the electron may be neglected. For the example of Ne with I_p of 21.6 eV on a Pt(111)surface with ϕ of 5.9 eV at the best imaging potential (3.75 V/Å), this gives a critical distance of 4.2 Å. Figure 2-6 illustrates the tunneling barrier and field lines for an imaging gas molecule near the surface. The tunneling probability D for a molecule at the critical distance is given by

$$D = \exp\left[-0.683\left(I_P - 7.59F^{1/2}\right)^{1/2} \frac{(I_P - \phi)}{F}\right] \tag{2.6}$$

where I_p and ϕ are given in eV, and F is in V/Å.

After the imaging gas is ionized, it is rapidly accelerated radially by the field. A multi-channel plate and phosphor screen assembly is positioned a few centimeters from the tip in the path of the accelerated ions. On the emitter tip surface, field strength depends on the local radius of curvature. Surface imperfections and protrusions result in a higher degree of local curvature and

therefore higher local fields. As a result, ionization of an imaging gas is more probable at these locations. For crystalline structures, this means that the image gas will preferentially ionize at step edges. For a well ordered cryo-cooled emitter tip, the preferential ionization probability results in a clear image of the tip structure as shown in Figure 2-4b for neon on platinum.

The ionization behavior of the imaging gas is influenced by both the field strength and the supply of imaging gas to tip. At very high fields, nearly all of the incoming imaging molecules are ionized in vacuum prior to reaching the tip surface. The ionized molecules have a potential energy deficit with respect to ions formed on the tip surface (due to the electric field) and are produced at the limit of the gas supply function, i.e. nearly all of the molecules approaching the tip are ionized. This supply function is greater than what is predicted by simple kinetic gas flux theory due to the polarization attraction of molecules in the presence of the high field. Furthermore, the dominant supply of gas molecules to the tip is typically from molecules hopping up the shank of the tip in the direction of the increased field[12].

At lower fields, nearer the onset of ionization, where the supply is much greater than the ionization rate, the ionization rate is given by dividing the equilibrium number of particles near the tip apex by the average ionization lifetime τ of a molecule. The average ionization lifetime can be estimated as the reciprocal of the product of the number of tunneling attempts per second ν_e (10^{15} to 10^{16} s^{-1}) and the tunneling probability given in Eq. 2.6[11].

$$\tau = \frac{1}{\nu_e D} \tag{2.7}$$

At intermediate fields, the system is more complex, as incoming molecules impinge on the surface, thermally accommodating with each hop, and then either escape, ionize, or remain trapped when unable to reach the critical distance.

An additional effect of the field enhancement at regions of high curvature is realized through field desorption of the emitter tip. At high positive fields, there is significant electrostatic pressure on the surface atoms of the emitter tip. At sufficiently high fields, the surface atoms themselves will ionize and accelerate from the tip. For Pt, field desorption occurs at a field of 4.5 V/Å. The Pt atoms are primarily desorbed as Pt^{2+}. It has been shown using both an image-hump model[25] and a charge exchange model[26] that desorption of multiply charged ions may occur at lower fields than singly charged ions depending on the properties of the metal. Since the field is enhanced near high curvature localizations, the atoms forming these localizations will desorb preferentially. As a result, the tip will become smoother as it undergoes field desorption, until the tip resembles the ordered surface shown in Figure 2-4b. After the surface is well ordered, desorption occurs primarily from step edges, i.e. the same spots that show brightly from the neon ionization. Because the desorption field for Pt is only slightly higher than the best imaging field for neon, the combination is useful for visually field cleaning the emitter tip. Field cleaning is performed by desorbing a few complete layers of the tip to ensure that surface adsorbed contaminants are desorbed along with a few monolayers of tip.

2.4 Field Ionization and Desorption Spectrometry

The field ion microscope has been extended to studies of high field surface chemistry through the advent of field ionization and desorption spectrometry techniques. In these techniques, the mass to charge ratios of ions accelerated away from the tip surface are analyzed using time of flight or ExB mass resolution.

2.4.1 ExB Mass Resolution (Wien Filter)

Wien filter mass spectrometry provides continuous mode ion mass to charge resolution. It allows for the easy separation of distinct masses without perturbing the equilibrium of the study system. The Wien filter operates by focusing the ion beam through crossed electric and magnetic fields. A beam of ions with mass m and energy eV_0, where V_0 is the accelerating potential for an ion (i.e., potential of the tip in reference to ground) and e is the ion charge, follows a straight path through the crossed electrical and magnetic fields of a Wien filter when the electrical force, eE, is equal to the magnetic force $ev B$, where E is the field strength, v is the ion velocity perpendicular to the magnetic field, and B is the magnetic field strength. The velocity v of the ion is determined by its mass and kinetic energy K.

$$v = \left(\frac{2K}{m} \right)^{1/2} \tag{2.8}$$

However, the ion gains its full potential energy neV_0 within a very short distance from the emitter tip, allowing us to substitute neV_0 for K in 2.8. Then the electromagnetic force balance requires that

$$E = B\sqrt{\frac{2neV_0}{m}}\,. \tag{2.9}$$

For ions of masses other than m in the same accelerating potential, the electrical and magnetic forces will not be balanced. As a result, each ion is shifted to the left or right in the plane of the electric field, depending on whether its mass is greater or less than m. Figure 2-7a illustrates the crossed fields and ion deflection. Only ions with masses near m will be registered on the MCPs at the end of the drift tube. Figure 2-7b shows a basic operating diagram of a Wien filter. The total force F (in the y direction only) on the ion traveling initially along the x-axis with a velocity υ_x is a combination of the electric field (y direction) and the magnetic field (z direction) given by,

$$F_y = \left(neE_y - ne\nu_x B_z\right). \tag{2.10}$$

where the subscripts represent the direction of the vector. For the system described, with the ion path, magnetic field and electric field all mutually orthogonal and aligned with the x, y and z axes, respectively, all of the subscripts except for the velocity may be dropped without loss of clarity. The force accelerates the ion according to Newton's law giving,

$$\frac{d^2y}{dt^2} = \frac{1}{m}\left(neE - ne\upsilon_x B\right). \tag{2.11}$$

Integrating Eq. 2.11 provides the y velocity,

$$\frac{dy}{dt} = \frac{1}{m}\left(neE - nev_x B\right)t \;\; + \nu_{y,0} \tag{2.12}$$

where $\upsilon_{y,0}$ is the initial velocity in the y direction. Integrating a second time provides the y position as a function of time,

$$y = \frac{1}{2m}\left(neE - nev_x B\right)t^2 + v_{y,0}t + y_0\,, \tag{2.12}$$

where y_0 is the initial position. Solving for the position and velocity at the exit of the Wien filter (position II) where

$$t = L_w / v_x \tag{2.13}$$

with the length of the Wien filter taken as L_w, and with y_0 and $v_{y,0}$ both equal to zero, gives

$$y\big|_{x=L_w} = \frac{1}{2m}\left(neE - ne v_x B\right)\left(\frac{L_w}{v_x}\right)^2 \tag{2.14}$$

$$\left.\frac{dy}{dt}\right|_{x=L_w} = \frac{1}{m}\left(neE - ne v_x B\right)\left(\frac{L_w}{v_x}\right) \tag{2.15}$$

Now to solve for the y position of the ion at the end of the drift tube, we employ Eq 2.12 again using Eqs. 2.14 and 2.15 as y_0 and $v_{y,0}$, respectively, and

$$t = L_w / v_x \tag{2.16}$$

but now taking E and B to be zero, leads to

$$y\big|_{x=L_w+L_D} = \frac{1}{m v_x^{\,2}}\left(neE - ne v_x B\right)\left(L_W L_D + \frac{L_W^{\,2}}{2}\right). \tag{2.17}$$

Finally, for ions with kinetic energy equal to the initial tip potential V_0, can substitute Eq. 8 into Eq 2.17, resulting in

$$y\big|_{x=L_w+L_D} = \frac{1}{2V_0}\left(E - \sqrt{\frac{2neV_0}{m}}B\right)\left(L_W L_D + \frac{L_W^{\,2}}{2}\right). \tag{2.18}$$

With Eq. 2.18, fields may be calculated for selecting ions and excluding near mass ions.

Figure 2.8 shows an example of ion separation using a Wien Filter for protonated water clusters of masses 19 and 37. The triangular shape of the ion beams in this figure is an artifact of the construction of the focusing lens.

2.4.2 Pulsed Time of Flight Mass Spectrometry

Pulsed time of flight (ToF) mass spectrometry provides accurate mass to charge resolution by measuring the flight times of ions formed due to a system perturbation such as a potential pulse or a laser pulse. With an applied potential on the tip, ions emitted from the tip by the pulse are accelerated away from the tip and travel down the flight tube for detection by the MCPs. The flight time of the ion depends on its velocity, which is determined by the ion mass and kinetic energy as described in Eq. 2.8. Shortly after the ion leaves the tip, its kinetic energy is equal to its initial potential energy neV_0 (excluding energy deficit subtleties) giving,

$$v = \left(\frac{2neV_0}{m} \right)^{1/2} \tag{2.19}$$

Deficits in the initial potential energy may occur if energy is spent during emission (e.g. the breaking of chemical bonds), or if ionization occurs further from tip surface. Substituting flight distance L_D divided by the time of flight t for the velocity of the ion and solving for m/n results in,

$$\frac{m}{n} = \frac{2eV_0}{L_D^{\,2}} t^2 . \tag{2.20}$$

To account for delays in pulse timing, t may be replaced with $t+\delta$, where δ is a small delay term.

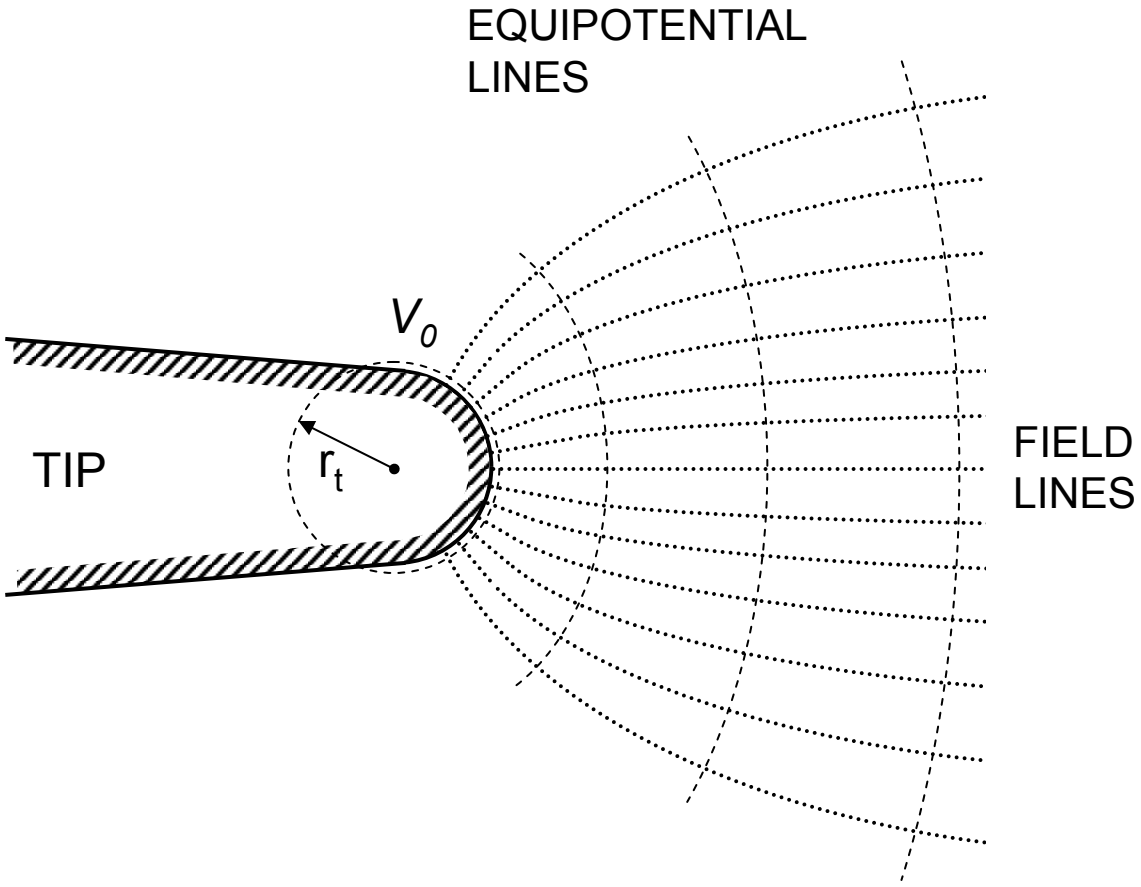

FIGURE 2-1: Emitter tip schematic. The hemispherical tip radius is typically 100 – 1000 Å.

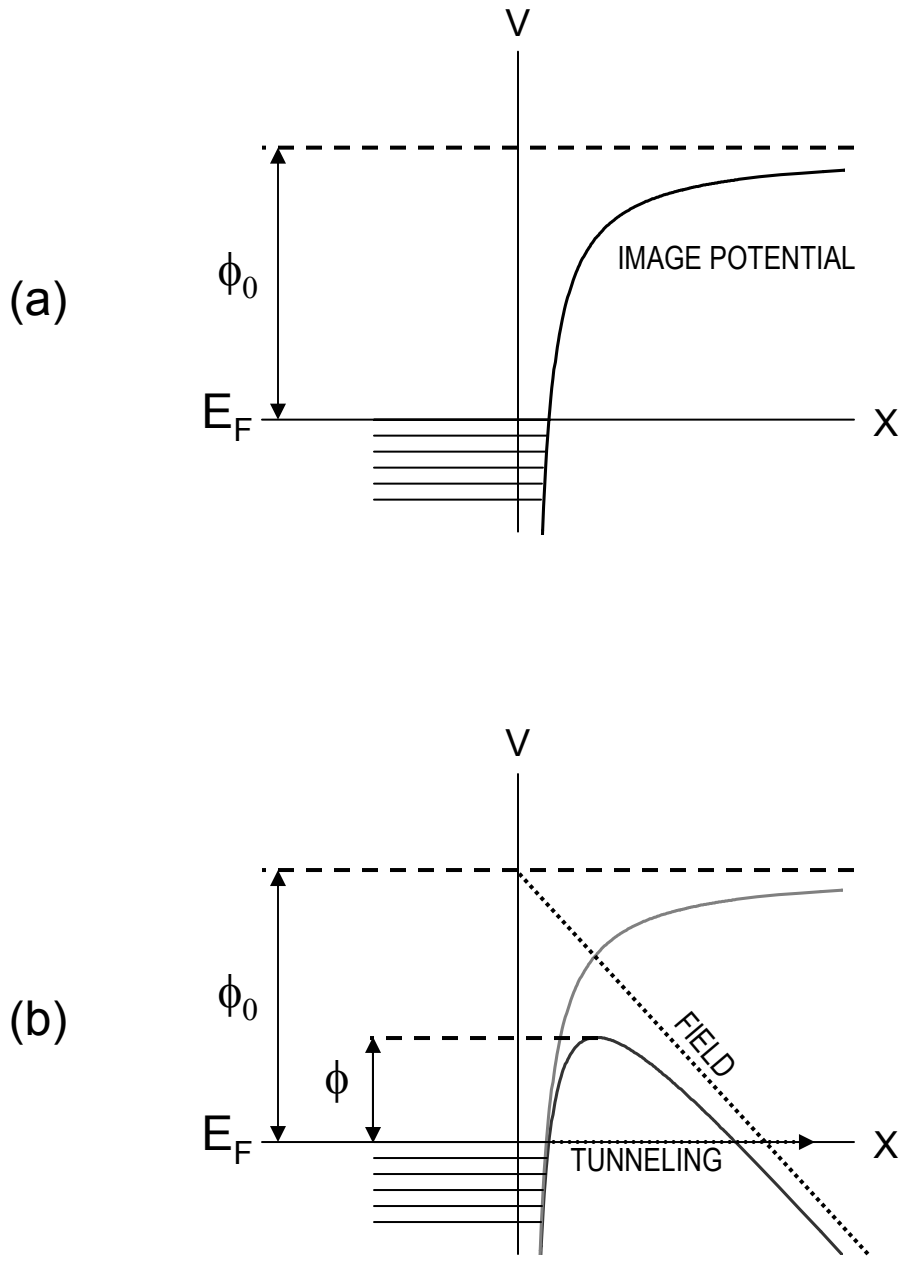

FIGURE 2-2: Field effect on electron emission barrier. (a) Emission barrier with image force and no external field. The work function ϕ_0 is the energy required to remove an electron from the Fermi level E_F. (b) Barrier in the presence of a high field. The effective work function ϕ is lower, and the barrier has narrowed allowing tunneling of electrons.

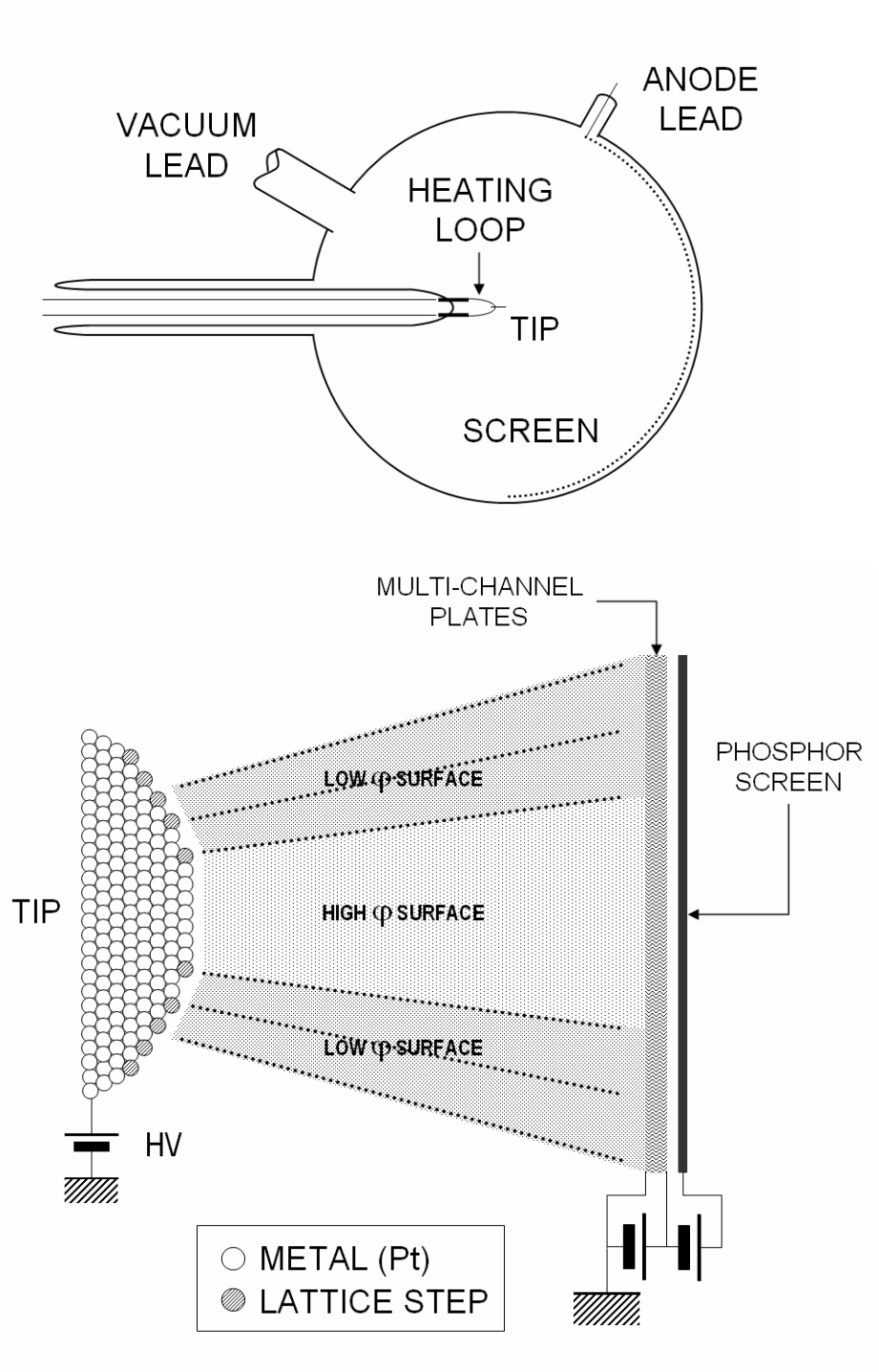

FIGURE 2-3: Field emission microscope. (a) Simplified schematic of an early field emission microscope. (b) Method of operation.

(a)

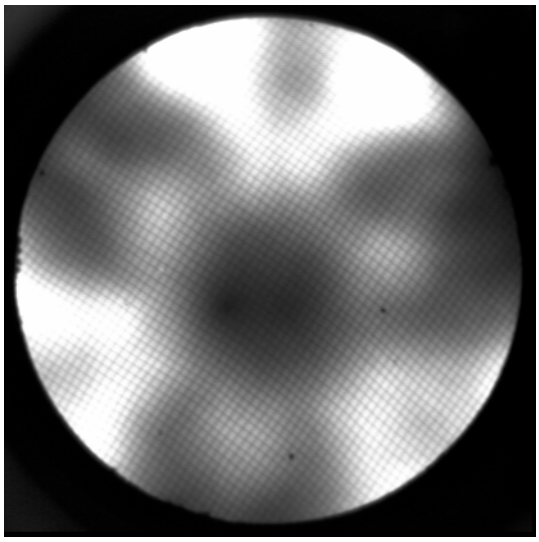

(b)

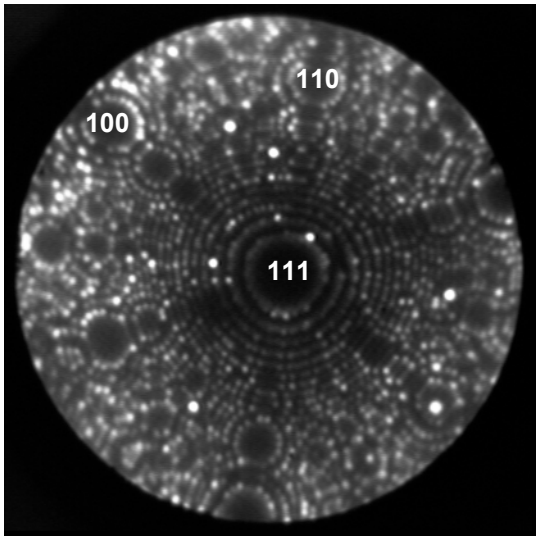

FIGURE 2-4: Experimental images of a Pt(111) oriented field emitter tip with a tip radius r_t ~ 550 Å. (a) Field emission micrograph at an applied negative field of 0.43 V/Å. (b) Field ion micrograph with 10^{-4} Torr Ne, T = 110 K, and positive applied field of 3.75 V/Å.

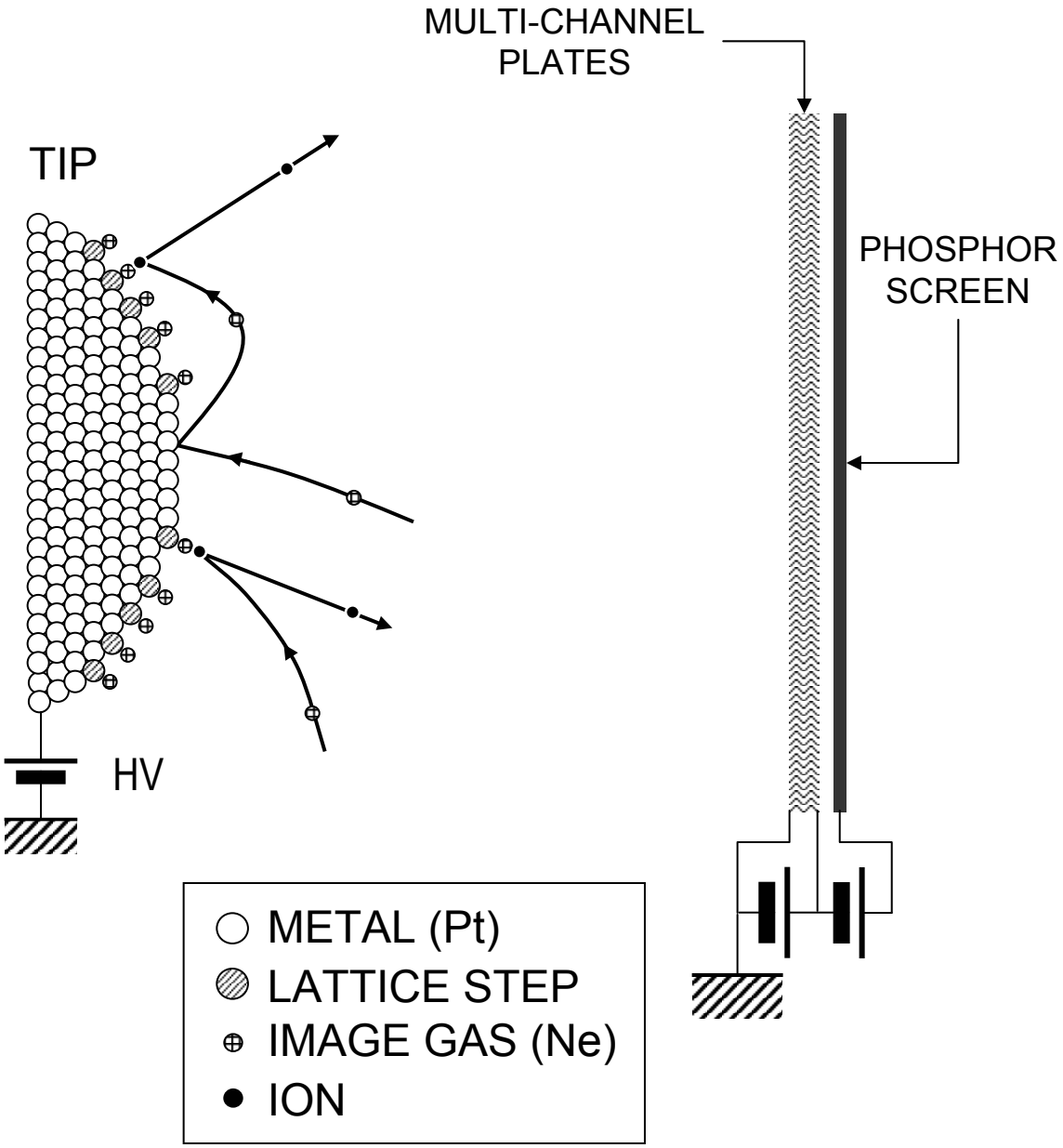

FIGURE 2-5: Field ion microscope method of operation.

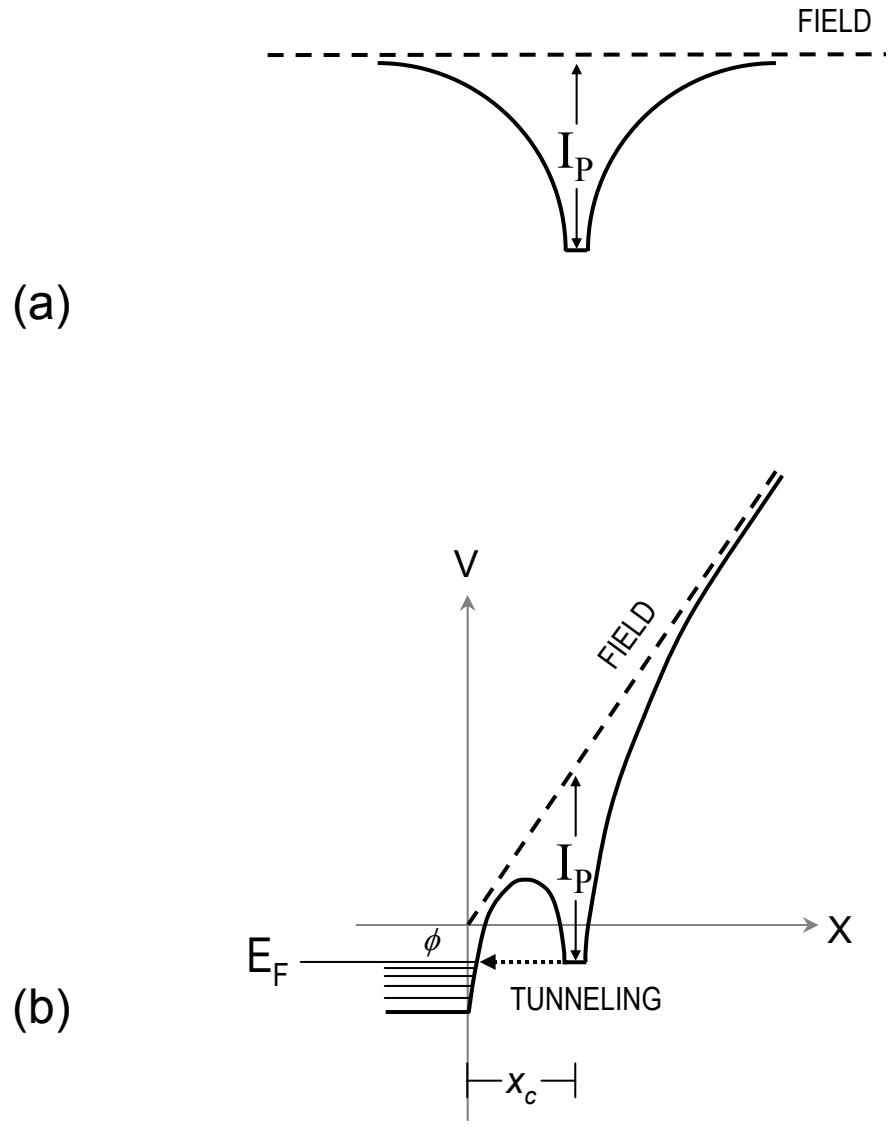

FIGURE 2-6: Field ionization mechanism. (a) Ion in free field with ionization potential I_P. (b) Ion near surface in high electric field at critical distance x_c where electron can tunnel to the Fermi level E_F.

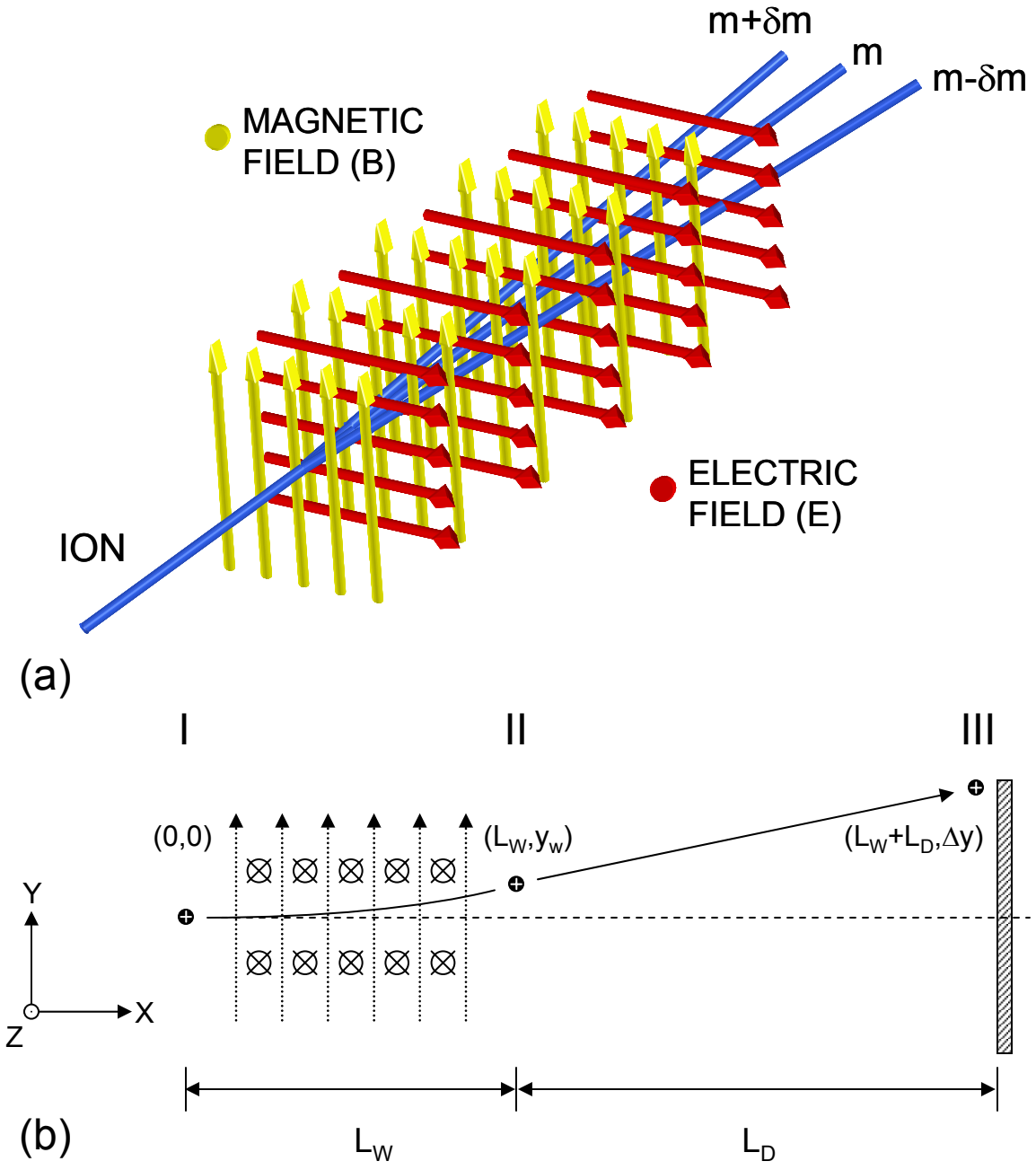

FIGURE 2-7: Wien filter operating principles. (a) Crossed field orientation for ion path results in straight passage for mass m, but deflection for mass m+/-dm. (b) Deflection path for ion I. Entering the Wien filter of length L_W, II. Leaving the Wien filter, and III. Arriving at the end of the drift tube of length L_D. Magnetic field lines are directed into the page.

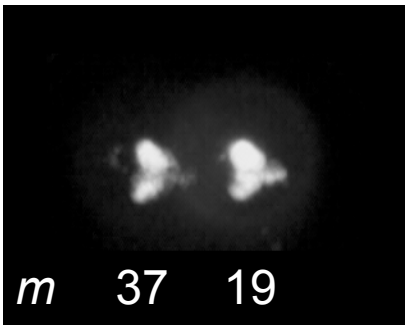

FIGURE 2-8: Wien filter separation of mass 19 and mass 37 protonated water clusters.

CHAPTER 3: LITERATURE REVIEW

3.1 Water

Volumes of literature have been written about the characteristics of water and ice. Of particular relevance to this research are works concerned with the behavior of water and ice on surfaces and in high fields, the ionization of water molecules, and phase transitions and characteristics. Solvation energies and transport properties of hydronium and hydroxyl molecules are also important to understanding the behavior of water on the tip surface. An excellent starting point for research concerned with water on surfaces is the 1987 comprehensive review article [28] by Thiel and Madey. This work provides detailed discussions of the properties of molecular water, surface bonding of water for metallic and oxide surfaces, dissociation products and their behavior, and adsorption/desorption kinetics among other topics. The water literature has been revisited in an extensive 2002 review article by Henderson[29] that brings together all of the recent advances made in water related surface science.

3.1.1 Properties and Phase Behavior

Water is a seemingly simple substance, but is rich with interesting behavior due largely to its small molecular size, strong molecular dipole (1.854 D)[30], extensive hydrogen bonding and high dielectric constant (~80 for liquid water at 0 °C). It is capable of molecular solvation and charge screening. The

dissociation of water to form H^+ and OH^- ions occurs readily. These factors contribute to the many anomalies of water and have lead to a significant body of research focused on water.

A single isolated water molecule has an H-O-H bond angle of 104.474°and an O-H bond length of 0.95718 Å[29]. In liquid water, both bond length and angle increase slightly[30] to 0.970 Å and 106°, respectively, because of hydrogen bonding. Under standard conditions, water boils at 373.15 K with a latent heat of vaporization of 40.657 kJ/mol[28] and freezes at 273.15 K to form hexagonal crystalline ice (Ih) with a heat of fusion of 6.01 kJ/mol.

The solid phase behavior of water has been the subject of much research. There are two forms of crystalline ice I, hexagonal (Ih) and cubic (Ic), plus eleven more crystalline ice "phases" numbered II through XII in addition to a variety of amorphous ice types that do not have crystalline structures. The phases differ by crystalline structure and molecular symmetry. Hobbs[31] describes the behavior and physics of the first several ice structures in detail. More recent exotic ice types have been formed[32-34] at extreme pressures and temperatures. The creation of ice IX[35], which can be formed from ice Ih at 250 K and 300 MPa, fortunately did not destroy the world as suggested by Vonnegut[36].

For the range of conditions available to the experimental system in this study ($T > 105$ K; $P < 10^{-4}$ Torr), a limited subset of these ice types are available for study. These include ice Ih, ice Ic and amorphous solid water

(ASW). Ice deposited on cold surfaces at low temperatures (~140 K) under vacuum conditions forms amorphous solid water[37]. The properties of ASW have been studied extensively by the Kay group in recent years. Their research has outlined ASW phase behavior[37-39], energetics[40], structure and morphology[41, 42], and transport poperties[43]. TPD experiments characterized the very slow crystallization of ASW to cubic crystalline ice above ~135 K. During this phase transition, water behaves as a supercooled liquid. At temperatures above 140 K, the transition occurs on a "laboratory time scale." The morphology of ASW was found[41, 42, 44] to depend on the angle of incidence of the adsorbing water molecules as well as the deposition temperature. Temperature programmed desorption (TPD) ramping of adsorbed nitrogen was used to determine the surface area of the ASW. Jenniskens et al.[45, 46] also investigated ASW and the presence of liquid water under conditions favoring cubic crystalline ice phase using TEM, reflection absorption infrared spectroscopy (RAIRS) and TPD. Ice Ic will slowly convert to ice Ih between 170 K and 220 K with a heat evolution of 40 J/mol[47]. Above ~140 K under vacuum conditions, it is suggested[31] that water is deposited on a cooled surface as ice Ih, although the exact transition remains unsettled. Cubic and hexagonal ice differ only in the stacking pattern of the ice bilayers. For ice Ih, the stacking pattern is ABAB, while the stacking pattern of ice Ic is ABCABC (diamond like)[48].

3.1.2 Dissociation and Ionization of Water Molecules

Water molecules may be ionized primarily in two ways. The first is the direct ionization of the water molecule by removing an electron (e.g. by photoionization).

$$H_2O + h\nu \rightarrow H_2O^+ + e^- \qquad (3.1)$$

This method requires a photon with energy $h\nu$ that exceeds the ionization potential (12.6 eV[28]) The second is the dissociative ionization of a water molecule according to

$$jH_2O \leftrightarrow H^+(H_2O)_n + OH^-(H_2O)_{j-n} \qquad (3.2)$$

The dissociation energy barrier for the reaction shown in Eq. 3.2 depends strongly on the j and n which determine the extent of solvation for the reaction products. Direct dissociation (j = 1 ;n = 0) requires 5.46 eV, while fully solvated ($j,n \rightarrow \infty$) dissociation has been experimentally reported to require as little as 0.59 eV[49] for liquid water.

Dissociative ionization of a water molecule depends strongly on the state of the surrounding system. *Ab initio* calculations[50] using transition path sampling suggest rare fluctuations in solvent structure lead to a destabilization of the OH bond and the subsequent dissociation of a water molecule at room temperature in ~ 10 hours. The newly created ion pair is initially separated by ~ 6 Å. Numerous other simulations and calculations have been carried out to determine dissociation energies[51] and pathways[49, 52].

Other models have attempted to determine pathways for dissociative adsorption of water on surfaces. For example, Cho et al[53] used DFT calculations to show that intermolecular hydrogen bonding plays an important role in water dissociation on MgO(100). They showed that single water molecules adsorb molecularly, but subsequent molecules adsorbing onto partially covered surfaces are dissociatively adsorbed. Lindan et al[54]performed first principles molecular dynamics simulations of water dissociation on TiO_2 and showed that dissociation is energetically favorable on the five-fold Ti site. These TiO_2 results were confirmed experimentally by Brookes, et al. [55] using STM to directly determine the water adsorption sites on TiO_2(111)-(1x1) at 150 K and then watch the dissociation products at 290 K. Water adsorbed on the five-fold Ti atoms was observed to dissociate on the bridging O vacancies.

An extensive resource for bond dissociation energies, molecular acidities, ionization potentials and electron affinities for a variety of R-H bonds, including methanol and ethanol and H_2O data, has been prepared by Berkowitz et al.[56] using three different experimental methods. This is useful for thermodynamic considerations of dissociated species.

3.1.3 Protonated Water Clusters

Nearby water molecules not only play a role in facilitating the actual dissociation event, but continue to screen the separated charges after the event. The solvation energy due to the first few solvation shells is quite significant. Experiments to determine proton solvation enthalpies and free

energies[57-59] have shown that, for a protonated water cluster $H^+(H_2O)_n$, the solvation energy due to the nth solvating water molecule decreases with increasing n. Molecular simulations have been employed to characterize ion clusters and solvation shells – particularly the behavior of the proton itself. *Ab initio* molecular dynamics calculations[60] of the simulated annealing of protonated clusters (n = 7-8) showed n = 4 ("magic number" shell) stability and a competition between a core structure of H_3O^+ and $H_5O_2^+$. The two states had very similar energy levels. Sagnella, et al.[61] used an empirical valence bond model to investigate proton transfer in water. Using *ab initio* potential energy calculations, they showed that the proton diffuses through water by

$$H_9O_4^+ \leftrightarrow H_5O_2^+ + 2H_2O\,. \qquad (3.3)$$

The proton diffuses through the water by shifting from the $H_9O_4^+$ structure (hydronium core) to the $H_5O_2^+$ structure, often called the Eigen and Zundel cations, respectively.

These results corroborated earlier results by Tuckerman[62], who observed the protonated solvation cluster complex shifting between n = 2 and n = 4 in *ab initio* molecular dynamics calculations. Several other theoretical simulations have been performed in recent years to determine proton solvation energies[63-66].

For water ice, the proton transfer is more complicated. Tsekouras[67] et al. soft landed ions onto ASW deposited on a Pt(111) crystal. A Kelvin probe was used to measure the surface potential as a function of temperature. The voltage dropped sharply at 50 K due to the dielectric response of the ASW.

This was significantly lower than the expected value of 135 K, where the glass transition occurs, suggesting that local relaxation of the amorphous ice occurs before molecular mobility. Actual ion migration through the deposited ice was not observed until 190 K. Kobayashi et al.[68] suggested a model for fast proton transfer in cubic ice based on *ab initio* calculations. They determined that the mechanism for fast proton transport in ice is very different from the mechanism in liquid water. For liquid water, the transition is between stable protonated dimers (Zundel structure), where in cubic ice the dimer structure is destabilized. The solvation energies from distant shells were found to contribute significantly to the potential energy surface of the proton resulting in limitations of the accessible proton transfer pathways. They also suggest that the proton may prefer to stay on the surface due to strong repulsive forces from the fourth coordinating water molecule.

3.2 Water / Methanol Systems

Water methanol systems are widely studied with regard to direct methanol fuel cell research. At the anode (Pt) of a direct methanol fuel cell (DMFC) methanol and water combine to form carbon dioxide, protons and electrical current according to

$$CH_3OH + H_2O \rightarrow CO_2 + 6H^+ + 6e^- \quad . \qquad (3.4)$$

Equation 3.4 is an ideal reaction and neglects the intermediate steps that are the focus of a great deal of DMFC research. Partial oxidation products and cations formed near the electrode influence the local fields and catalyst behavior.

Meot-Ner performed an extensive study[57] of water / methanol clusters for both the cations and anions using thermochemical techniques. He determined experimental enthalpies, free energies and entropies of solvation for wide range of clusters. Others have since used vibrational spectrocopy[69], microwave dielectric analysis[70], femtosecond pump-probe spectroscopy[71] and vacuum ultraviolet time of flight spectroscopy[72] among other techniques to examine spectra of mixed water / methanol ion clusters. Neat and mixed water methanol clusters were observed, primarily of the form $H^+(CH_3OH)_m(H_2O)_n$ with m and n observed up to 10 for neat clusters. Finer mass structure was observed in these experiments but not thoroughly discussed or explained.

Time of flight experiments[73, 74] have shown that mixed water / methanol clusters undergo evaporative mestable decay in the flight tube to produce uncharged daughter products. The decay is driven by ion dipole interactions within the water / methanol ion clusters.

3.3 Field Emitter Studies

Field desorption and ionization of adsorbed molecules has been studied for many different system types. Of particular interest to this research is the behavior of water on field emitter tips. The study of water on a field emitter tip dates back to 1955 when Gomer and Inghram[75] observed the formation of ion clusters on a tungsten tip. Beckey et al.[14] further characterized water ionization by identifying the emitted ions as protonated water clusters of varying size. Schmidt[76] later provided critical ionization potentials for water

on tungsten, iridium and platinum. Anway[77] extended field ionization experiments to field adsorbed water layers at room temperature and proposed a model of the condensed water layer on the tip surface. He noted the pressure and temperature dependence of the water clusters and recognized a field dependence of ion cluster type. Jaenicke[78] used tunable synchrotron radiation to study the influence of high electric fields on polar water molecules, as well as methanol and ammonia, on a Ni tip at low temperatures (80 K-120 K). He found that the application of a high electric field resulted in whisker like ordering at temperatures below 120 K.

More recently, Stintz and Panitz have studied both protonated water clusters[79, 80] and negative ion water clusters[81] using a technique called ramped field desorption (RFD) and characterized the sizes of the ion clusters produced as the emitter tip field was ramped. Clusters were desorbed from amorphous ice layers over temperatures ranging from 33 to 140 K. They also recognized a temperature dependence of the ionization onset field, requiring higher fields at lower temperatures, and the presence of larger mass clusters at higher desorption temperatures. The negative ion work showed similar cluster formation results, and suggested the importance of ion conductivity to the emission process.

Ernst et al.[82, 83] examined hydrogen-water oscillation reactions on a Pt emitter tip. They considered possible pathways for the dissociation and ionization of water at room temperature and found through appearance energy analysis two apparent reactions resulting in H_3O^+ ions. Gorodetskii and

ionization of water at room temperature and found through appearance energy analysis two apparent reactions resulting in H_3O^+ ions. Gorodetskii and Ernst[85] later looked at the titration of adsorbed molecular oxygen created after the field dissociation water on the Pt surface using hydrogen. Sieben[95] continued this line of research and examined the energetics and kinetics of these surface reactions.

Recent work by our group[23, 96-98] has probed the onset of ionization of water clusters from a Pt emitter tip as a function of adsorbed layer thickness and tip temperature in an effort to investigate the mechanism of ionization and the response of the nearby, non-reactive water molecules. For low temperature ice layers, the ionization onset field was found to decrease from 0.6 to 0.3 V/Å as the temperature increased from 80 to 145 K. An activation barrier of approximately 0.7 eV was reported for the field free dissociation of the water molecules. A phase transition for water near 130 K was reported based on a slope break in the ionization onset field and differences in the behavior of ionization zones above and below 130 K. Additionally, a model was presented describing the dielectric response of water in high electric fields. The model provides evidence of field enhancements at the tip/water and water/vacuum interfaces. The relative field strengths at the two locations depend on the thickness of the water layer with thick water layers leading to higher fields at the tip/water interface and thin water layers resulting in higher fields at the water/vacuum interface.

Beckey[15] discusses early results using field desorption spectroscopy and discusses field dissociation of molecular ions. Additionally, theory regarding field condensation and dissociation is provided. More recently, Klesper and Röllgen have investigated the behavior of cyclohexane as an imaging gas on Pt[99] and Au[100] emitter tips. They chose cyclohexane because of the stable ring structure and lack of side chains. Consequently, dissociative ionization and fragmentation were not observed. However, water contamination in the cyclohexane sample resulted in surface oxidation and difficulties with the Pt tip. For both systems, ion emission localizations were observed.

CHAPTER 4: EXPERIMENTAL APPARTUS

The primary experimental system[88] consisted of an ultra-high vacuum (UHV) chamber pumped by a turbomolecular and titanium sublimation pumps to a base pressure of 10^{-10} Torr. Figure 4-1 shows the overall configuration of the system. The chamber was fitted with analytical equipment for performing field ion microscopy (FIM), field emission microscopy (FEM), ExB and pulsed time of flight ion mass spectrometry, and a quadrupole mass spectrometer for residual gas analysis.

4.1 Ultra High Vacuum Chamber

The UHV chamber, outlined in Figure 4-2, was equipped with analytical equipment for performing field ion microscopy (FIM), field emission microscopy (FEM), ExB (Wien filter) and pulsed time of flight ion mass spectrometry, and residual gas analysis. A downtube with emitter tip assembly (Fig. 4-2e) was mounted onto a polar coordinate manipulator for orientation towards either a micro-channel plate/phosphor screen assembly for ion/electron imaging, or a lens assembly for mass resolved analysis of emitted ions. The lens assembly focused the ion beam towards a Wien Filter assembly (Fig. 4-2c) and drift tube (Fig. 4-2b). The tip translation apparatus allowed rotation of the tip assembly about the z-axis, translation along the z-axis, and a small degree of angular tilt from the axis. The tip assembly was mounted on a cold-finger downtube

for cooling the apparatus with liquid nitrogen. The chamber was pumped by turbomolecular and titanium sublimation pump to a base pressure of 10^{-10} Torr. A gate valve located between the turbomolecular and the main chamber provides some control of the pumping speed to reduce the throughput of gases used in experiments. The turbomolecular pump and mechanical backing pump were lubricated with Fomblin to minimize possible back contamination.

4.2 Tip Assembly

Platinum emitter tips were prepared by electrochemically etching a 0.13 mm Pt wire in a 500 K mixture of sodium chloride and sodium nitrate[24]. The Pt tip of approximately 350 Å radius and [100] orientation was spot-welded to a 0.25 mm Pt wire heating loop (Figure 4-3) and mounted onto a liquid nitrogen cooled downtube (Figure 4-4a). The cryo-cooled tip, at a base temperature of 105 K, was resistively heated to the desired experimental temperature. Tip temperature was measured with a chromel-alumel thermocouple spot-welded to the heating loop near the tip. The tip potential was controlled with a ± 5 kV power supply. A planar counter electrode with a 5 mm circular hole was positioned coaxial with the tip apex at a distance of 1 mm. The counter electrode potential was independently regulated to ± 5 kV. The tip/counter electrode configuration provided fields greater than 4 V/Å, sufficient to field-evaporate Pt and thus clean the tip.

4.3 Einzel Lens Assembly

The ion focusing lens (Figure 4-4) was similar to the symmetric three-electrode unipotential type suggested by Rempfer[91]. To eliminate aberrant

electrical fields, stainless steel cylindrical rings were welded to the entrance and exit electrodes of the lens in its inner part. The addition of these rings to the usual design of the unipolar lens improved focusing of the ion beam. The lens was mounted on four supporting stainless steel rods that passed through the Wien filter, allowing the distance between the tip and the entrance diaphragm connected to the lens L_D to be varied between 20 and 56 mm. With a 5 mm diameter hole in the entrance diaphragm, ions emitted from the tip within the solid angle of 0.109 (at 20 mm) to 0.014 steradians (at 56 mm) were collected by the Wien filter assembly. For a typical tip, ions are emitted from the tip surface through angles up to ~60° from the tip axis, based on comparisons of field ion micrographs to stereographic maps of the crystalline structure. Field compression of the ion beam effectively reduces this angle to ~40°. The space angle of the total emission cone from the tip is $2\pi\,[1-\cos(\theta)] \cong$ 1.5 steradians, i.e. our Wien filter can analyze from 1% to 7% of the ions emitted from the tip depending on the position of the entrance diaphragm. For experiments with tips of radius 350 Å, ion signals of 10^3 counts/s were easily achieved at the exit of the Wien filter, which would then imply total ion emission of $10^4 - 10^5$ s^{-1}.

4.4 Gas Handling System

The gas handling system for the chamber was independently pumped using a mechanical pump. Gases were introduced through either a needle valve with a sensitivity down to 10^{-7} Torr or a variable leak valve with a sensitivity better than 10^{-8} Torr.

The water samples used for dosing was prepared by triply freezing nanopure, de-ionized water to 77 K and evacuating the containment vessel. A final freeze and evacuation of the vessel was performed at 195 K. Methanol samples were purified using the same technique.

4.5 Wien Filter Ion Characterization

The Wien filter assembly, shown in Figure 4-5, consisted of an entrance diaphragm and focusing lens (b), Wien filter (c), bellows (d) for changing the distance between the tip assembly and the focusing lens, drift tube (e), and a pair of chevron multi-channel plates (MCPs) with a phosphor screen (f) for detecting and imaging the exiting ion beam.

The Wien filter itself was constructed with curved magnetic and electric poles[92] providing homogeneity of electric and magnetic fields in the functional space of the filter. The length of the magnetic poles along the cylindrical axis was 100 mm. The electrodes were longer than the magnetic poles by 1.3 mm on each side to decrease aberrations in the boundary regions at the entrance and exit of the Wien filter.

For our system, the drift tube between the bellows and the multi-channel plate was 616 mm in length, giving a total L_D of about 800 mm depending on the bellows length. With a distance between the two Wien filter electrodes of 12.9 mm for our system,

$$\Delta x / \text{mm} = 3.3 \cdot 10^3 \frac{\Delta V}{\phi_0}\left(1 - \sqrt{\frac{m}{m+\delta m}}\right), \qquad (3.4)$$

where ΔV is the potential difference between the electrode pair (c_3). We used this equation to calculate the minimum electrode potential needed to completely separate two neighboring masses so that only one ion signal was registered on the MCPs. For our MCPs (19 mm diameter) with ϕ_0 at 3000 V, ions of mass 18 (H_2O^+) and mass 19 (H_3O^+) were separated at an electrode potential differemce of 550 V, while all other ion beams examined herein (other protonated water clusters with m up to 127) were separated with 150 V.

Direct imaging of the mass selected ion beam using a CCD camera positioned behind the phosphor screen and MCP assembly was of considerable value for tuning the ion signal. The imaging ensured good ion focus and allowed us to confirm that no signal from neighboring masses was registered on the MCPs.

4.6 Time Of Flight

For our experimental system, a uniform potential (typically 3000 V) was applied to the emitter tip. The counter electrode was set to provide a field near the threshold for ion emission from the tip. The counter electrode was then pulsed with 70 ns square potential pulses up to 1000 V. Typically, the potential of the pulse was kept low to minimize uncertainties inherent to pulsed experiments.

The pulsed ToF experiments were run using the same configuration as the Wien filter experiments, but without the electric and magnetic fields. The einzel lens was again used to focus the ion beam down the drift tube and onto the MCPs. A digital delay generator was used to simultaneously trigger the

pulser and open the window for the binning hardware. A PC interacted with the binning hardware to configure the time width of each bin and collect bin data as the ions were collected.

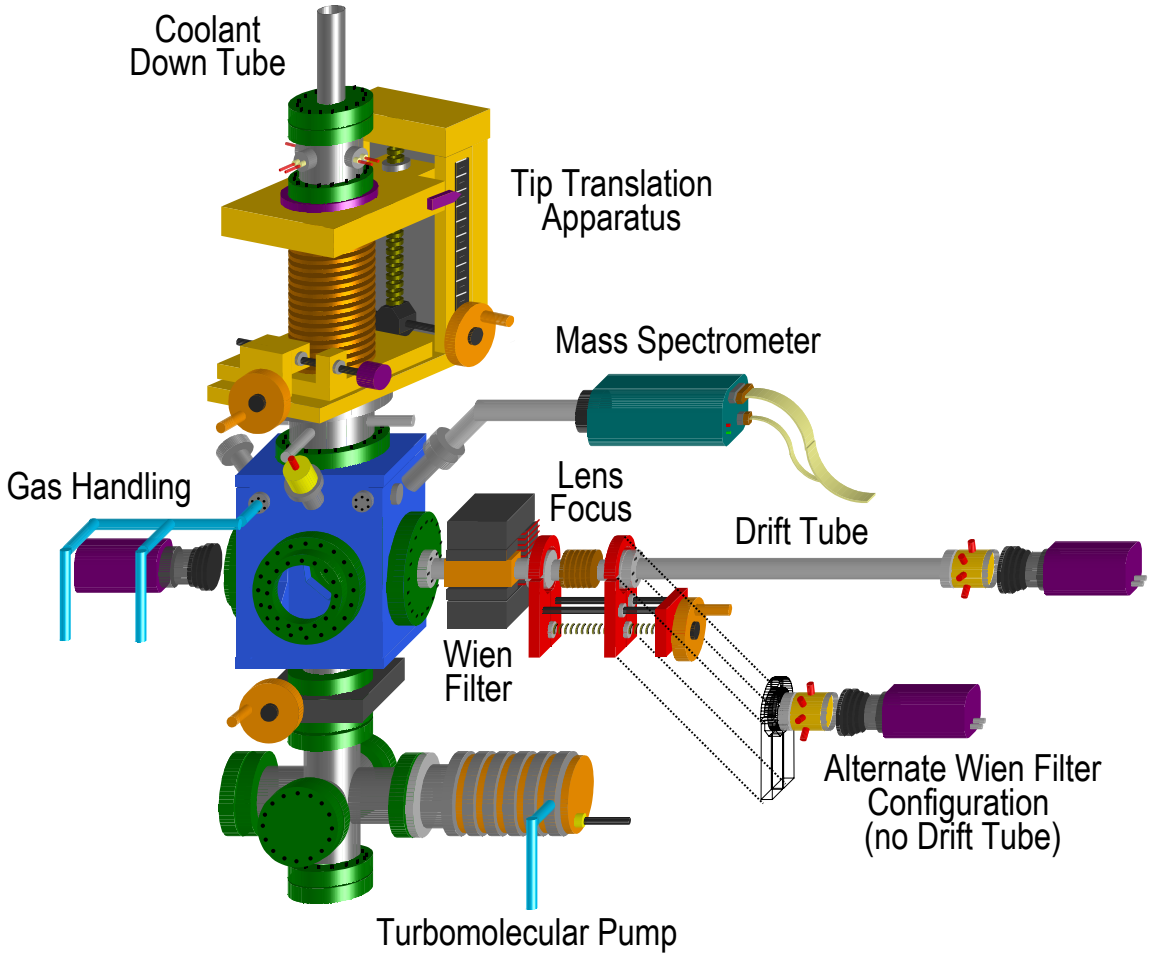

FIGURE 4-1: Experimental UHV chamber setup.

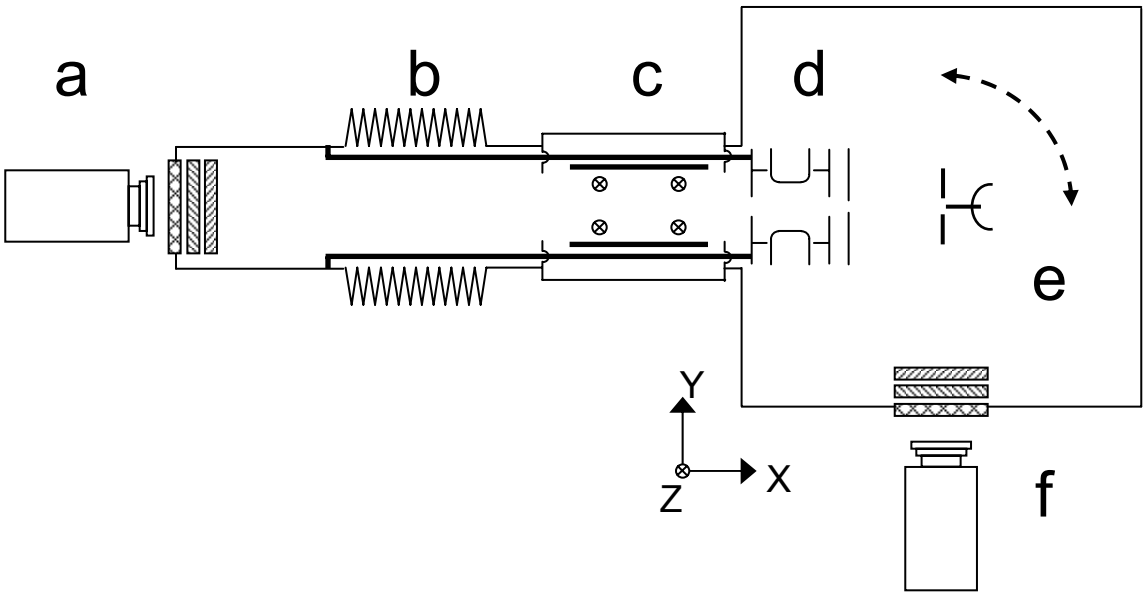

FIGURE 4-2: Schematic of experimental system. (a) Multi-channel plate / phosphor screen assembly with CCD camera for signal measurement and visual focusing of ion signal. (b) Ion flight tube with adjustable bellows. (c) Wien filter (ExB) assembly for mass selection. (d) Einzel lens assembly for ion focusing. (e) Rotatable emitter tip assembly. (f) Multi-channel plate / phosphor screen assembly for direct imaging (FIM or FEM).

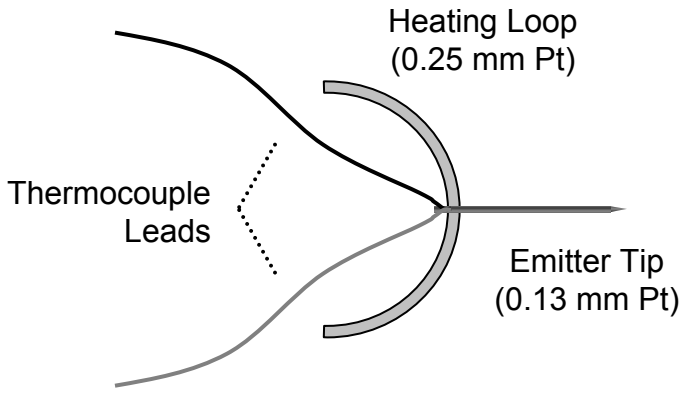

FIGURE 4-3: Pt emitter tip assembly. (Not drawn to scale)

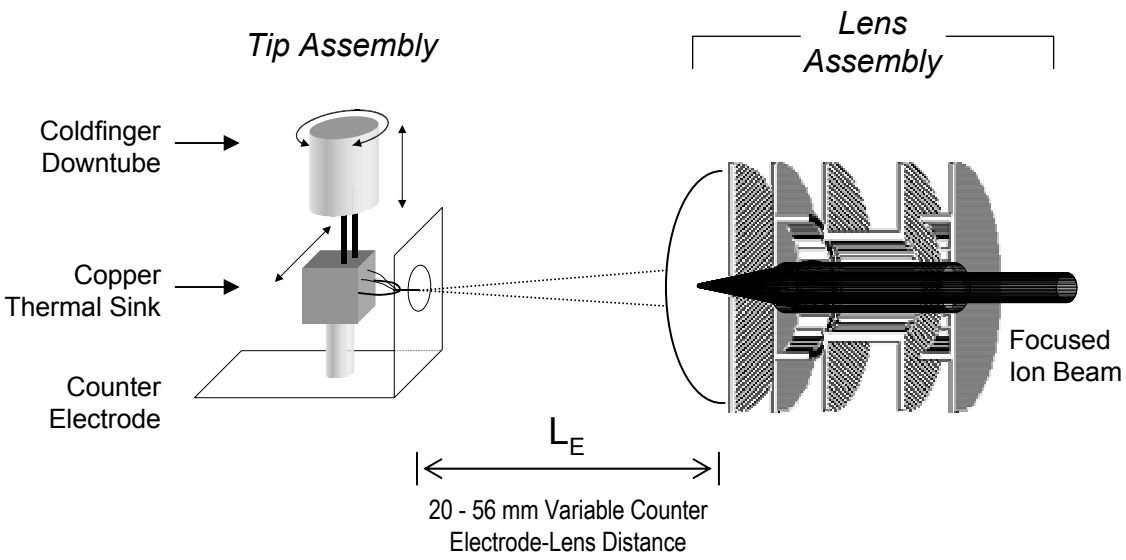

(a)

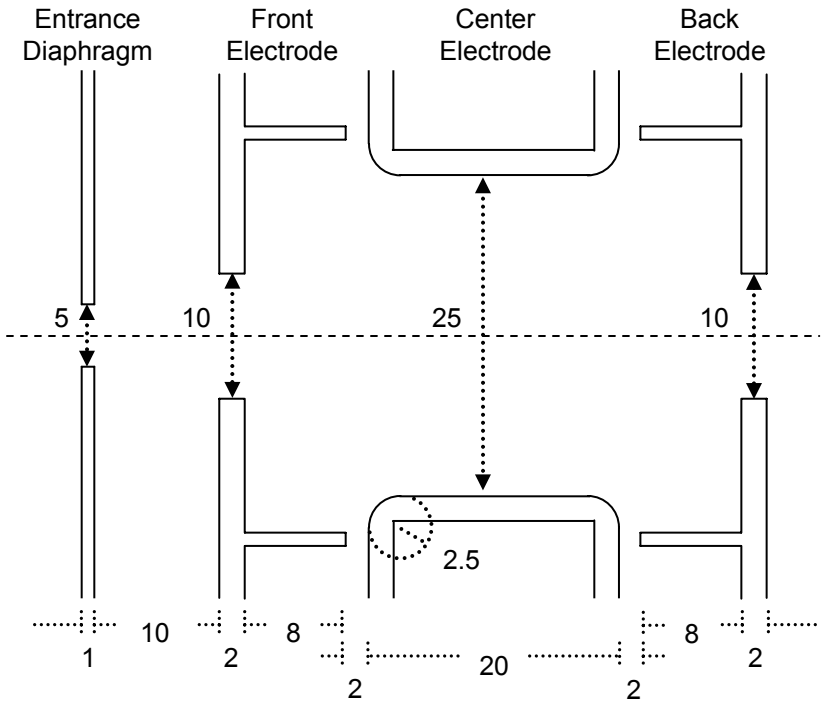

(b)

FIGURE 4-4: Einzel lens schematic. (a) Variable distance between tip / counter electrode assembly and lens. (b) Dimensions of lens design in millimeters.

I

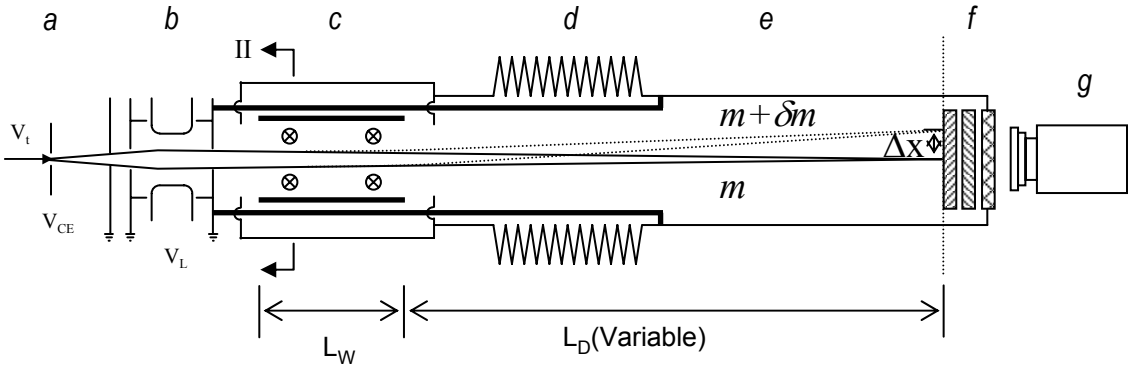

II

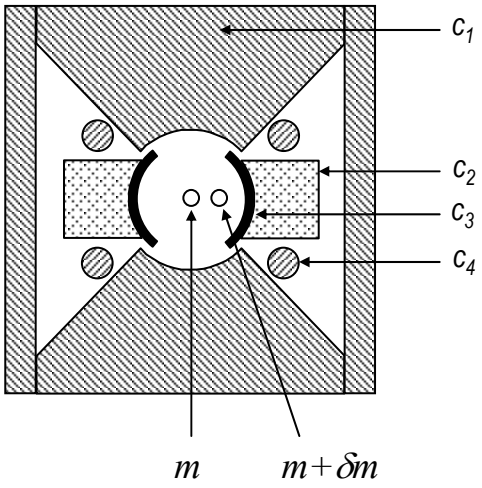

FIGURE 4-5: Wien filter and lens apparatus. I. System schematic showing flight path of ions for masses *m* and $m+\delta m$: (a) tip at potential V_t and counter electrode at potential V_{CE}, (b) lens assembly at potential V_L, (c) ExB Wien filter, (d) bellows, (e) drift tube, (f) ion detector comprised of dual chevron multi-channel plates and a phosphor screen, (g) CCD camera for imaging and focusing ion signal. II. Cross sectional diagram of ExB Wien filter: (c_1) magnet, (c_2) electrode support, (c_3) electrode, (c_4) lens support rods.

CHAPTER 5: ION CLUSTER EMISSION FROM FIELD ADSORBED WATER LAYERS ON PLATINUM

Water on an emitter tip can exist primarily in two different manners. At low temperatures, below the condensation point, multilayer ice deposition occurs. The thickness of the ice layer depends on the length of exposure and the partial pressure of water in the chamber. The properties of the ice layer also depend on the water flux and temperature as described in Chapter 2. The other regime of study is a field adsorbed water layer, which remains in equilibrium with a constant background pressure of water in the vacuum chamber. The emitter tip conditions used in this work provide an environment for investigating ion cluster formation from a liquid-like water layer with control over applied field, tip temperature, and water flux under steady state conditions.

Field desorbed ions were mass resolved using a Wien filter and monitored in real time without perturbing the system. Mass resolved, ramped field ionization was performed over a range of temperatures from 170 to 300 K. This provided insight into the field dependence of ion cluster emission. Additionally, temperature cycling experiments were performed at constant fields to examine proton solvation energies of small clusters.

5.1 Experimental Procedure

Three series of tests were conducted to characterize water ion cluster formation in a field-adsorbed water layer on the platinum emitter tip. In the

first, ramped field ionization experiments were performed to determine the onset of ionization threshold from the field adsorbed water layer. In the second, the Wien filter was used for mass selecting a particular water cluster ion signal for a series of isothermal ramped field ionization and desorption experiments. For the third, the tip potential was held constant at the ion signal maximum while the temperature was cycled for each of a series of selected masses.

Prior to all testing, the Pt emitter tip was field cleaned and imaged with neon gas. Cleaning was accomplished by field evaporating a small amount of Pt from the surface, while visually inspecting the imaged surface until it appeared atomically clean and structured. Simple annealing of the tip is not sufficient for removing all contaminants from the surfaces - particularly carbon. Field cleaning ensures complete removal of surface contaminants prior to testing and reduces the possibility of undesired surface reactions or interactions. During field cleaning, several layers of Pt were field evaporated and the tip crystalline structure was visually inspected to guarantee pristine tip conditions. During imaging, the best imaging voltage (BIV) was recorded and used to estimate the tip radius.

5.1.1 Full Spectrum Ramped Field Ionization and Desorption

After imaging and field cleaning, the tip potential V_t and counter electrode potential V_{CE} were set to +3 kV. To maintain a constant ion formation potential with respect to ground, the tip potential was held constant while the counter electrode potential was ramped negatively to increase the

local field. The ion signal from the tip was focused on the imaging MCPs for PC data acquisition. The tip was resistively heated to the desired temperature, ranging from 170 to 270 K. Water was introduced into the system at the desired partial pressure, ranging from $1 \cdot 10^{-8}$ Torr to $5 \cdot 10^{-6}$ Torr. The counter electrode potential was ramped from +3000 V to 0 V at a rate of 10 V/s.

5.1.2 Mass Selected Ramped Field Ionization and Desorption

For this series of experiments, tip potential and counter electrode potential were again set to +3 kV. The field was increased by ramping the counter electrode potential while maintaining a constant tip potential and consequently a constant ion formation potential. The constant ion formation potential is important for both lens focusing and consistent Wien filter results. The cryo-cooled tip was then resistively heated to the desired experimental temperature, ranging from 180 to 300 K. This temperature range is above the field free condensation temperature for water on platinum, typically 165 K depending on pressure. Water was then introduced into the chamber at a pressure of $5 \cdot 10^{-6}$ Torr. The Wien filter was tuned to select a particular ion mass. The counter electrode potential was ramped from +3000 V to 0 V at a rate of 10 V/s. A computer data acquisition system recorded the mass selected ion signal as a function of potential. The Wien filter was then tuned to a different mass, and the ramping procedure was repeated. Three or more experiments for each tested mass were performed in 10 K increments from 180 to 300 K.

5.1.3 Mass Selected Field Ionization and Desorption with Temperature Cycling

These experiments were performed in a fashion similar to the ramped field experiments described above with a few notable exceptions. The counter electrode potential for each experiment was set to the potential that provided the optimal ion signal for the desired water cluster. The Wien filter was again tuned to isolate the ion signal for the selected mass. Prior to introducing water at a partial pressure of $5 \cdot 10^{-6}$ Torr, the tip was heated to 300 K. This temperature prohibited formation of water ion clusters with *n* greater than 2. The temperature, regulated with a computer controller card[93], was then ramped down to 170 K and slowly cycled between 170 K and a temperature above the maximum cluster formation temperature for the selected mass: 300 K for $H^+(H_2O)_3$, 260 K for $H^+(H_2O)_4$, and 240 K for $H^+(H_2O)_5$. Each full cycle lasted 10 minutes. Typically, 5 cycles were run consecutively for a given mass, after which the tip was heated above 300 K and briefly field cleaned at 3 kV before beginning the next series of cycles. The ion signal was sampled twice per second by the computer and recorded along with the time and tip temperature.

5.2 Results

The ramped field ionization and desorption experiments for temperatures ranging from 170 to 270 K are given in Fig. 5-1. The results shown are a variety of replicate spectra over a range of pressures, resulting in variation of ion intensity between depicted runs at each temperature. The onset of ionization occurs at higher fields for higher temperatures.

The mass selected ramped field ionization and desorption experiments revealed ion cluster formation dependencies on both tip temperature and applied field. Fig. 5-2 depicts the ion signals for detected water clusters at 180 K and 230 K as a function of applied field. The graph represents signal averaged data for three or more runs per mass. At low temperatures, $H^+(H_2O)_n$ ion clusters were detected for *n* up to 7. The large *n* ion clusters were favored at lower field strengths. As the field increases, each ion cluster gives way to the next lower cluster number until the onset of direct ionization of H_2O to form H_2O^+. At the higher temperature, the same progression through the ion clusters occurs, though large ion cluster signals are diminished or absent entirely. Although the amplitude of the ion signal for a given mass varies significantly with temperature, the field dependence of the cluster formation does not. These results allowed us to determine field and temperature conditions that strongly favored the formation of particular ion cluster types.

The results of the mass selected ramped field ionizations for mass 73, the $H^+(H_2O)_4$ ion cluster, for temperature 180 K to 230 K are compared in Fig. 5-3. The onset and peak of cluster emission do not vary significantly as a function of temperature, however the peak height declines at higher temperatures.

Fig. 5-4 illustrates typical experimental temperature dependencies of the ion signals for masses 55, 73, and 91 at their respective optimal signal potentials as determined from Fig. 5-2. The initial temperature was chosen above the range where ion formation was observed. As the temperature

decreases linearly with time, the ion signal increases for each mass. After reaching a minimum temperature, chosen to remain above the field free condensation point, the temperature was increased, resulting in a decrease in ion signal, as expected. No hysteresis effects were observed in our experiments.

The ion signal versus inverse temperature was plotted using data from approximately 15 cycles for each of the three masses. This provides an Arrhenius type plot, shown in Fig. 5-5, which can be used to determine activation energies for each of the cluster formation events. The apparent activation energies (as determined from the line slopes) for ion clusters n = 3, 4, and 5 were 0.85 ± 0.03, 0.76 ± 0.02, and 0.55 ± 0.02 eV, respectively. The slopes shown are positive and differ from typical Arrhenius plots, suggesting thermal deactivation of the cluster emission. Higher mass clusters (n > 5) were not present over a wide enough temperature range to extract activation energies. Lower mass clusters (n < 3) were present over the entire experimental range and were therefore not suited for the same Arrhenius analysis.

Mass selected ramped field desorptions for O_2^+ ions are shown in Fig. 5-6 for temperatures ranging from 180 K to 300 K. These tests were performed at a water partial pressure of $5 \cdot 10^{-7}$ Torr. The signal intensity for these experiments was much lower than the observed intensities of the other ions.

5.3 Discussion

5.3.1 Ion Cluster Emission

The onset of ionization for ramped field desorption from a field adsorbed water layer moves to higher fields with increasing temperature as shown in Fig. 5-1. This is in stark contrast to the results of Scovell, et al.[87] which show a decreased onset field with increasing temperatures from adsorbed ice layers at low temperatures.

The results of the mass selected ramped field ionization experiments in Fig. 5-2 show that the field necessary for emitting ion clusters varies with ion cluster size. Large ion clusters are more easily emitted than small clusters and were consequently observed at much lower fields. The field required for emission of a specific ion did not vary significantly between the two temperatures, although the ion current for the higher masses diminished at higher temperatures. The ease of cluster emission depends on the difference in energy between the solvated proton in the water layer on the surface and the proton solvated by *n* water molecules in vacuum near the surface. Fig. 5-7 qualitatively illustrates the behavior of the energy barriers at 0.3 and 0.9 V/Å for cluster emission in the presence of a strong field. The field free energies necessary for removing a given ion cluster were calculated with a thermodynamic cycle. For example, a proton near the water surface may be created by first removing a water molecule from the bulk by providing the latent heat of vaporization λ_v of 0.44 eV [28],

$$^{\ell}H_2O \rightarrow {}^{v}H_2O \qquad (5.1)$$

dissociating it in vacuum with a dissociation energy E_D of 5.11 eV [94],

$$^{v}\mathrm{H_2O} \rightarrow {}^{v}\mathrm{H} + {}^{v}\mathrm{OH} \tag{5.2}$$

ionizing the hydrogen with an ionization potential I_P of 13.6 eV [28],

$$^{v}\mathrm{H} + {}^{v}\mathrm{OH} \rightarrow {}^{v}\mathrm{H^+} + {}^{v}\mathrm{OH} + e^- \tag{5.3}$$

transferring the free electron to the OH with an electron affinity E_A of -1.83 eV (here given as negative for consistency) [28],

$$^{v}\mathrm{H^+} + {}^{v}\mathrm{OH} + e^- \rightarrow {}^{v}\mathrm{H^+} + {}^{v}\mathrm{OH^-} \tag{5.4}$$

and then solvating the hydroxide ion with a solvation energy of E_{solv}^{OH-} of -4.77 eV [59].

$$^{v}\mathrm{H^+} + {}^{v}\mathrm{OH^-} \rightarrow {}^{v}\mathrm{H^+} + {}^{\ell}\mathrm{OH^-} \tag{5.5}$$

Summing the energies

$$\Delta E_{emit}^{H+} = \lambda_v + E_D + I_P + E_A + E_{solv}^{OH-} \tag{5.6}$$

results in a total energy ΔE_{emit}^{H+} of 12.55 eV for the emission of a proton from bulk water. Solvating the proton,

$$^{v}\mathrm{H^+} \rightarrow {}^{\ell}\mathrm{H^+} \tag{5.7}$$

results in an initial energy of 0.7 eV[87]. This initial state assumes infinite solvation ($n \rightarrow \infty$), which may not be the case on the Pt surface, although the Pt surface itself may act to solvate the proton to some extent. Energies for ion clusters of different n may then be calculated by accounting for the additional energy of solvation [57] of the emitted proton by the n water molecules, minus the energy required to remove the water molecules from the bulk according to,

$$\Delta E_{emit}^{n} = \Delta E_{emit}^{n-1} + \Delta E_{solv}^{n} + \lambda_v \tag{5.8}$$

where ΔE_{emit}^{n} is the energy barrier for cluster n emission and ΔE_{solv}^{n} is the solvation energy due to the nth solvating water molecule. The values for the first several ion clusters are tabulated in Table 5-1.

As Fig. 5-7 demonstrates, the energy barrier for ion emission is formed by a combination of the image potential and the field lines. The image potential V_I is described by,

$$V_I = \frac{e^2}{4x}\left(\frac{\varepsilon - 1}{\varepsilon + 1}\right) \tag{5.9}$$

where ε is the relative permittivity and x the distance from the surface [95]. This expression is for a point charge approaching a perfectly smooth flat surface, and is therefore only an approximation for the emitter tip. It is nonetheless reasonable when comparing the thickness of less than 10 Å for thin water layers to the tip diameter ~350 Å. Additionally, the image force expression has a singularity at the water-vacuum interface and consequently fails within the first Ångstrom, but this is acceptable for a qualitative consideration of the energy barrier peak, which occurs beyond the first Ångstrom. The field is approximately linear near the water vacuum interface for a thin water layer [15] and is shown as such. The energy barriers under field free conditions for clusters n = 1-4 are depicted by dashed lines at the top of each diagram. A solid line shows the emission barrier E_b due to the combined field and image forces (neglecting higher order terms) for each cluster given by,

$$E_b(x) \cong \Delta E_{emit} - xF - V_I(x)\,. \tag{5.10}$$

As shown, the energy barriers are confronted by a solvated proton at 0.7 eV in the water layer on the tip. This initial energy is the same as the thermal barrier for H_2O ionization discussed earlier. At low fields the barriers are high and wide. As the field increases, the barrier narrows and decreases. Thermally activated emission may occur depending on the barrier height. When the emission barrier for a given cluster falls below the potential energy of the solvated proton, emission occurs freely. As the field increases further, the emission barriers for each cluster *n* in turn drop below the solvated proton potential and become energetically accessible.

It is important to note that the applied field shown in Fig. 5-7 is idealized. The local field at the ion cluster emission point may be enhanced due to the formation of localized humps on the surface where the water supply function appears to be concentrated. In addition to the influence of localization on the energetics of emission, localization plays a role in the kinetics of the cluster formation. While large *n* cluster emission is energetically favorable, kinetically it is more difficult to achieve because it requires further solvation. Consequently, the lowest *n* cluster that is energetically accessible at a given field and temperature will dominate the ion emission signal. This is observed in the results of the ramped field ionization experiments shown in Fig. 5-2. When cluster *n* emission is observed to decay during the field ramp, cluster *n*-1 emission begins. Cluster *n* emission is still energetically favorable, but the cluster is capable of overcoming the emission barrier after reaching *n*-1. For example, the peak of cluster 3 emission occurs

at an applied field of 0.43 V/Å, the same field as the onset of emission for cluster 2. As cluster 2 emission increases, cluster 3 emission decays, even though cluster 3 emission is still energetically favorable.

5.3.2 Temperature Dependence and Solvation Energy

A comparison of the ion emission signal heights of the 180 K and 230 K ramped field ionization experiments in Figure 5-2 for large *n* clusters shows a dependence of signal intensity on tip temperature. At higher temperatures the large *n* cluster emission was diminished, even though the required emission fields were equal. Figure 5-3 shows the mass selected RFD peaks for the $n = 4$ cluster in detail. This peak is strong at temperatures below 220 K, but is nearly absent at 230 K and is not present above that temperature. By maintaining the tip at a constant field selected to optimize a chosen cluster and cyclically ramping the temperature, the temperature dependence of the emission amplitude was observed, as illustrated by Figures 5-2 and 5-3. An added benefit of these constant field experiments is that the water supply to the tip is relatively constant, as opposed to the ramped field ionization experiments where the flux of water to the tip is influenced by the applied field.

From the Arrhenius plots in Fig. 5-5, several observations may be made about the behavior of the ion clusters. While the signal for the $n = 5$ cluster diminishes with increasing temperature, the $n = 4$ signal remains saturated. As the $n = 5$ fades away completely, the $n = 4$ signal begins to decay, although the $n = 3$ remains saturated. Finally, when the $n = 4$ emission ceases, the $n =$

3 signal decays. That is, there is continuity in the progression of the decay with temperature of the ion signals from one cluster to the next. The decrease in emission signal with increased temperature is in contrast to traditional Arrhenius plots depicting temperature activated reactions. For these data, ion emission appears to be a thermally *deactivated* event. This suggests an alternate pathway to field ionization that depends strongly on temperature and consequently shuts down the emission event as the thermally activated alternate pathway begins to dominate.

An examination of the surface behavior of an adsorbed protonated water cluster provides an explanation for this observed thermal deactivation. There are three primary reactions governing the ion formation and emission processes. These reactions are illustrated in Fig. 5-8a. The first of these reactions,

$$H_2O^* \xleftrightarrow{r_a} H_2O \tag{5.11}$$

governs the supply of water to the surface, where H_2O^* is gas phase water and H_2O is surface adsorbed water and not part of an ion solvation shell. Reactants discussed hereafter are surface adsorbed unless denoted by an asterisk to indicate gas phase. The net reaction rate r_a may be expressed as

$$r_a = k_1 p_w - k_2 \theta_w \tag{5.12}$$

where k_1 and k_2 are reaction rate constants, p_w the water partial pressure, and θ_w the surface water coverage for sub-monolayer quantities only. For multilayers cases θ_w will be constant. This equation may be equivalently restated as

$$r_a = NS - k_2\theta_w \tag{5.13}$$

where N is the incident water flux and S is the sticking coefficient. The remaining rate constant is given by

$$k_2 = A_2 e^{-\lambda_v/kT} \tag{5.14}$$

where A_2 is a pre-exponential factor. Although λ_v for water on platinum is not exactly equal to the value for bulk water, the difference is not significant for these calculations.

If we consider the case where a variety of clusters has already formed on the surface, the second reaction equation,

$$H^+(H_2O)_{n-1} + H_2O \xleftrightarrow{r_b^{(n)}} H^+(H_2O)_n \tag{5.15}$$

accounts for the solvation of the protonated water molecule with the transition of the solvation shell from n-1 to n and is depicted specifically in Fig. 5-8b. The net rate of this reaction,

$$r_b^{(n)} = k_3^{(n)}\theta_{n-1}\theta_w - k_4^{(n)}\theta_n \tag{5.16}$$

and the corresponding rate constants, k_3 and k_4, vary with n and are superscripted accordingly. θ_n represents the surface coverage by n solvated proton clusters, i.e. $H^+(H_2O)_n$. θ_w once again assumes sub-monolayer coverages. The forward reaction constant, given by

$$k_3^{(n)} = A_3^{(n)} e^{-E_A^{(n)}/kT} \tag{5.17}$$

has a low activation barrier $E_A^{(n)}$ as water readily solvates the proton under experimental conditions and should proceed rapidly. The forward reaction is exothermic and will release the excess energy of solvation $\lambda_E^{(n)}$ which is the

difference in energy between the water molecule as the nth member of the solvation shell, and the water molecule on the surface with no role in solvation. The rate constant for the desolvation reaction, stepping from *n* to *n*-1, is given by

$$k_4^{(n)} = A_4^n e^{-(E_A^{(n)} + \lambda_2^{(n)})/kT} \tag{5.18}$$

The energy barrier for the reverse reaction is higher than that of the forward reaction by the value of the excess energy of solvation.

The third reaction of interest is the ion emission event,

$$\mathrm{H^+(H_2O)}_n \xrightarrow{r_c^{(n,m)}} \mathrm{H^+(H_2O)}^*_{m\le n} + (n-m)\mathrm{H_2O} \tag{5.19}$$

where a cluster of size $m \le n$ is emitted from a cluster of size n on the surface, leaving behind n-m surface adsorbed water molecules. This reaction is, for all practical purposes, irreversible in the presence of a strong applied field, and may therefore be given by

$$r_c^{(n,m)} = k_5^{(n,m)}\theta_n \tag{5.20}$$

where the doubly superscripted reaction rates and constants depend on both the initial surface cluster size and the size of the emitted ion cluster. The reaction constant may be written as

$$k_5^{(n,m)} = A_5^{(n,m)} \exp\left(\frac{-E_{Emit}^{(n,m)}(F)}{kT}\right) \tag{5.21}$$

where the activation barrier $E_{Emit}^{(n,m)}$ is a strongly field dependent value as suggested by Figures 5-1 and 5-4 $E_{Emit}^{(n,m)}$ is equivalent to E_b mentioned earlier

while discussing emission barriers, but accounts for the incomplete solvation of the surface ion with the double superscript.

Four additional reaction equations are necessary for completion. The first is the dissociative ion formation event,

$$H_2O \xrightarrow{r_d} H^+ + OH^- . \qquad (5.22)$$

This reaction is temperature and field dependent. The rate may be estimated for our experimental conditions using methods outlined by Pinkerton et al. [98]. For tested experimental conditions, the field remains well above the extrapolated dissociation barrier, suggesting that the ion emission rate is not rate limiting.

The second equation is the electron discharge at the tip surface,

$$OH^- \xrightarrow{r_e} OH + e^-_{Pt} . \qquad (5.23)$$

Conservation of charge at equilibrium dictates that the reaction rate of Equation 5.23 will be equal to the total ion emission rate. Accounting for the buildup of OH on the surface provides the reaction equation

$$2OH \xrightarrow{r_f} H_2O + O . \qquad (5.24)$$

The fate of the atomic oxygen on the surface is not known for certain. It may diffuse up the tip shank, recombine with neutralized hydrogen (if available) or, at high fields, ionize and desorb from the Pt tip according to the reaction,

$$2O \xrightarrow{r_g} O_2^{+*} + e^-_{Pt} \qquad (5.25)$$

as suggested by Ernst, et al. [87]. The mass selected ramped field desorption experiments isolating O_2^+ shown in Fig. 5-6 show that this ionization is possible at fields greater than 1.0 V/Å at all tested temperatures, yet the signal intensity for the oxygen was quite small. The exact mechanism, however, does not prove important to the steady state calculation.

The rate of change of water on the tip surface may be expressed using the rate equations given above. This results in the differential equation

$$\frac{d\theta_w}{dt} = r_a - \sum_0^\infty r_b^{(i)} + \sum_{i=1}^\infty \sum_{j=1}^i (i-j) r_c^{(i,j)} - r_d + r_f \qquad (5.26)$$

where the first term on the right hand side of the equation accounts for the adsorption/desorption flux, the second for the summation of the solvation reactions, the third for the water left behind by all of the emission events, and the final two terms due to the dissociative ionization and OH recombination events, respectively. By varying the temperature very slowly and maintaining constant tip potential during testing, the tip surface may be assumed to be at steady state. This allows us to set the time derivative to zero. Additionally, it allows us to set serial pathways at equal rates (while accounting for stoichiometric multipliers). By setting the tip to conditions where emission of only one cluster type dominates and occurs readily, ion emission will be restricted to the case where $n = i = j$, thereby eliminating the third term from the equation. The water dissociation rate r_d is not rate limiting and is therefore taken at equilibrium and may be set equal to $r_b^{(n)}$. The OH recombination reaction also must be at equilibrium resulting in r_f equal to $^1/_2$

$r_b^{(n)}$. Since emission will not proceed until the nth solvation is reached, n solvation events must occur per emission event. When we take these as serial events and take into consideration the fact that the ion emission event is a one-to-one function of the rate of formation of n size clusters at steady state we may simplify the equation and are left with

$$r_a - \left(n + \tfrac{1}{2}\right) r_b^{(n)} = 0 . \tag{5.27}$$

Plugging in the equations for the rate constants and solving for the surface coverage of water, θ_w, gives

$$\theta_w = \frac{NS + (n + \tfrac{1}{2})\theta_n k_4^{(n)}}{k_2 + (n + \tfrac{1}{2})\theta_{n-1} k_3^{(n)}} . \tag{5.28}$$

Next, we turn to the rate of change of the surface population of n solvated protons, which is described by the differential equation

$$\frac{d\theta_n}{dt} = r_b^{(n)} - r_b^{(n+1)} - \sum_{i=0}^{n} r_c^{(n,i)} . \tag{5.29}$$

Again, we take the system at conditions optimal for forming ion clusters of size n only. Since emission of cluster n+1 is more easily accomplished than emission of cluster n, failure to emit size n+1 clusters allows us to assume $r_b^{(n+1)} << r_b^{(n)}$ and that the summation term is approximately $r_c^{(n,n)}$ (hereafter referred to as $r_c^{(n)}$). This reduces the equation to

$$\frac{d\theta_n}{dt} \cong r_b^{(n)} - r_c^{(n)} . \tag{5.30}$$

With the tip at steady state conditions we further reduce this to

$$r_b^{(n)} - r_c^{(n)} = 0 . \tag{5.31}$$

Substituting the rate equations provides

$$k_3^{(n)}\theta_{n-1}\theta_w - k_4^{(n)}\theta_n - k_5^{(n)}\theta_n = 0\,. \tag{5.32}$$

Rearranging and solving for the surface coverage of *n* solvated proton clusters gives

$$\theta_n = \theta_w \frac{k_3^{(n)}\theta_{n-1}}{k_4^{(n)} + k_5^{(n)}} \tag{5.33}$$

Now substituting Equation 5.28 into Equation 5.33 gives

$$\theta_n = \frac{NS + (n+\frac{1}{2})\theta_n k_4^{(n)}}{k_2 + (n+\frac{1}{2})\theta_{n-1}k_3^{(n)}} \times \frac{k_3^{(n)}\theta_{n-1}}{k_4^{(n)} + k_5^{(n)}} \tag{5.34}$$

Again, solving for the surface coverage of *n* solvated proton clusters and rearranging gives the explicit result,

$$\theta_n = \frac{N \cdot S}{k_5^{(n)}}\left(\frac{k_2^{(n)}k_4^{(n)}}{k_3^{(n)}k_5^{(n)}\theta_{n-1}} + \frac{k_2^{(n)}}{k_3^{(n)}\theta_{n-1}} + n + \frac{1}{2}\right)^{-1}. \tag{5.35}$$

Substituting this equation into the rate equation for ion emission (Eq. 20) and dividing through by the water flux term yields a dimensionless ion emission rate

$$\frac{r_c^{(n)}}{N \cdot S} = \left(\frac{k_2^{(n)}k_4^{(n)}}{k_3^{(n)}k_5^{(n)}\theta_{n-1}} + \frac{k_2^{(n)}}{k_3^{(n)}\theta_{n-1}} + n + \frac{1}{2}\right)^{-1}. \tag{5.36}$$

Substituting in the equations for each rate constant and rearranging leads to

$$\frac{r_c^{(n)}}{NS} = \left[\frac{A_2}{A_3^{(n)}\theta_{n-1}}\left(\frac{A_4^{(n)}}{A_5^{(n)}}e^{-(\lambda_v+\lambda_E^{(n)}-E_{Emit}^{(n)}(F))/kT} + e^{-(\lambda_v - E_A^{(n)})/kT}\right) + n + \frac{1}{2}\right]^{-1}. \tag{5.37}$$

For fields where ion emission is facile for a given cluster *n*, $E_{Emit}^{(n)} << \lambda_v + \lambda_E^{(n)}$. If it were not, signal from the *n*-1 cluster would also be observed.

Additionally $A_4^{(n)}$ >> $A_5^{(n)}$, since the time-scale for oscillation of one water molecule in a cluster is much smaller than the time-scale for an escape attempt of several molecules in concert. As a result, the first exponential term dominates the second, allowing us to neglect the latter. The sum $\lambda_v + \lambda_E^{(n)}$ is the vaporization energy plus the excess solvation energy which is the negative of the overall solvation energy for the nth water molecule, $E_{Solv}^{(n)}$ from Equation 8. If we define

$$\kappa^{(n)} = \frac{A_2 A_4^{(n)}}{A_3^{(n)} A_5^{(n)} \theta_{n-1}}, \tag{5.38}$$

these assumptions allow us to simplify Equation 5.37 to provide

$$\frac{r_c^{(n)}}{N \cdot S} \cong \frac{1}{\kappa^{(n)} e^{-\left(\lambda_v + \lambda_E^{(n)}\right)/kT} + n + \frac{1}{2}}. \tag{5.39}$$

Equation 5.39 provides the functional form of the $H^+(H_2O)_n$ ion cluster emission rate equation for a constant optimal field. It contains a thermally activated reaction with an activation barrier equal to the solvation energy provided by the nth solvating water molecule in the denominator. An equation describing the actual experimental ion signal illustrated in Fig. 5-5 would require multiplication of the right hand side by a field dependent instrumentation constant. At low temperatures (while remaining above the condensation point) the ion emission rate is maximized and constant with

$$\frac{r_c^{(n)}}{N \cdot S} \cong \frac{1}{n + \frac{1}{2}} \qquad \lim T \rightarrow 0. \tag{5.40}$$

This predicts the plateaus observed in Fig. 5-5, although absolute calibration of the ion signal is very difficult due to variations in ion collection efficiency with counter electrode potential. As the temperature increases, the exponential term begins to dominate the denominator, and the ion signal decays according to

$$\frac{r_c^{(n)}}{N \cdot S} \cong \frac{1}{\kappa^{(n)}} e^{\left(\lambda_v + \lambda_E^{(n)}\right)/kT} \qquad \lim T \rightarrow \infty. \qquad (5.41)$$

This form explains the unusual thermal deactivation of the ion emission event as well as the slope of the decay being equal to the solvation energy. The energy term in the exponential in Equation 5.41, $\lambda_v + \lambda_E^{(n)}$, corresponds to the energy required for removing the nth solvating water molecule from the surface adsorbed protonated water cluster, to the surface, and then into the vacuum. This is equivalent to the total solvation energy provided to the surface adsorbed protonated water cluster by the nth solvating water molecule, which are given in Table 5-1. Table 5-1 shows the peak appearance field, literature and experimental solvation energies and calculated emission barriers for the first 7 protonated water clusters.

5.4 Conclusions

Water ion cluster $\{H^+(H_2O)_n\}$ formation and emission from a field adsorbed water layer on a Pt emitter tip was characterized for temperatures ranging from 170 K to 300 K. Mass resolved ramped field ionization experiments revealed a field dependence of ion cluster emission that varied with cluster mass. Large clusters were observed at lower field strengths. As

the field increases, the cluster size decreases to successively lower values. This behavior is attributed to the tradeoff between the energetic favorabilty of large n cluster emission and the kinetic favorability of small n cluster emission. A comparison of the ion signals at different temperatures showed that the field required for emission of a specific cluster varied little with temperature, while the ion signal decayed with temperature. Constant field temperature cycling experiments provided Arrhenius plots showing thermal deactivation of ion emission for cluster sizes of n = 3, 4 and 5 with energies of 0.85, 0.76 and 0.55 eV, respectively. An analysis of the possible pathways available to an adsorbed ion cluster explains these thermal deactivation energies as those associated with the solvation of the surface adsorbed proton by the nth water molecule.

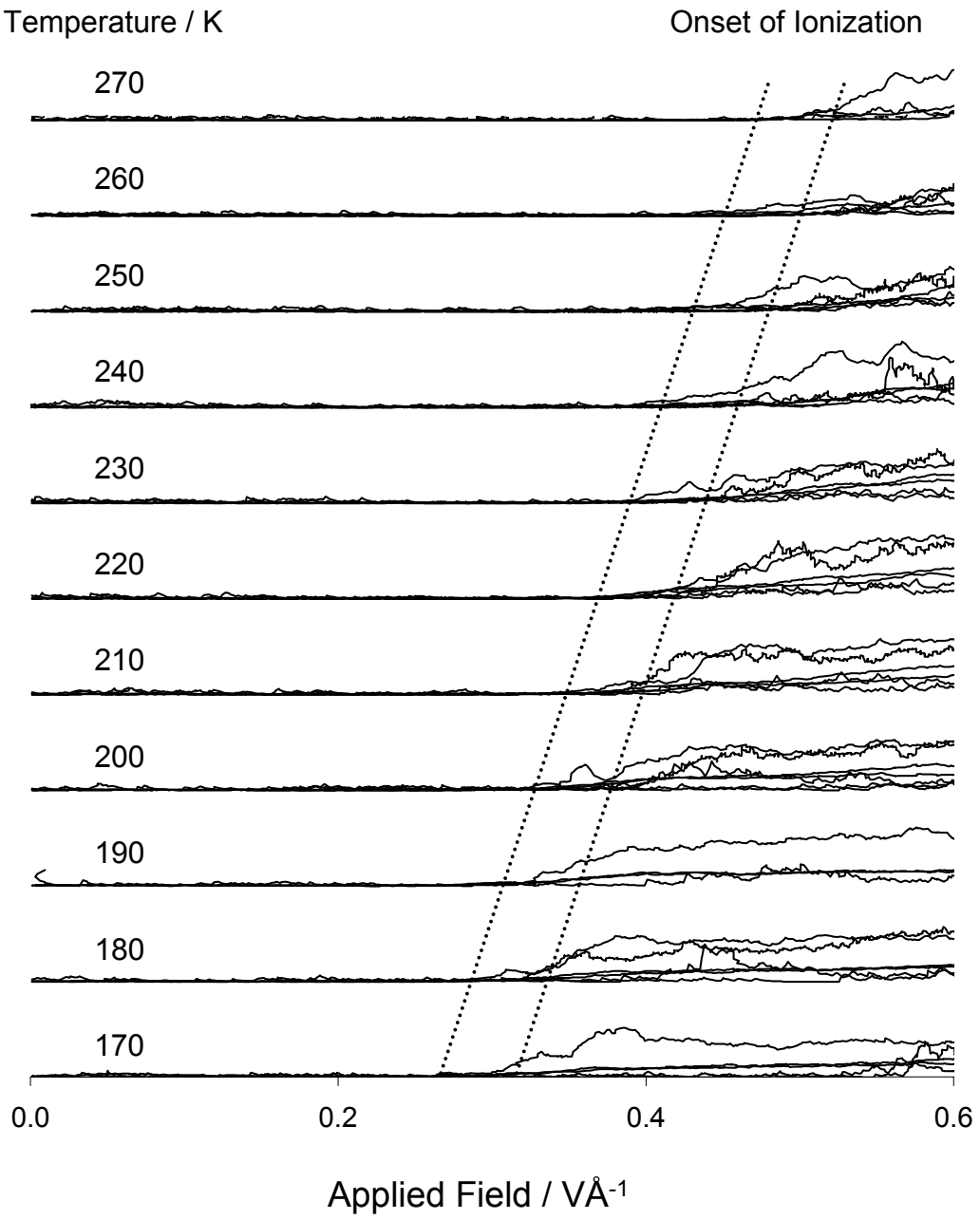

FIGURE 5-1: Onset of ionization for ramped field desorption of water from Pt emitter tip by temperature. Each series shows the full ion signal for numerous tip experimental runs at a variety of water partial pressures from $1x10^{-8}$ to $5x10^{-6}$ Torr.

(a)

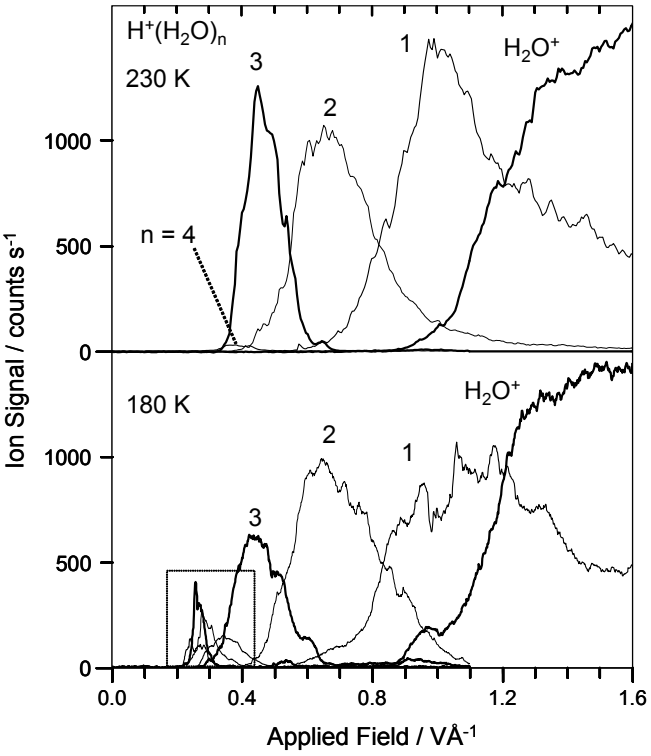

(b)

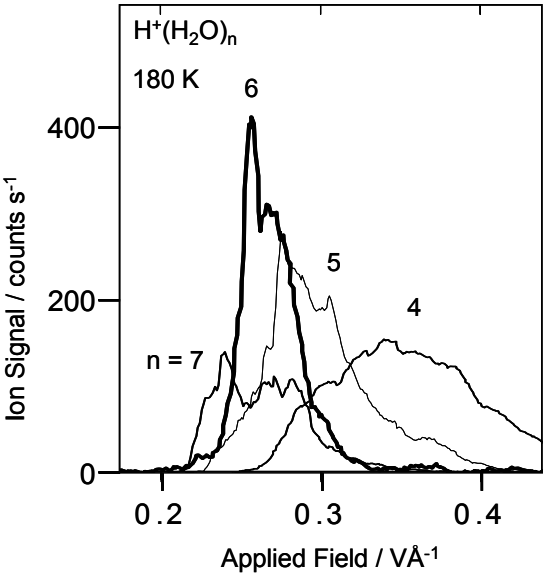

FIGURE 5-2: Mass selected ramped field cluster formation. (a) Protonated water clusters, $H^+(H_2O)_n$, with n up to 7 were observed while ramping the applied field on a Pt emitter tip (~350Å) from 0 to 1.6 V/Å. The experimental background H_2O partial pressure was $5 \cdot 10^{-6}$ Torr. (b) A magnification of the high mass cluster signal for the 180K ramped field experiments.

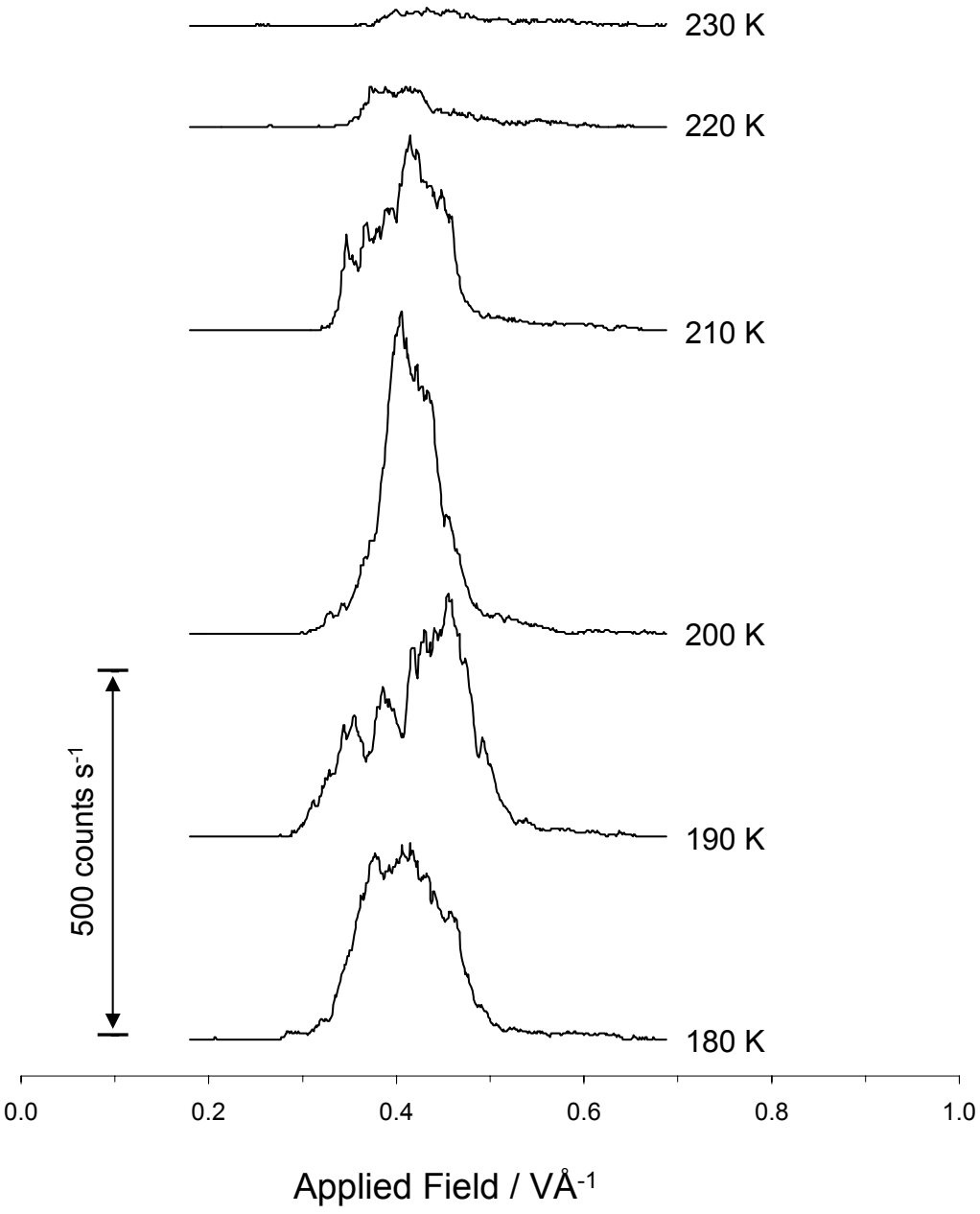

FIGURE 5-3: Mass resolved ramped field ionization of $H^+(H_2O)_4$ for temperatures 180 K to 230 K. $P_{H2O} = 5x10^{-6}$ Torr.

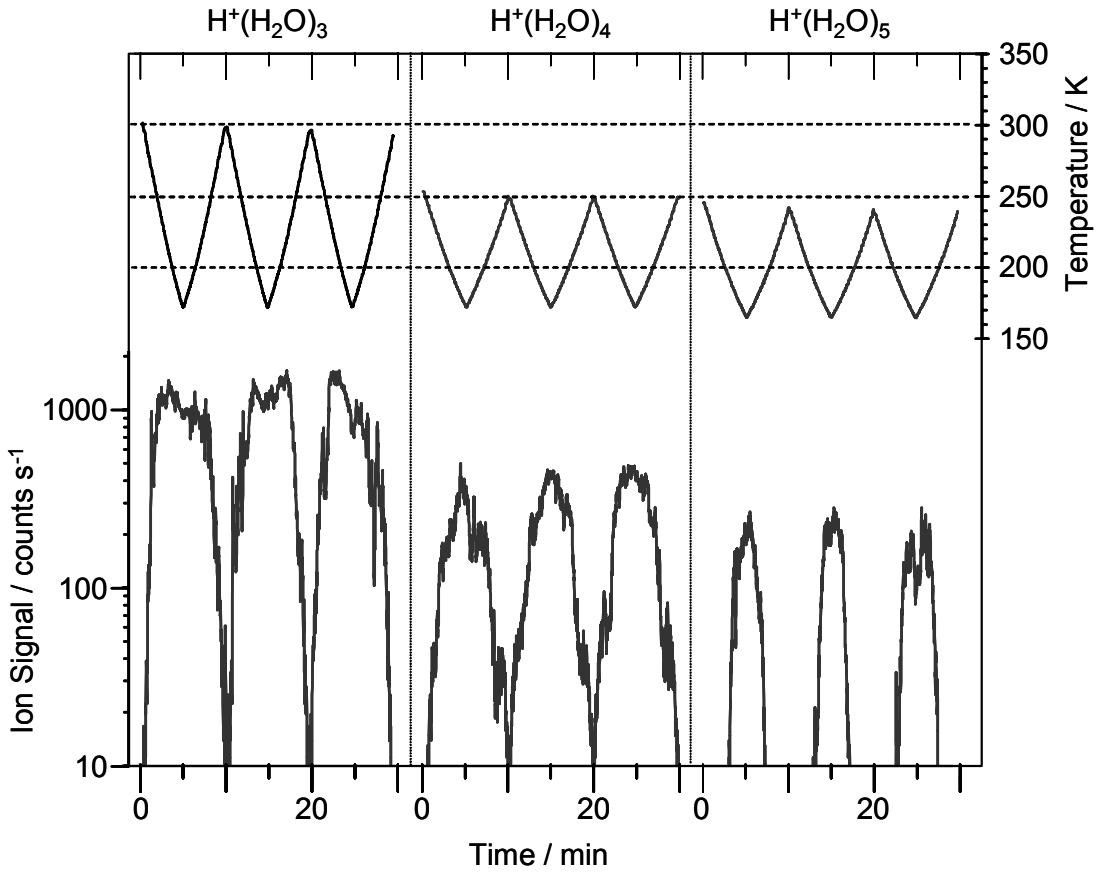

FIGURE 5-4: Typical ion cluster formation dependency during temperature cycling (lower curves). The tip potential was held at the optimal formation potential (see Fig. 5-2) for each respective ion while the temperature of the tip was slowly cycled linearly with time (upper curves).

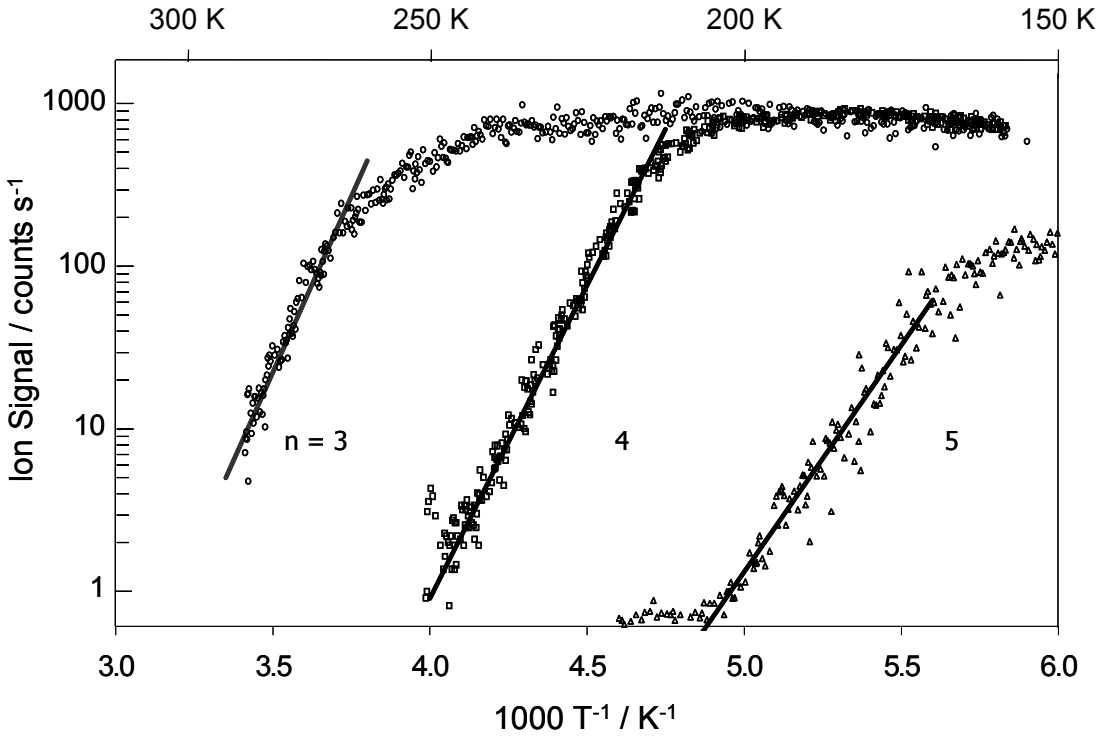

FIGURE 5-5: Arrhenius plot of cluster ion formation during temperature cycling demonstrating thermal *deactivation* of the cluster emission. Deactivation energies determined from the slopes of the solid lines are 0.85 ± 0.03 eV, 0.76 ± 0.02 eV and 0.55 ± 0.02 eV for n = 3, 4 and 5, respectively.

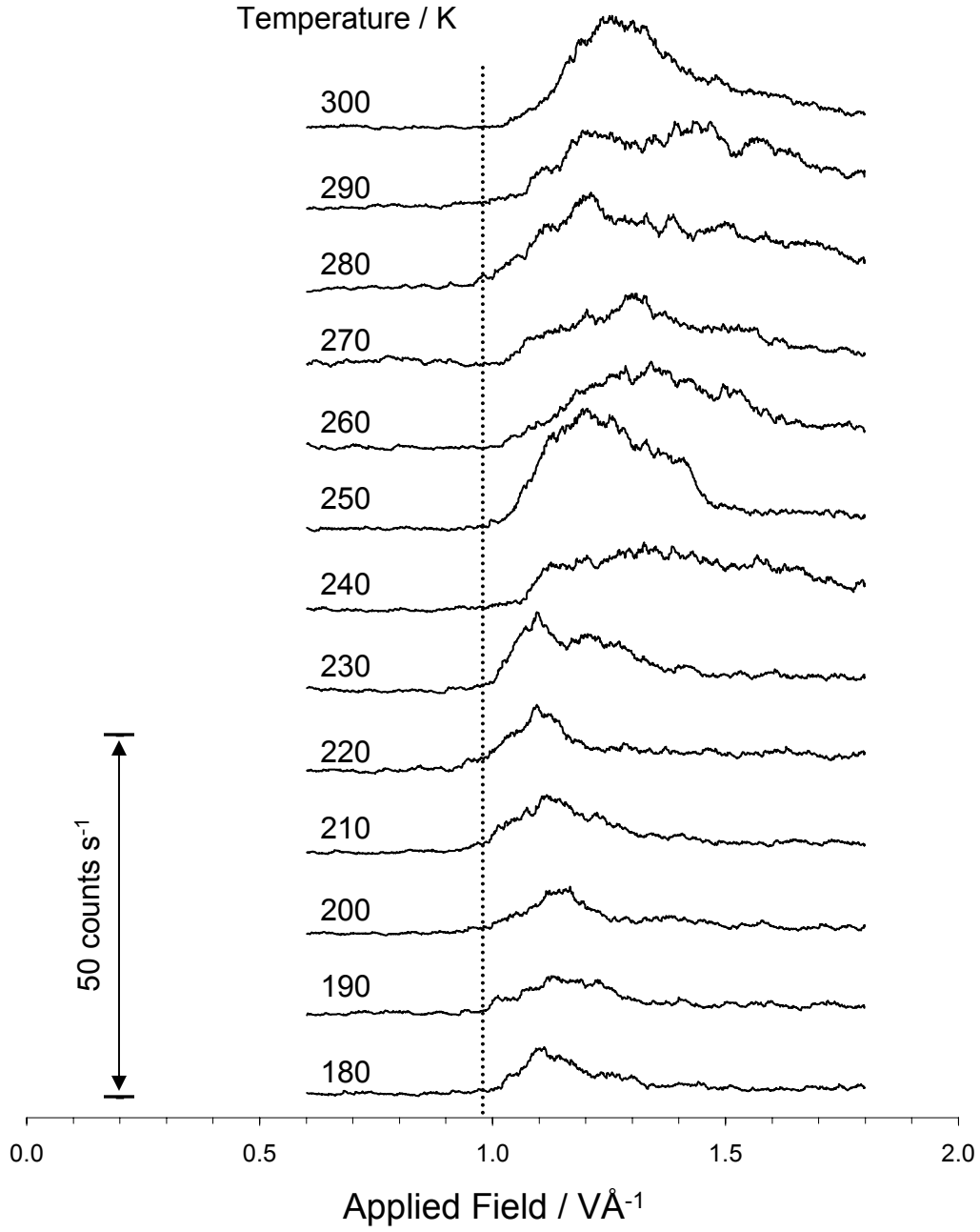

FIGURE 5-6: Mass resolved ramped field desorption of oxygen from Pt emitter tips for temperatures 180 K through 300 K. Tip radius ~ 330 Å. P_{H2O} = 5x10^{-7} Torr.

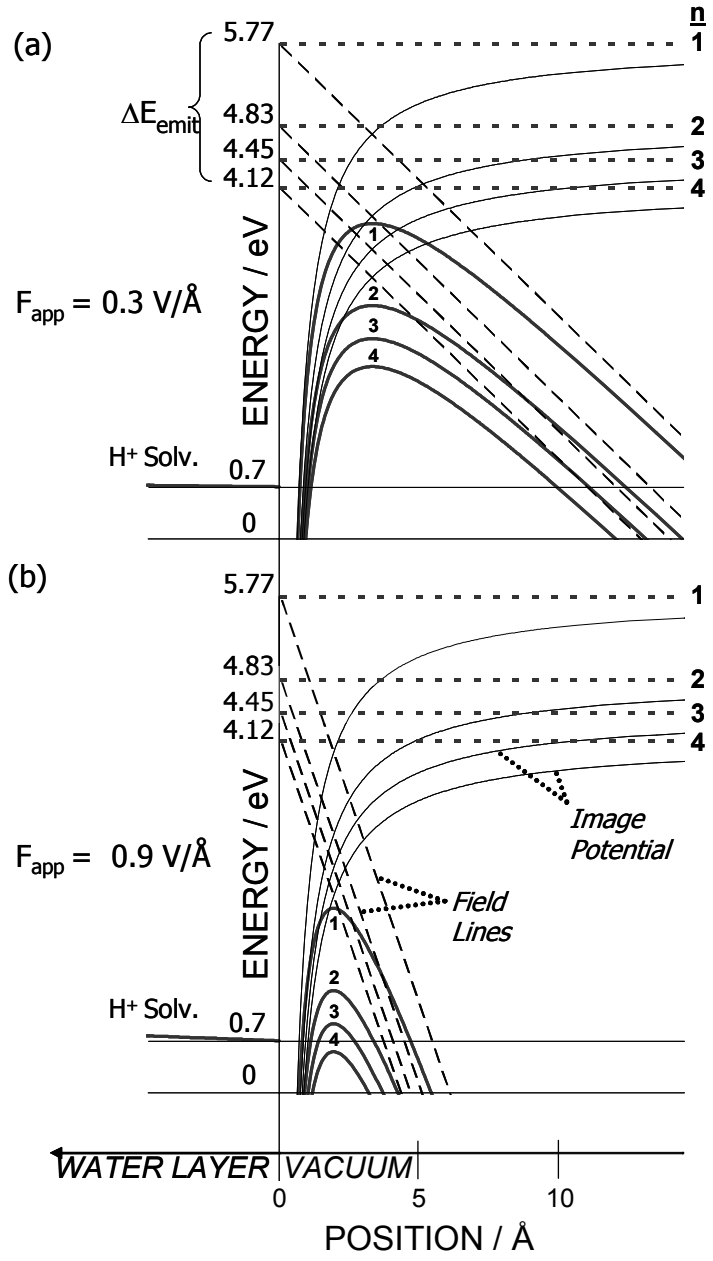

FIGURE 5-7: Field bending of potential energy barriers to ion cluster emission. The energies for emission of clusters *n* = 1-4 under field free conditions are shown by the short dashed lines. Image potential and field lines are illustrated with thin solid and long dashed lines, respectively. Energies are referenced to uncharged water adsorbed on the platinum tip surface. The resulting emission barriers confronted by the solvated proton on the surface are shown by the thick solid curves. As the field increases, the barriers in turn fall below the energy of the solvated proton on the surface.

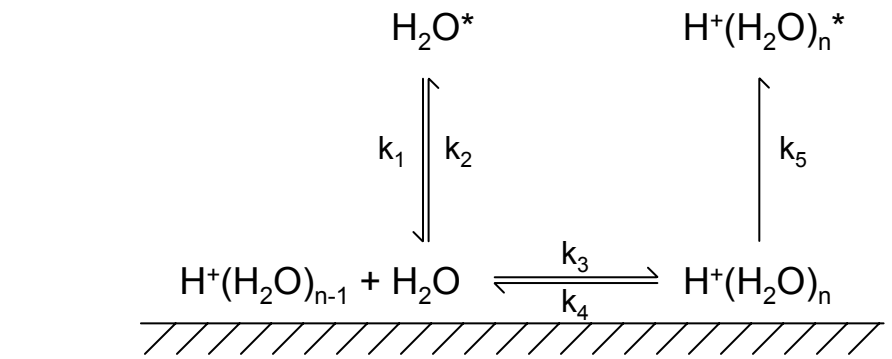

(a)

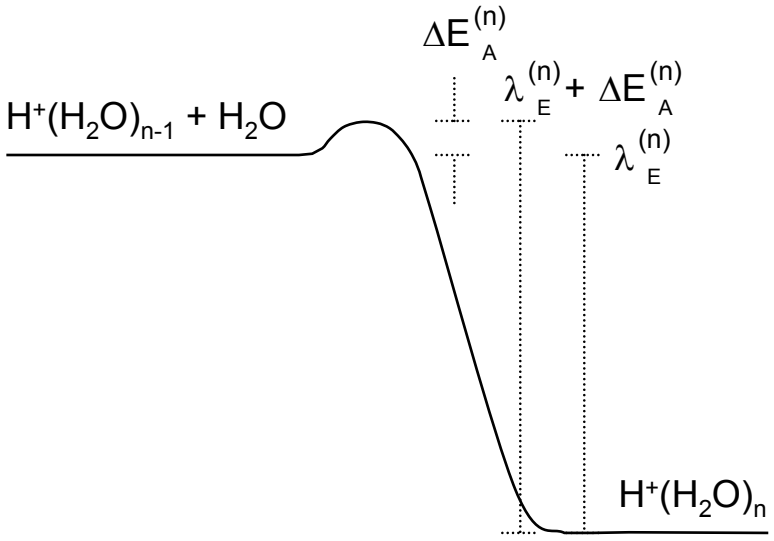

(b)

FIGURE 5-8: Reaction pathways and energies. (a) Possible reaction pathways for an adsorbed water cluster. The cluster may be solvated by additional water molecules (if available), desorb from the surface, or lose a solvating water molecule. (b) Reaction barrier energy diagram for solvation. represents the excess solvation energy of the nth solvating water molecule.

TABLE 5-1: Ion cluster energies and observed formation fields.

	F_{app} [a] V/Å	Lit ΔE_{solv} [b] eV	Exp ΔE_{solv} [c] eV	ΔE_{emit} [d] eV
H^+	n/a	n/a	-	12.55
$H^+(H_2O)$	1.00	-7.22	-	5.77
$H^+(H_2O)_2$	0.64	-1.38	-	4.83
$H^+(H_2O)_3$	0.45	-0.82	-0.85	4.45
$H^+(H_2O)_4$	0.34	-0.76	-0.76	4.12
$H^+(H_2O)_5$	0.29	-0.50	-0.55	4.07
$H^+(H_2O)_6$	0.27	-0.48	-	4.02
$H^+(H_2O)_7$	0.26	-0.46	-	4.00

[a] Optimal observed applied field for cluster formation.

[b] H^+solvation energy associated with *n*-1 to *n* transition. [Meot-Ner, 86]

[c] Experimentally observed solvation energies from Fig. 5-5.

[d] Calculated emission energy based on $\Delta E_{solv}+\lambda_v$ (e.g. $\Delta E_{emit}(n=3)$ = 4.83 eV - 0.82 eV + 0.44 eV = 4.45 eV)

CHAPTER 6: TWO STEP ION CLUSTER DISSOCIATION AND EMISSION

The investigations in Chapter 5 into the temperature and field dependence of protonated water cluster emission from water adlayers on Pt have provided an understanding of the cluster emission behavior. A protonated water cluster may form on the surface through dissociative ionization of a water molecule according to

$$m\mathrm{H_2O} \longrightarrow \mathrm{H^+(H_2O)}_n + \mathrm{OH^-(H_2O)}_{m-n-1} \qquad (6.1)$$

A protonated water cluster residing on the surface has essentially three available pathways. The first possibility is emission,

$$\mathrm{H^+(H_2O)}_n \longrightarrow \mathrm{H^+(H_2O)}^*_{m\le n} + (n-m)\mathrm{H_2O} \qquad (6.2)$$

where n represents the number of water molecules solvating the proton on the surface and m represents the number of water molecules in the emitted ion cluster, which is designated by an asterisk. Emission is a strongly field dependent phenomenon and largely independent of temperature. This independence logically follows from a comparison of the emission energies (typically about 4 eV), and the thermal energy of the tip (~0.02 eV). Calculated emission energies[96] showed a dependence of emission barrier on cluster size in which large clusters are more easily emitted than are small clusters, consistent with the experimental field dependence of ion emission.

The second possibility for the solvated water cluster residing on the tip surface is to associate with an additional surface adsorbed water molecule,

$$H^+(H_2O)_n + H_2O \longrightarrow H^+(H_2O)_{n+1} \qquad (6.3)$$

if another molecule is locally available. This provides additional solvation energy, and proceeds readily at the limit of availability.

The third possibility is thermal desorption of the nth solvating molecule,

$$H^+(H_2O)_n \longrightarrow H^+(H_2O)_{n-1} + H_2O^* . \qquad (6.4)$$

This pathway is thermally activated and almost completely field independent. The nth water molecule is bound to the proton by the solvation energy associated with the transition from $H^+(H_2O)_n$ to $H^+(H_2O)_{n-1}$. With increasing temperature, the extent of solvation of the proton diminishes, and emission of large ion clusters becomes impossible. So it was concluded from our studies that for temperatures from 170 to 300 K, the dominant ion emission clusters were determined by the applied field from a set of possible cluster types, which was determined by the tip temperature.

Pinkerton and Scovell et al. [22, 86-88] investigated ionization thresholds for protonated water clusters using ramped field desorption. For crystalline ice deposited at 145 K and in the limit of zero thickness, they reported a correlation between ionization onset field and tip temperature, with a line break near 130 K and an extrapolated intercept near 210 K (shown in Figure 6-1a). This intercept corresponds to the field-free ionization temperature for an ice layer of zero thickness. Figure 6-1b illustrates the behavior of the ion signal during the field ramp. The ion current showed a

sharp onset field and a relatively narrow peak. The results of these earlier RFDs were very different from the field adsorbed experiments above 170 K outlined in Chapter 5. The onset field for ion emission was actually lower for lower temperatures in these field adsorbed experiments, in stark contrast to the extrapolated line shown in the low temperature graph. This contrast in behavior for the ramped field desorption of field adsorbed water at temperatures above 170 K and ice below 145 K suggests a difference in the limiting step for ion emission between the two cases.

6.1 Experimental Procedure

Two series of tests were conducted to characterize the mechanism of water ion cluster formation in a field adsorbed water layer on the platinum emitter tip. In the first, the Wien filter was used for mass selecting a particular water cluster ion signal for a series of isothermal ramped field ionization and desorption experiments. For the second, the Pt tip was directly imaged using water as the imaging gas at 180 K and 230 K for a variety of fields. An additional set of tests was carried out to examine surface charging effects during ion emission from low temperature ice layers by desorbing ion clusters from a thick ice layer through the cyclical application of stepped tip potential.

Prior to all testing, the Pt emitter tip was field-cleaned and imaged with neon gas. Cleaning was accomplished by field-evaporating a small amount of Pt from the surface, while visually inspecting the imaged surface until it appeared atomically clean and structured. Simple annealing of the tip was

not sufficient to remove all contaminants from the surfaces, especially carbon. Field-cleaning ensures complete removal of surface contaminants prior to testing and reduces the possibility of undesired surface reactions or interactions.

6.1.1 Low Temperature Mass Selected Ramped Field Desorption (RFD)

After imaging and field-cleaning, the tip potential V_t and counter electrode potential V_{CE} were each set to +3 kV. The cryo-cooled tip was then resistively heated to 145 K for water deposition. Water was deposited at a partial pressure of $2x10^{-7}$ Torr for 5 minutes, resulting in a deposition thickness of approximately 100 Å. Under these conditions, water is deposited as crystalline ice[31]. The tip was then heated or cooled to the desired temperature for the field desorption. The Wien filter was tuned to select a particular ion mass. To maintain a constant ion formation potential with respect to ground, the tip potential was held constant while the counter electrode potential was ramped from +3000 V to 0 V at a rate of 10 V/s to increase the local field. The constant ion formation potential is important for both lens focusing and consistent Wien filter results. A computer data acquisition system recorded the mass selected ion signal as a function of potential. After each ramped field desorption, the tip potential was taken to the field cleaning potential at 110 K to refresh the tip. The Wien filter was then tuned to a different mass, water was again adsorbed, and the ramping procedure was repeated. RFDs for each cluster type were performed for n up to 7 at both 109 K and 145 K.

6.1.2 Direct Ion Imaging

The Pt emitter tip was positioned at the MCP/phosphor screen for direct imaging of ion cluster formation on the tip surface. Prior to imaging with water, the tip was field-cleaned in neon. The tip potential was set to 3 kV and the counter electrode potential was set according to the desired ion cluster formation size as determined from previous experiments. Water was introduced to the chamber to a pressure of 5 x 10^{-6} Torr. This establishes a steady state ion signal, as opposed to the discrete ion signal of the RFDs. The ion signal from the Pt tip was amplified by the MCPs and the image on the phospor screen was recorded with a CCD camera. The CCD camera signal was acquired by the computer at a scan rate of 5 frames per second and resolution of 640 x 480 pixels. This procedure was repeated for a series of potentials at both 180 and 230 K.

6.1.3 Step Desorption Cycles

The preparation and deposition methods for these experiments were identical to those outlined in 6.1.1 with a few notable exceptions. Water ice was deposited at 145 K at a pressure of 5 x 10^{-7} Torr for 15 minutes to obtain a thick deposition layer ~ 750 Å. The tip was then cooled to 110 K for step desorption. The tip potential was constant at 3000 V, and the counter electrode was stepped between 1200 V and 900 V. At 1200 V, no ion signal was present. The 900 V potential was sufficient to provide a steady ion current without flashing the ice cap. These potentials were selected specifically for the tip conditions by previous experimental trials. The full ion

signal was recorded as a function of time by PC data acquisition. The potential was stepped to 900 V (high field condition) for 30 s and then back to 1200 V (low field condition) for a period of time ranging from 30 s to 270 s before repeating the step.

6.2 Results

Figure 6-2 depicts the results of the ramped field desorption experiments. The 109 K data in Figure 6-2a shows ion signal from all masses n = 2 to 7, with the dominant mass at n = 3. The ion emission signals occurred simultaneously (in a flash) at an applied field of 0.44 V/Å. For the higher temperature experiments at 145 K (Fig. 6-2b), the ion content was changed and the onset occurred at a lower field of 0.32 V/Å. This ramp showed only clusters n = 4 to 7. The dominant n = 3 peak observed in the 109 K system was absent at 145 K. Again, all clusters appeared simultaneously at the ionization onset in a flash for a given experiment. The slight onset deviation exhibited between the differing masses is due to the deviations from experiment to experiment.

Fig. 6-3 illustrates the spatial distribution of ion cluster formation under steady state tip conditions, time-averaged over 10 seconds, for a variety of potentials at 180 and 230 K. Intense white areas represent localized ion formation throughout the 10 second measurement period. The micrograph in Fig. 6-3a is the signal average for a tip field favoring large ion cluster formation (n > 4; F = 0.27 V/Å) at 180 K. Few ion sources were present, but those present persisted for all or most of the imaging time. In Fig. 6-3b (n = 4;

F = 0.34 V/Å), ion formation occurred from a larger number of sources with similar persistence of signal. Figure 6-3c shows conditions (n = 3; F = 0.45 V/Å) optimal for emission of n = 3 clusters. The size and number of localizations again increased. In Fig. 6-3d (n = 2; F = 0.64 V/Å), the number of sources increased further, but the intensity of each localization appears less. This trend is more pronounced for the transition from Fig. 6-3d to Fig. 6-3e (n = 1; F = 1.0 V/Å). In Fig. 6-3e, many small localizations remained for the course of the experiment. Additionally, in both Figs. 6-3d and 6-3e there are numerous localizations that did not persist throughout the experiment, which appear as gray spots. Figure 6-3f shows the tip at a field (H_2O^+; F = 1.6 V/Å) where field-ionization of the water molecules occurs directly, prior to dissociation on the surface. No sustained localizations are visible. Figs. 6-3g and 6-3h were recorded at 230 K for the same fields as Figs. 6-3d and 6-3e, respectively. The increased temperature increases the size of the localizations while decreasing their number. Finally, Fig. 6-3i is a picture of the platinum tip cleaned and imaged with neon after testing.

Figure 6-4 shows the results of the step desorption experiments. The step desorptions depicted are taken after a series of prior step desorptions followed by the discharge time τ as shown. For all step desorptions, the ion emission peaked immediately following the step and then quickly decayed to a relatively steady emission level. Step desorptions following short discharge times had lower initial emission peaks than those of the longer discharge times, but stabilized to the same level.

6.3 Discussion

6.3.1 Mass Selected Ramped Field Ionization and Desorption of Ice Layers

The emission mechanism outlined previously[96] provides an understanding of the behavior of the emission for the field-adsorbed system (i.e. at higher temperature), but does not explain the low temperature RFDs. At low temperatures adsorbed ice layers provide sufficient water coverage for large cluster emission, but fail to emit clusters until higher fields. It is also important to note that the apparent emission barrier determined by Scovell, et al. was ~0.7 eV, which is nearly equal to the activation energy for molecular dissociation of bulk water[87], suggesting that under their experimental conditions, ion emission was determined by the onset of dissociative ionization. While the dissociation event is strongly field dependent, it is much more strongly influenced by temperature than the emission barriers observed for the higher temperature work in the field adsorbed water layers. This is because the activation barrier for dissociation is significantly lower than the field free barrier for ion emission (~4 eV).

Based on the field-adsorbed ion emission results coupled with the low temperature RFD data, it appeared that dissociative ionization was rate limiting at low temperatures while cluster emission was rate limiting at higher temperatures in determining ion current. Therefore, another line of experiments was performed to test this hypothesis. The same ramped field desorption experiments performed by Pinkerton, Scovell, et al.[22, 86-88] at low temperatures were repeated at 109 K and 145 K, but with mass resolved ion analysis, as shown in Figure 6-2. The procedure for these experiments

was the same as that used for field adsorbed ramped field desorption with the exception of the dosing technique.

The behavior of these mass resolved low temperature RFDs supports the two-step hypothesis where dissociative ionization and ion emission occur as separate events. The same field dependent emission barriers observed in the high temperature work still hold at low temperatures for determining which cluster types are energetically accessible for emission. The difference is that at these low temperatures the field ramp passes through several emission barriers prior to reaching the dissociation barrier. This behavior can be illustrated by considering the three ramps shown in Figure 6-5. For this figure, the dissociation line is taken from ref.[87], while the cluster emission fields (horizontal lines) are taken from previous field adsorbed RFD experiments[96]. In RFD1 (109 K), the ramped field passes through the emission field for each cluster, beginning with the high masses and moving in turn through n = 2, immediately prior to intersecting the dissociation barrier. Upon reaching the dissociation field, ion emission begins in a flash containing all of the cluster types beneath the dissociation line. As observed with the ion population shown in Fig. 6-2a, all ion clusters n > 1 are energetically accessible when the dissociation event occurs. However, the n = 2 cluster is barely accessible so the primary cluster type remains n = 3. For RFD2 (145 K), the field passes through each cluster n = 4 and above prior to reaching the dissociation threshold. At the threshold, the ion clusters are again removed in a flash, but in this case n = 2 is not observed and only trace n = 3 ions are

present, as observed in Fig. 6-2b. Finally, for RFD3 (180 K), the field ramp passes through the dissociation barrier prior to any of the emission barriers, resulting in dissociative ionization on the tip surface without ion emission. Ion emission begins only after the ramp reaches the high mass cluster emission fields and then favors each cluster type in turn moving to smaller clusters at higher fields.

6.3.2 Direct Imaging of Water Ion Cluster Formation

To better understand the dynamics of the ion cluster formation, the full ion signal was imaged directly onto the MCPs at potentials corresponding to peak ion signals. The direct imaging of the ion formation in Figure 6-3 clearly shows that the ionization/emission events are strongly localized for dissociated ionization. The higher mass clusters have fewer active locations. As the field is increased, the dominant cluster size n decreases. With this decrease comes smaller and more numerous emission localities. Particular localities are temporary, but have extremely long lifetimes relative to the time scale of an ionization event. All pure white localities depicted lasted more than 10 seconds. Consequently, there must be a self-sustaining process that increases the probability of an emission event in an area where a previous event has occurred.

The results of these imaging experiments are consistent with a hump formation hypothesis. Ion emission occurs from localized points on the emitter surface for times that are epic relative to the timescale of an ionization event. A comparison of Figs. 6-3a-h with Fig. 6-3i does not suggest any

correlation between surface geometry and emission localization, although such a correlation would be reasonable. From micrograph to micrograph, the positions of the localizations change. They were also observed to change on a time scale of about 20 to 30 seconds. However, it is possible that the state of the platinum surface, as either a metal or oxide, affects the emission event in a manner that is not obvious from analyzing the field cleaned image.

An effect similar to hump formation and localization of ion current is observed in the formation of Taylor cones[97] for liquid metal ion sources where the balance of surface tension and electrostatic pressure results in self-sustained ion sources with substantially enhanced electric fields. However, the enhanced field near the hump in the adsorbed water layer not only eases ion emission, it increases the probability of dissociative ionization of additional water molecules near the hump. Consequently, the initial localization of charge results in a self-sustaining ionization and emission point. At low fields and temperatures, if the emission current is limited by the rate of dissociation, this enhancement would play an even more important role as both the supply of ions and the emission event are amplified.

6.3.3 The Importance of Solvation

Solvation of the proton (and hydroxyl) plays an important role in both dissociation of the water molecule and emission of the ion cluster. Fig. 6-6a shows an illustration of field induced ion dissociation in a thin water layer. The field is highest at the interfaces (Pt-water or water-vacuum) and is largely screened within the water layer[86]. However, dissociative ionization will not

readily occur at either interface due to the lack of solvating water molecules. The dissociative event needs other water molecules to screen the charge and allow for separation of the proton from the hydroxyl ion. The degree of screening determines the energy barrier height for the dissociation, as well as the energies of the dissociation products after dissociation. If the barrier is too high, reaction will not proceed. The suitability of the local environment for accepting the dissociation products near a potential event plays a significant role in the dissociation step. The key to this suitability is the solvation of the dissociation products. Therefore, since the ionization event cannot readily occur at either interface due to solvation limitations, it will occur immediately inside either interface, where solvation is sufficient and the field remains high. The field at these locations will be much lower than the applied field on the tip.

After dissociation, the hydroxyl ion will move to the tip and discharge as shown between in Figs. 6-6b and 6-6c. The proton will remain on the tip until the field is sufficient to emit the ion cluster. While it resides on the tip, the solvating water molecules will help to screen the proton charge. However, the proton still represents a charge localization on the surface. This localization will attract other water molecules on the surface (through dipolar attraction) and result in further solvation of the proton. Eventually there will be a balance between the solvation rate and the desorption rate of the least bound solvating water molecules. Our earlier work[96] has shown that the extent of

solvation due to this balance is temperature dependent and effectively determines the largest available cluster for ion emission.

6.3.4 Water Ion Cluster Field Emission Mechanism

The importance of the proton solvation shell continues through the emission event. Figs. 6-6b and 6-6c illustrate an idealized ion emission event. The ion emission event will not occur by simultaneously breaking all of the bonds with the surface. As the ion cluster pulls away, nearby water molecules are pulled towards the localized charge, forming a hump as the ion is emitted. The remaining water molecules are left in a state highly conducive to further dissociation events. First of all, there is a high local concentration of water providing an environment for proton/hydroxyl solvation. As the emission event occurs, the surface adsorbed water is pulled away from the tip resulting in a higher local thickness of the adlayer. This thicker layer provides an opportunity for 3 dimensional solvation, allowing for the dissociation event to occur *beneath* the surface of the water layer, as described above. Secondly, this hump formation leads to a high degree of local surface curvature. As a result, the field at the hump is enhanced. This may be compounded by the fact that the remaining local water molecules had adjusted their orientations to screen the charge of the nearby proton, resulting in a charge "vacancy" after the ion emission event has occurred.

6.3.5 Notes on Low Temperature Cluster Formation

The picture presented of the two step mechanism so far has focused on the dissociation and emission events, without consideration of transport

phenomena. In the field-adsorbed water layer experiments, there is a high incident flux and low residence time of water on the surface, and surface diffusion occurs relatively freely, allowing transport to be largely neglected. However, for the ice deposition RFD experiments, the solvation, cluster formation and emission events are complicated by transport limitations. The onset of surface diffusion or glass transition near 130 K may be responsible for the slope break in emission onset observed by Scovell, et al.[87] (Figure 6-1a). This mobility would provide a greater capacity for solvating the proton during dissociation near the surface (where the field is strongest). Near 150 K, molecular transport within bulk ice becomes possible, which may further facilitate dissociation; however RFD experiments at this temperature have not been carried out. The limitation of transport of water molecules is not the only significant consequence of the low temperature. Hydroxyl diffusion through the ice layer to discharge at the tip surface may also be transport limited. If the hydroxyl discharge cannot occur quickly, there will be a negative charge buildup near the water surface, effectively screening the tip field and shutting down emission. This hypothesis is supported by the results of the stepped field desorption experiments shown in Fig 6-4. When the potential was stepped, the ion signal spiked and then quickly decayed to a stable emission level. Temporarily reducing the potential to a level below the emission threshold and then re-stepping the potential resulted in another emission spike and decay to the same level. The intensity of the initial peak depended upon the length of time between emissions.

During the interim time period, a field is still applied to the tip, but the field is insufficient for emission. At experimental temperatures, dissociation is the limiting step for emission, so it is unlikely that the emission enhancement resulting from extending τ is due simply to the buildup of protons in the ice layer. However, each dissociation reaction near the surface of the ice layer during emission produces a corresponding hydroxyl ion. In field adsorbed water layers (high temperatures), the negative charge will quickly discharge on the tip surface, but for the thick ice layer, the charge will require more time to discharge as either the hydroxyl or the electron itself makes its way to the tip surface. The presence of these negative charges in the ice layer acts to screen the field at the ice surface limiting the emission. For a given set of tip conditions, an equilibrium emission rate is quickly established where the ion emission and hydroxyl (electron) discharge are in balance. By shutting off emission while maintaining a field (as is the case when the field is stepped down), the ice layer continues to discharge without building up additional charge. This effect results in the observed increase in ion signal at the beginning of the potential step.

6.4 Conclusions

The emission of ions from a field emitter tip has traditionally been thought of as a single event process where the ionization and emission were assumed to occur nearly simultaneously. Our research into the field induced ion emission of protonated water clusters from both deposited ice layers and field adsorbed water layers suggests otherwise. The evidence supports a two-

step mechanism requiring first the dissociation of an adsorbed molecule followed later by ion emission. The energy barriers for these steps are very different and are influenced differently by the applied field. The situation is further complicated by the temperature dependence of solvation of the proton on the surface and the availability of solvating water molecules.

Based on the results of the field adsorbed water ionization and ice deposition RFDs, two independent steps are required for water ion cluster emission. The first step, water dissociation, is a field-enhanced, thermally activated process with an activation energy of ~0.7 eV. The extent of solvation of the product ion pair (H^+ ... OH^-) is important to the success of the dissociation event. After the water molecule dissociates, the OH^- discharges on the tip and the proton remains in an intermediate state on the surface, solvated by nearby water molecules. These solvating water molecules are bound to the proton by their solvation energies. The extent of solvation depends on the tip temperature, as desorption of the solvating molecules is thermally activated, requiring more energy with decreasing *n*. The extent of solvation determines the minimum field required for the second step, ion emission. If the field is sufficient, ion emission occurs. The emission event acts to facilitate additional dissociation events locally and an emission localization occurs.

(a)

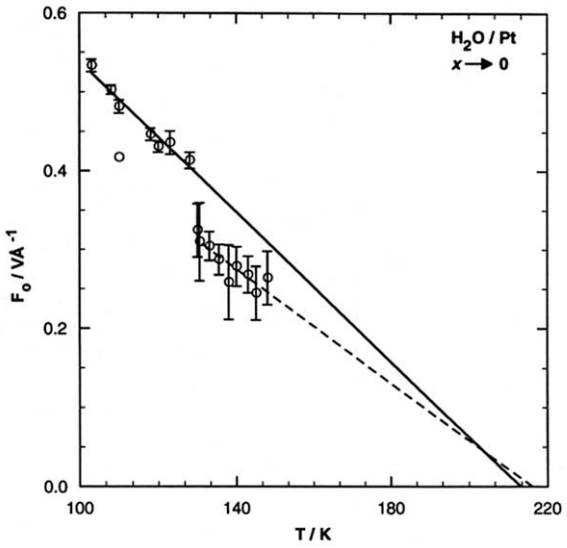

(b)

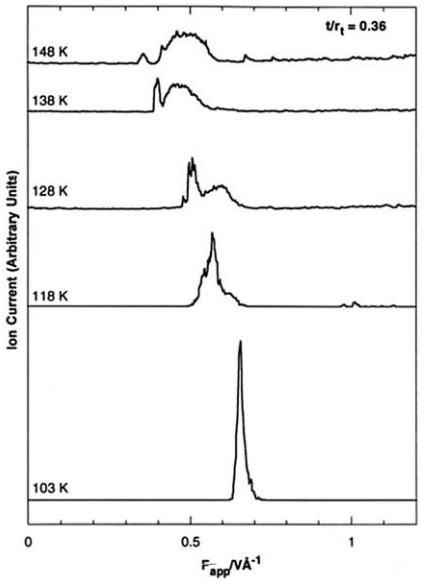

FIGURE 6-1: Previous protonated water cluster emission results. (a) Applied field F_A for ion emission onset as a function of temperature T in the limit of zero coverage for water deposited on a Pt emitter tip. Reprinted from Scovell, et al. (b) Ramped field desorption total ion current for adsorbed water (ice) layers. Dimensionless ice thickness (thickness water / tip radius) was 0.35. Reprinted from Scovell, et al.

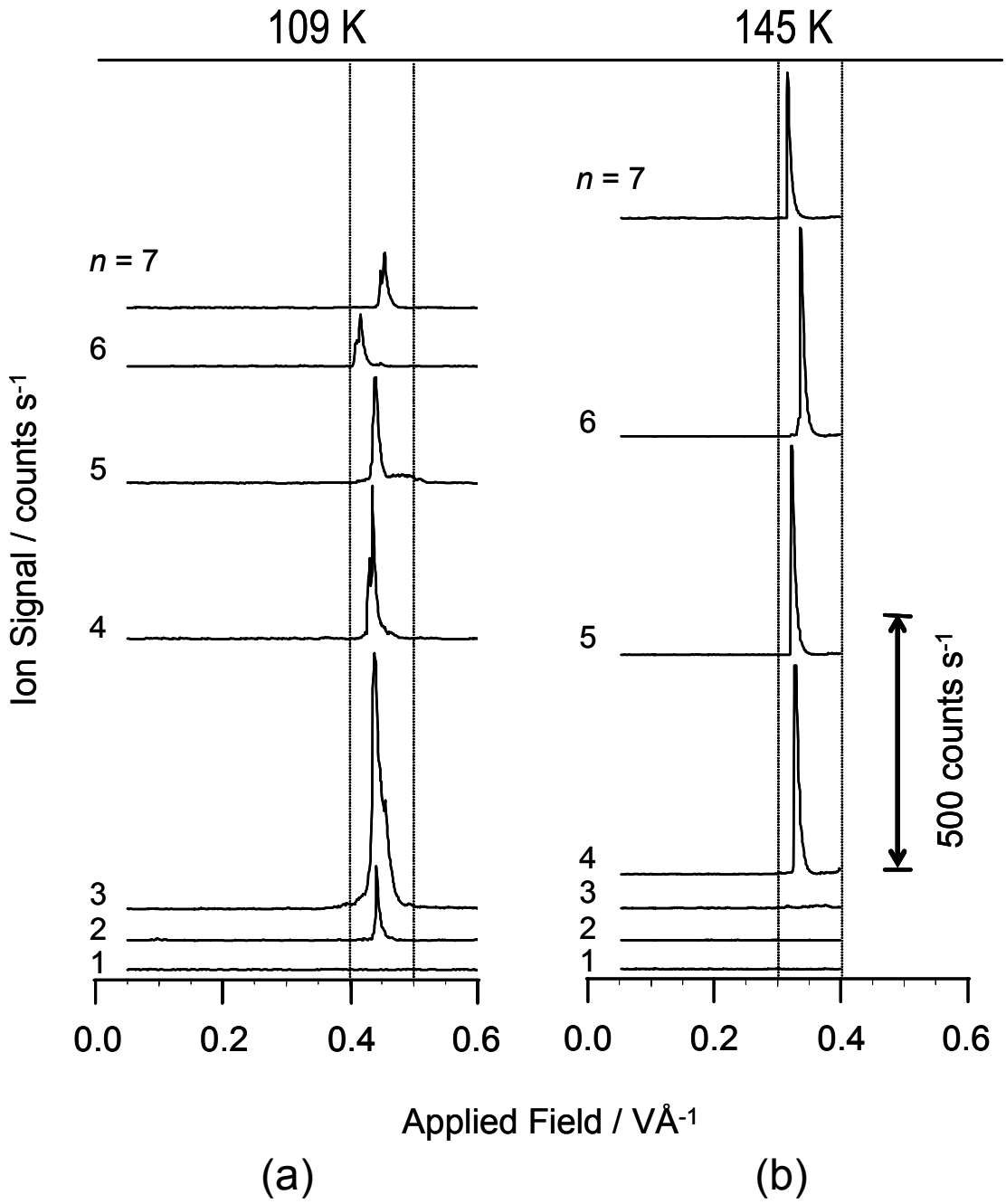

FIGURE 6-2: Mass selected ramped field desorption (RFD) of ice layers from a Pt field emitter tip of radius ~350 Å. Crystalline ice was deposited at 145 K to a thickness of 100 Å. Protonated water clusters $H^+(H_2O)_n$ are shown for *n* up to 7. (a) Tip cooled to 109 K for RFD. (b) Tip at 145 K for RFD.

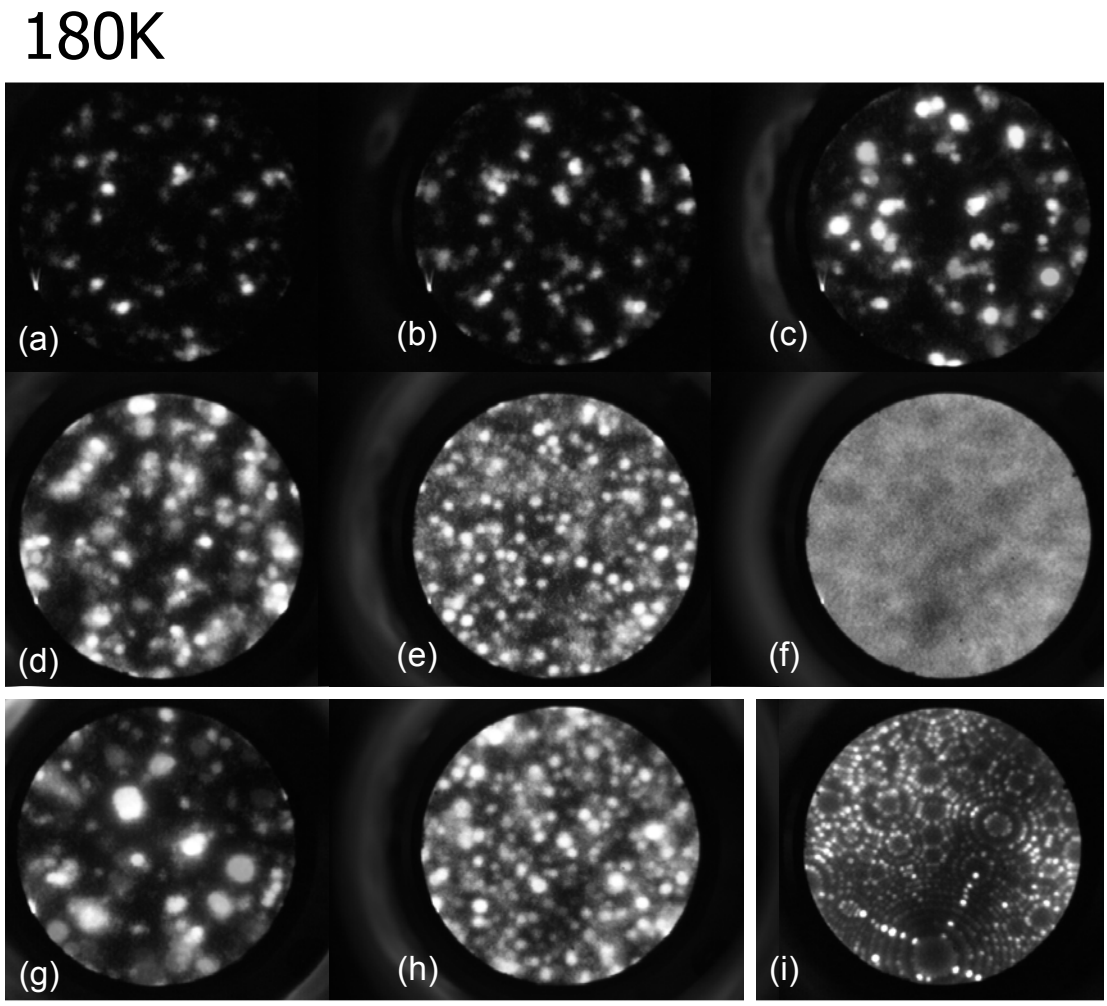

FIGURE 6-3: Field ion micrographs of protonated water cluster $H^+(H_2O)_n$ emission at 180 K and 230 K for a variety of fields selected for favoring particular clusters types. Imaging is water only for a-h, and neon only for i. Micrographs represent 10 seconds of signal averaged ion intensity. (a) Clusters $n > 4$; $F = 0.27$ V/Å; $T = 180$ K. (b) Cluster $n = 4$; $F = 0.34$ V/Å; $T = 180$ K. (c) Cluster $n = 3$; $F = 0.45$ V/Å; $T = 180$ K. (d) Cluster $n = 2$; $F = 0.64$ V/Å; $T = 180$ K. (e) Cluster $n = 1$; $F = 1.0$ V/Å; $T = 180$ K. (f) H_2O^+; $F = 1.6$ V/Å; $T = 180$ K. (g) Cluster $n = 2$; $F = 0.64$ V/Å; $T = 230$ K. (h) Cluster $n = 1$; $F = 1.0$ V/Å; $T = 230$ K. (i) Field ion micrograph of clean Pt tip in Ne at 3.75 V/Å provided for reference.

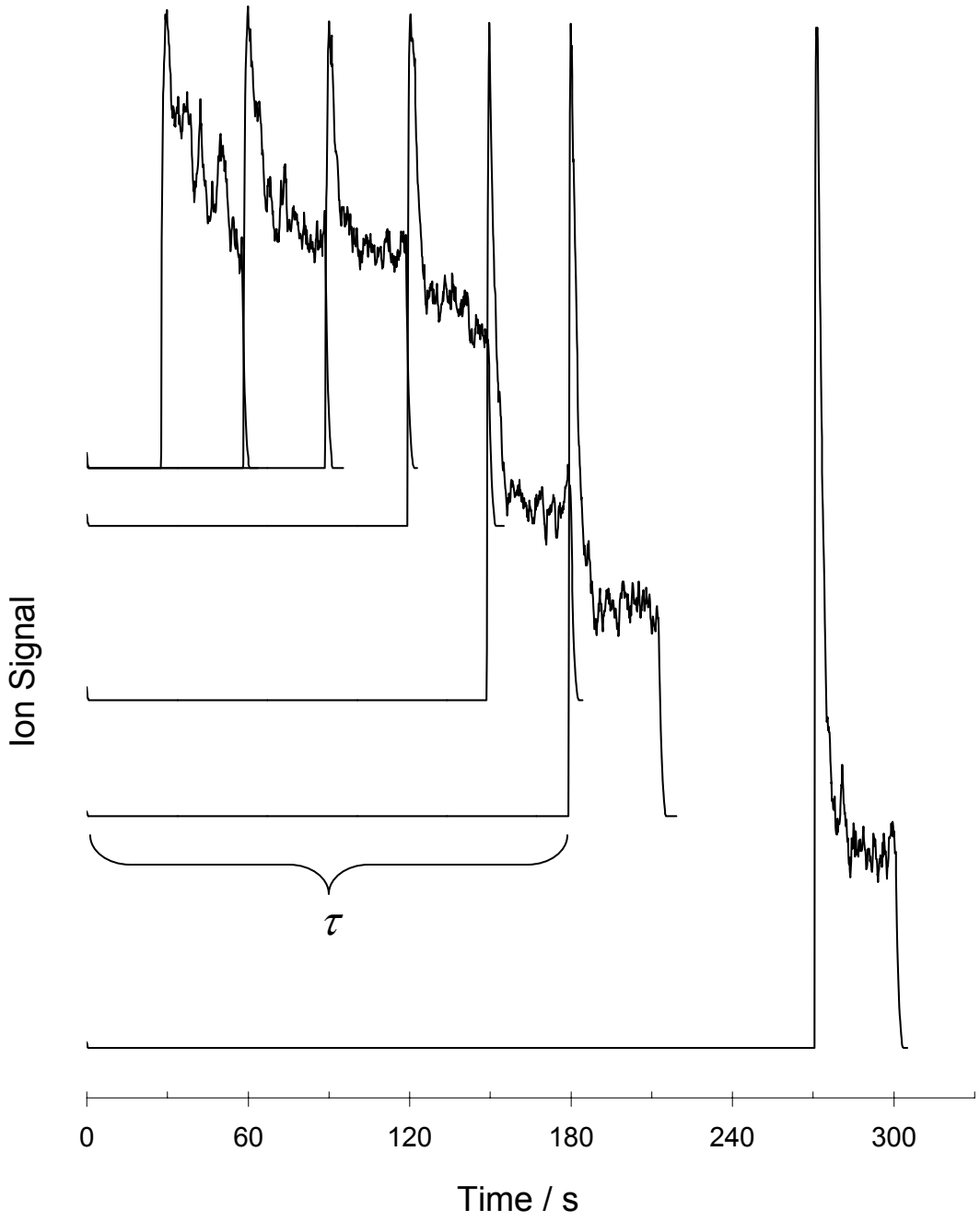

FIGURE 6-4: Step desorption of water clusters from thick ice layers on Pt tip. Ice deposition thickness ~ 750 Å at 145 K. Tip potential set to 3000 V. Counter electrode stepped from 1200 V to 900 V at t = τ.

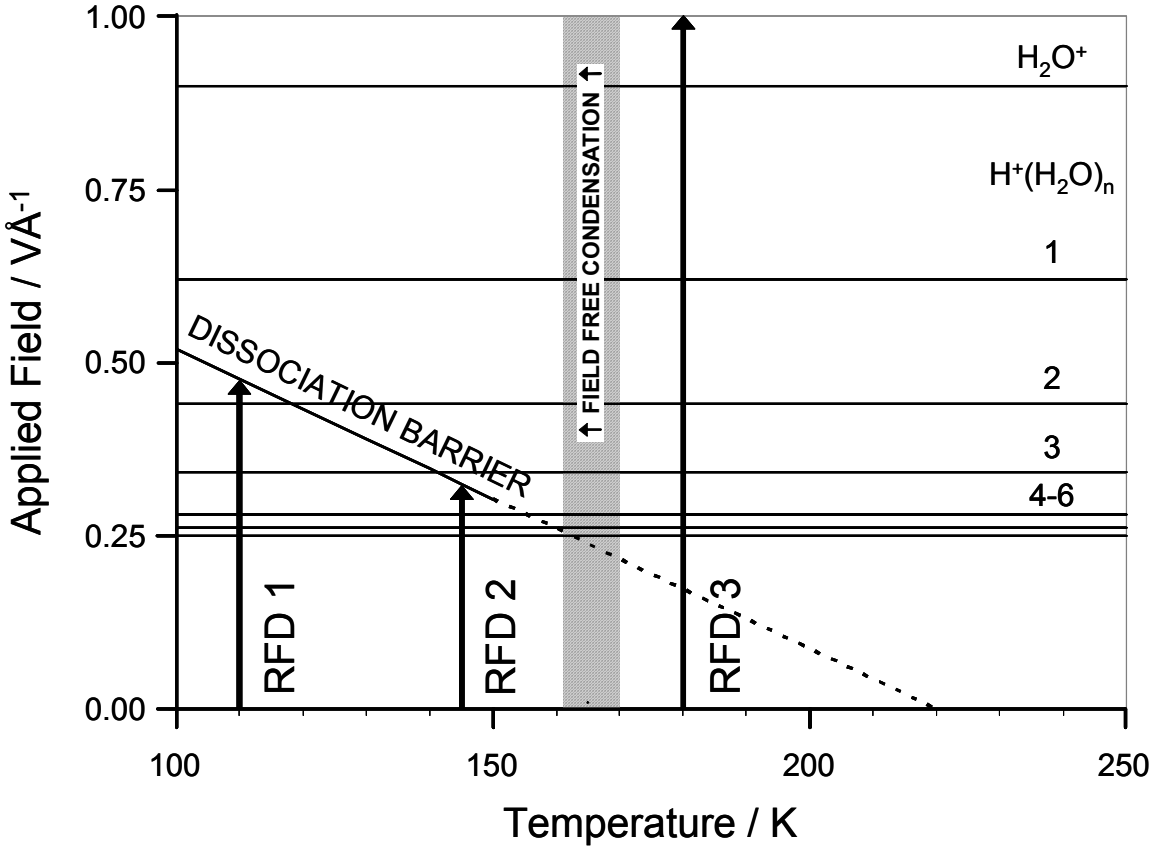

FIGURE 6-5: A comparison of three ramped field desorptions. RFD1 is at 109 K and passes through the emission barriers for all clusters 2 and above and then reaches the dissociation barrier. RFD2 is at 145K and passes through emission barriers for clusters above 3 before reaching the dissociation barrier. RFD3 is above the field free condensation zone. It passes through the dissociation barrier prior to reaching any of the emission barriers. The emission barriers are taken from Chapter 5. The dissociation barrier is taken from Scovell et al.

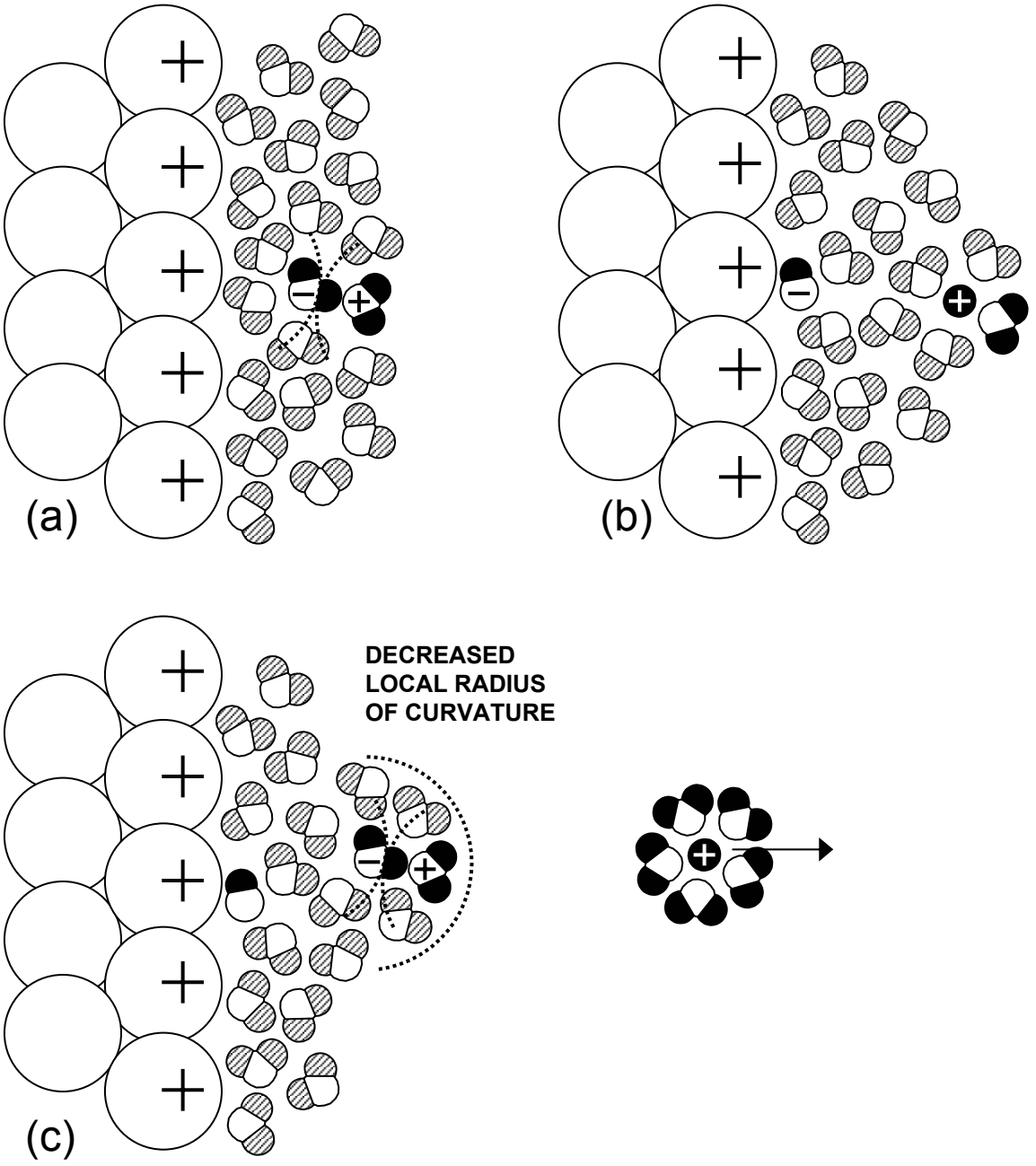

FIGURE 6-6: Idealized model of 2 step ionization / emission mechanism. (a) Water molecule in field begins to dissociate. Dissociation probability is influenced by the alignment of molecules and the extent of local solvation for accepting. (b) After dissociation, the hydroxyl moves to the tip surface to discharge and the solvated proton moves to the vacuum interface for emission if the field is strong enough. (c) After emission, a localization is created with a decreased local radius of curvature. This localization provides a higher local probability of dissociation due to field enhancement.

CHAPTER 7: FIELD EMISSION OF METHANOL AND WATER / METHANOL MIXTURES

The investigation of ion cluster formation and emission from a Pt emitter tip has been expanded to water / methanol mixtures. The water / methanol system and its behavior in high fields are of particular interest to direct methanol fuel cell research. In a DMFC, the well hydrated methanol molecule adsorbs on the platinum surface where it undergoes dehydrogenation, generating protons. The proton charge must then be screened by a solvation shell of water molecules (typically ~ 4 water molecules)[64, 108]. The methanol molecule itself brings a water solvation shell of around 3 molecules[109]. Under steady state conditions, there are 6 presumably well solvated protons leaving the surface for every methanol molecule arriving (assuming complete dehydrogenation). Consequently, the fluxes of solvating water molecules chaperoning the inbound methanol and outbound protons are significant and will play an important role in the actual kinetics of the surface reactions. Extending the water ion behavior to include methanol has provided some insight into the solvation and dissociation behavior of this complicated system.

The spectra of ions observed for methanol and water / methanol mixtures are much richer than those for the pure water system. Two sets of experiments have been performed to determine the ion cluster types emitted

from a field adsorbed layer of methanol and water / methanol mixtures. The first was a low field Wien filter series to qualitatively illustrate the clustering behavior. The second series used pulsed ToF spectrometry to determine the ion masses present in ion streams at different potentials.

7.1 Experimental Procedure

A preliminary analysis of ionization and emission characteristics for methanol and water / methanol mixtures was performed using the Wien filter at low magnetic fields to simultaneously image all cluster masses. The drift tube attached to the Wien filter was removed, shortening the ion flight path, and allowing for easier focusing of the ion beam. The Pt emitter tip was imaged and field cleaned with neon prior to testing. The tip radius based on the best imaging potential was 370 Å. The tip temperature was set to 180 K for all experiments. Three different series of tests were performed. The first series was with pure water at a partial pressure of $4x10^{-6}$ Torr. The second was with pure methanol (MeOH) at $4x10^{-6}$ Torr. The third was with a mixture of water and MeOH, each with partial pressures of $2x10^{-6}$ Torr.

Testing was performed in continuous mode with ion emission occurring from a field adsorbed layer similar to the previous 180 K water research described in Chapter 5. Tip potential was set at +3000 V, and the counter electrode potential was varied to apply the desired field. Ion spectra at different fields up to 1.10 V/Å were recorded for each composition. Ion spectra were obtained by recording ion signal images to PC using a CCD

camera with video acquisition. Each spectrum represents 300 linearly averaged frames of recorded ion signal.

For the ToF experiments, the Pt tip was cleaned and imaged and then set to a temperature of 165 K. A +3000 V potential was applied to the tip, and the counter electrode was set at +2600 V. A digital delay generator triggered the pulser, which delivered square pulses of negative potential to the counter electrode resulting in an increase in the applied field on the tip. Two series of tests were performed. The first series investigated the characteristics of ion emission from pure methanol on the tip at $6x10^{-6}$ Torr for a variety of different fields. Pulse heights ranged from 300 V to 900 V. In the second, the pulse height was maintained at 600 V, while the composition of the field adsorbed layer was varied. The partial pressures of water and methanol totaled $5x10^{-6}$ Torr for each experiment, with the methanol/water ratio varying from 4:1 to 0:5. It is important to note that the experimental ratios are of partial pressures. Due to dipole and polarization differences between water and methanol, the actual partial pressures near the surface will be somewhat different.

7.2 Results

Figure 7-1 illustrates the Wien filter spectra for water, methanol and water / methanol ion cluster $H^+(CH_3OH)_m(H_2O)_n$ emission for a variety of fields. The water only spectra (Fig 7-1a) are consistent with previously reported results, showing cluster separation with cluster type dependent upon field. The methanol-only results (Fig. 7-1b) exhibit similar characteristics, with

cluster formation occurring for *m* up to 4, again with large mass clusters favored at low fields. The actual masses of the clusters shown are not easily determined from these Wien filter results. Additionally, fine structure appears to exist surrounding each cluster type, but cannot be discerned from this data. The third group of spectra (Fig. 7-1c) is for the water / methanol mixture. For this series, the lowest field spectrum was recorded at 0.39 V/Å, as opposed to 0.33 V/Å as in Figs. 7-1a and b.

Figure 7-2 shows the voltage dependent cluster formation for pure methanol. The peak heights have been normalized to emphasize peak position by pulse voltage. Actual ionization rates were much higher for higher potentials pulses. Peak position was calibrated to align the 33 peaks exactly, because the energy from the pulse resulted in slightly different initial potential energies. Low pulse potentials favored larger masses, as expected based on water cluster ion formation results. The primary peak for 300 V pulsing is located at mass 97. Additional peaks are present at 33, 65, and 129. Smaller peaks are observed at 83 and 115.

As the pulse potential was increased, ion cluster mass to charge decreased. Mass 65 became dominant at 400, and then faded away with greater pulse heights as the 33 peak group became dominant.

The results of the composition dependence analysis are shown in Figure 7-3. The top and bottom spectra are for pure methanol and water, respectively. Water ion clusters $H^+(H_2O)_n$ were present for *n* up to 6. The addition of methanol changed the spectrum markedly. In addition to the

presence of characteristic methanol peaks seen in the pure methanol spectrum only work, peaks at 51, 69, 83 and 87 were present in the mixed spectra.

Figure 7-4 is a closer look at the mass spectra near mass 33 for pure methanol and for the 4:1 methanol / water mixture. Primary peaks are located at masses 32 and 33, with secondary peaks at 30, 31 and 35. Peaks 32 and 33 are separated by ~100 data bins, with a maximum peak height of 1600 ions. Figure 7-5 is a further resolution of the pure methanol peak to show the fine structure near mass 35.

7.3 Discussion

The behavior of the ion cluster emission from the methanol and mixed water / methanol systems is qualitatively similar to what was observed in the water only systems discussed in Chapters 5 and 6. Below a threshold emission field, no ions were observed. As the field was increased, the dominant emitted ion species transitioned from large clusters to smaller clusters as previously demonstrated. However, there were a few interesting observed phenomena that did not necessarily follow from the pure water results. These include the richness of substructure in the methanol peaks, particularly around the m = 1 cluster; the composition and pulse dependence of the observed mass 32 / 33 ratio; and the enhanced presence of mass 19 for mixed systems.

7.3.1 Ion Cluster Emission Behavior

The results in Figures 1 through 3 suggest that the behavior of pure methanol on the Pt surface is similar to the previous water experiments, but are complicated by a number of factors. First of all, the adsorption energy of methanol on the surface is significantly higher than the latent heat of vaporization of pure methanol. The adsorption energy E_{ads} of methanol on clean Pt (111) is 0.49 eV[98, 99], whereas the latent heat of vaporization λ_v is only 0.36 eV. Compare this with water where the adsorption energy on Pt (111) of 0.44 eV[98] is nearly equal to the latent heat of vaporization of 0.42 eV [100]. This difference in energies may affect the solvation behavior of methanol on the surface since methanol is more strongly bound to the surface than to the other methanol molecules. In addition, the difference may serve to prohibit large methanol clusters because the additional solvation energy provided by the methanol in the larger clusters is less than the adsorption energy.

A thermodynamic cycle, similar to the one employed in Chapter 5 can be used to estimate and compare emission barriers for pure methanol on the surface. A proton near the methanol surface may be created by first removing a methanol molecule from the surface by providing the desorption energy E_{ads} of 0.49 eV,

$$^{\ell}CH_3OH \rightarrow {}^{v}CH_3OH\,. \qquad (7.1)$$

Dissociating a proton (or methyl group) is now more complicated, because of the R-H bond energy difference between H-CH_2OH and CH_3O-H which are 4.10

eV and 4.51 eV, respectively. Additionally, it may be possible to field dissociate the hydroxyl group from the methyl group CH_3-OH with a dissociation energy of 3.98 eV. Furthermore, dehydrogenation of methanol on the Pt surface will lead to additional intermediate products that may provide ions. For demonstrative purposes, the methoxy-proton pair will be chosen. Dissociating in vacuum with a dissociation energy E_D of 4.51 eV gives,

$$^{v}CH_3OH \rightarrow {}^{v}CH_3O + {}^{v}H \tag{7.2}$$

ionizing the hydrogen with an ionization potential I_P of 13.6 eV [28],

$$^{v}CH_3O + {}^{v}H \rightarrow {}^{v}H^{+} + {}^{v}CH_3O + e^{-} \tag{7.3}$$

transferring the free electron to the methoxy with an electron affinity E_A of -1.57 eV (here given as negative for consistency)[56],

$$^{v}CH_3O + {}^{v}H \rightarrow {}^{v}H^{+} + {}^{v}CH_3O^{-} \tag{7.4}$$

and then solvating the methoxyl ion with a solvation energy of $E_{s,CH3O-}$.

$$^{v}CH_3O + {}^{v}H \rightarrow {}^{v}H^{+} + {}^{\ell}CH_3O^{-} \tag{7.5}$$

A literature value for the methoxyl ion solvation in bulk methanol is not available. However, the solvation energy due to 4 solvating methanol molecules has been experimentally determined to be 2.84 eV[57] and more closely resembles the actual tip conditions. Summing the energies

$$\Delta E_{emit}^{H+} = E_{ads} + E_D + I_P + E_A + E_{s,CH3O-} \tag{7.6}$$

results in a total energy ΔE_{emit}^{H+} of 14.19 eV for the emission of a proton from bulk methanol. Energies for ion clusters of different *m* may then be calculated by accounting for the additional energy of solvation [57] of the emitted proton

by the m methanol molecules, minus the energy required to remove the methanol molecules from the surface according to,

$$\Delta E_{emit}^{m} = \Delta E_{emit}^{m-1} + \Delta E_{s,MeOH}^{m} + E_{ads} \qquad (7.8)$$

where ΔE_{emit}^{m} is the energy barrier for cluster m emission and $\Delta E_{s,MeOH}^{m}$ is the solvation energy due to the mth solvating methanol molecule. The calculated emission barriers for the first seven clusters are given in Table 7-1.

The pulsed ToF results for neat methanol at a variety of pulse potentials V_P shown in Fig. 7-2 are consistent with the calculated barrier energies. Low energy pulses favored large clusters. Increasing the pulse height allowed smaller cluster emission, which was then favored due to entropic considerations.

Estimating the emission barrier for mixed water / methanol is more complicated. Not only is the extent of surface solvation of the proton important, but the number and type of molecules in the cluster on the surface. Emitting a $H^+(CH_3OH)_m(H_2O)_n$ cluster from the surface requires

$$\Delta E_{emit}^{m,n} = \Delta E_{emit}^{H+} + \sum_{i=1}^{m} \Delta E_{s,MeOH}^{i} + mE_{ads}^{MeOH} + \sum_{j=1}^{n} \Delta E_{s,H2O}^{j} + nE_{ads}^{H2O}. \qquad (7.9)$$

The only term on the RHS that provides difficulty is the first term, the proton emission. If we define the excess emission energy $X^{m,n}$ for an ion cluster to be

$$X^{m,n} \equiv \Delta E_{emit}^{m,n} - \Delta E_{emit}^{H+} \qquad (7.10)$$

and substitute Eq. 7.10 into Eq. 7.9 giving,

$$X^{m,n} = \sum_{i}^{m} \Delta E_{s,MeOH}^{i} + mE_{ads}^{MeOH} + \sum_{j}^{n} \Delta E_{s,H2O}^{j} + nE_{ads}^{H2O}. \qquad (7.11)$$

then we can compare these relative emission energies for an arbitrary surface configuration without knowing the actual proton emission energy. Table 7-2 provides excess emission energies for several cluster types calculated using Eq. 7.11 and experimental solvation data from Meot-Ner[57]. More negative numbers represent lower emission barriers.

The Wien filter spectra in Fig. 7-1b follow the behavior suggested by Table 7-2. At the lowest field (0.33 V/Å), only emission of clusters m = 3 and 4 are observed. The field provides insufficient energy to emit m = 2 ions. Larger m clusters provide relatively little additional solvation energy and may either be discouraged by entropic effects or unavailable due to thermal desorption of the mth solvating methanol molecule. Moving to higher fields overcomes the energy barriers for the smaller clusters making them favored for emission.

The mixed water / methanol spectra are not clearly explained by the tabulated results in Table 7-2. The first ion cluster appearance was at a field of 0.39 V/Å. No ions were visible at 0.33 V/Å. However, the expected trend of shifting to lower mass clusters at higher fields was again observed. The reasoning behind the excess emission energy calculation still applies to the mixed cluster case; however, it appears that either the ΔE_{emit}^{H+} for the mixed system is higher for the mixed system than for either neat system, or that the dissociation barrier requires a higher field. Either way, it appears to suggest a lower degree of surface solvation of the proton in the mixed system than in either neat system.

Mixed clusters are clearly evident in Fig. 7-3. Neat water and methanol spectra are shown on the bottom and top of the figure, respectively. Under experimental conditions for the water only system, trace amounts of n = 1 are present with dominant peaks at 2 and 3 and visible peaks at 4 through 6. The methanol only system is dominant for m = 1 and 2. A comparison of the emission barrier energies shown in Tables 7-1 and 5-1 with the spectra in Fig. 7-3 suggests an inconsistency with the tabulated data. The presence of small amounts of n = 1 implies a field energy near the 5.77 eV emission barrier, but not much higher, according to Table 5-1. For the same field energy, Table 7-1 suggests that the methanol system should be emitting m = 3 and higher, in stark contrast to the observed clustering. This is likely due to inaccuracies in determining the actual solvation energies for the dissociated proton on the surface, which is clearly not fully solvated as the calculations assume.

Mixed (m, n) clusters of (1, 1), (1, 2), (2, 1) and (1, 3) were observed. While larger mixed clusters are energetically permissible (and often favored) the thin surface coverage does not appear to favor their emission. However, pulsed experiments tend to favor smaller cluster sizes because of their kinetic favorability.

7.3.2 Mass 19 Enhancement

One interesting phenomenon that is apparent from Figs. 7-1 and 7-3 is the enhanced presence of mass 19 emission for mixed systems. The H_3O^+ ion is barely visible in the pure water spectra and not present in the neat

methanol spectra. However in all of the mixed system spectra it is a dominant peak.

The most obvious explanation for the presence of the H_3O^+ ion peak in the mixed cluster series is that the mixed system results in a reduced emission barrier for the ions. If this explanation is correct, the thermodynamic emission cycle analysis (above) suggests that the mixed system would have to have a significantly lower proton emission barrier ΔE_{emit}^{H+} as a basis, consequently shifting all of the emission thresholds lower. As a result all of the peaks should have their behaviors shifted to resemble higher fields conditions. High mass peaks should diminish accordingly. This appears to be the case in Figure 7-3, although it is difficult to conclude because of the increased ion contribution due to mixed mass clusters.

A second possible explanation is that the H_3O^+ ions are daughter ions[73, 74] formed during flight. The height of the peak appears to correlate well with the peak for the mixed (1, 1) cluster. If a fraction of the emitted (1, 1) clusters breaks apart during flight, it would provide a source for H_3O^+ ions that would be unavailable in the neat systems. However, this break would require ~ 1.8 eV[57] with no apparent energy source.

7.3.3 Ion Mass Substructure

The ion mass spectra near the m = 1 peak is much richer in character than a simple variation on the mass 33 peak. Figure 7-4 shows the peak substructure near the mass 33 peak for pure methanol and the 4:1 methanol to water experiments. Distinct peaks are present at M/z = 30, 31, 32, 33 and

35. For the mixed cluster system a small peak at M/z = 37 is also visible representing the $H^+(H_2O)_2$ ion clusters. Additionally, a very small peak is visible at M/z = 15 in Fig. 7-3. Similar peaks can be observed in ToF spectra performed by other research groups[71, 72, 101], but very little discussion about the nature of these peaks is provided, with the focus resting on the primary 33 peak.

Table 7-3 lists possible molecular configurations for ion masses near M/z = 33. The actual configuration of the peak cannot be determined from the ToF data alone. Additional experiments, such as deuterium doping, would provide further insight into the exact nature of the ions. Shi, et al.[72] reported observing mass 29 (CHO^+) and 31 (CH_3O^+) in addition to the 33 peak, in a ToF study of vacuum ultraviolet ionized methanol from a jet expansion, but did not observe 30, 32 or 35. This suggests that these masses are the result of secondary combinations of previous reaction products remaining on the surface. The mass 35 ions are particularly curious. The only viable molecule of that mass is a protonated peroxide molecule $H^+(HOOH)$.

An additional consideration is the possibility of doubly ionized molecules. The most convincing evidence for this is the apparent peak at 32.5 in Fig. 7-4, which would correspond to an $[H^+(CH_3OH)_2]^+$ molecule. The second ionization may occur either as a field ionization during emission (electron tunneling) or as emission of doubly protonated cluster. The doubly protonated clusters would be highly unstable, and would very likely fracture in the flight tube resulting in daughter ions (that may help to explain the other ion

masses). However, at the field strengths present in these experiments, the formation of doubly charged methanol ions seems intuitively unlikely.

Another interesting characteristic apparent from Fig. 7-4 is the additional substructure within each of the mass peaks. A further magnification of the ToF spectrum near mass 35 is shown in Fig. 7-5. The spectrum is divided into subpeaks with a wavelength of 0.239 ± 0.017 M/z or a time of flight of ~ 29 ns. The data points and actual experimental ion counts are displayed to illustrate that it is not simply a signal to noise issue. Peaks and valleys are separated by >200 ion counts in some cases.

The energy deficit necessary to produce an apparent mass to charge shift may be calculated by first taking the simple time of flight equation

$$\frac{M}{z} = \frac{2eV_0}{L_D{}^2} t^2 \quad , \tag{7.12}$$

taking the derivative with respect to a change in potential energy

$$\frac{d(M/z)}{dV_0} = \frac{2e}{L_D{}^2} t^2 , \tag{7.13}$$

and then substituting Eq. 7.13 into Eq. 7.12 giving

$$\frac{M}{z} = \frac{d(M/z)}{dV_0} V_0 . \tag{7.14}$$

Multiplying both sides of Eq. 14 by *z* and rearranging provides,

$$\frac{\Delta V_0}{V_0} = \frac{\Delta M}{M} . \tag{7.15}$$

So for M at 35, V_0 of 3000 and ΔM of 0.239, the deviation in initial energy would be ~20 eV for a singly charged ion. This energy deficit is far too great to

be explained by subtle emission or ionization differences, as it is over twice the emission energy of a typical ion cluster. However, for a sufficiently thick adlayer, the ionization may occur at a sufficient distance from the emitter to result in a significant energy deficit as observed.

A more probable explanation would be ringing of the pulsed counter electrode due to insufficient termination and impedence matching. With the pulse width around 70 ns, and the counter electrode pulse height at 600V for these experiments, pulse ringing with a frequency around 29 ns and a maximum amplitude ~100 V is not unreasonable.

7.3.3 Mass 32 / 33 Ratio

The final notable feature in the mass spectra for the methanol and mixed water / methanol systems is the shift in the mass 32 / 33 ratio. Fig. 7-2 shows that with increasing pulse height, the 32 to 33 ratio increases. This supports the idea that the mass 32 ions are field ionized methanol molecules. Field ionization is energetically unfavorable in comparison with field emission of a protonated methanol clusters (mass 33), but is mechanistically simpler. As the field increases due to the higher potential pulses, more methanol is directly ionized either on the surface or in the vacuum near the surface. The integrated peaks and corresponding peak ratios are tabulated in Table 7-4. At low potentials, very few ions of mass 32 and 33 were observed, but those present strongly favored the protonated cluster with only a 0.12 to 1 ratio. Increasing the potential increased the ratio, and at a pulse height of 900 V, mass 32 was favored 1.62 to 1.

A similar trend is present in Fig. 7-2. The 32 to 33 ratio visibly increases with decreased methanol to water ratio. Since the pulse height is uniform in these experiments, the direct ionization rate of methanol on and near the surface should be relatively constant for each system. Therefore, the change in ion ratio is due to diminished mass 33 emission relative to a constant mass 32 emission due to suppression of the peak by the presence of the water molecules. Table 7-5 shows the mass ratios by water / methanol compositions.

7.4 Conclusions

The results of the methanol and mixed water / methanol systems are consistent with expected results based on an extension of the two step dissociation and emission mechanism advanced for the water only system. Protonated methanol clusters were observed using pulsed time of flight mass spectrometry in the neat methanol system for *m* up to 4. Large clusters were favorable at low fields (counter electrode pulse heights), while higher fields provided the necessary energy for the emission of low mass clusters. Complex spectra were observed near the *m* = 1 cluster. In addition to the primary peaks at mass 32 and 33, secondary peaks at 30, 31 and 35 were observed. The exact nature of these secondary peaks was not determined. The ratio of the 33 to 32 peaks decreases with increasing field.

The addition of water to the methanol system behaved largely as expected, with the presence of mixed $H^+(CH_3OH)_m(H_2O)_n$ clusters present along with the previously observed neat clusters. However, there were two notable

effects observed for the mixed systems. First, the mass 19 signal intensity was enhanced in the mixed system, despite being absent from the neat methanol tests and nearly absent from the pure water system under comparable experimental conditions. Second, the mass 33 to 32 ratio increased with increasing methanol concentration. These two effects suggest a change in proton solvation for the mixed system, but remain unexplained.

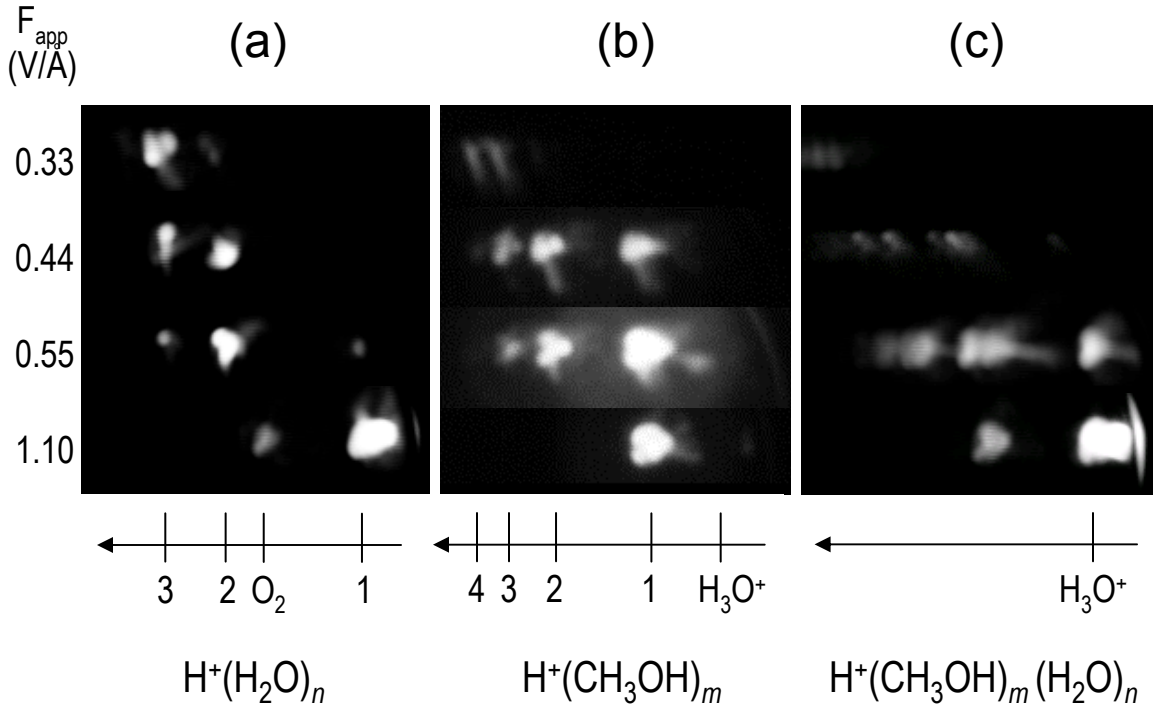

FIGURE 7-1: Wien filter separation of water, methanol and water / methanol ion clusters. Applied field is given on the left. (a) Water only. $P_{H2O} = 4x10^{-6}$ Torr. (b) Methanol only. $P_{MeOH} = 4x10^{-6}$ Torr. (c) Water / methanol mixture. $P_{H2O} = 2x10^{-6}$ Torr and $P_{MeOH} = 2x10^{-6}$ Torr. Lowest field shown is 0.39 V/Å instead of 0.33 V/Å.

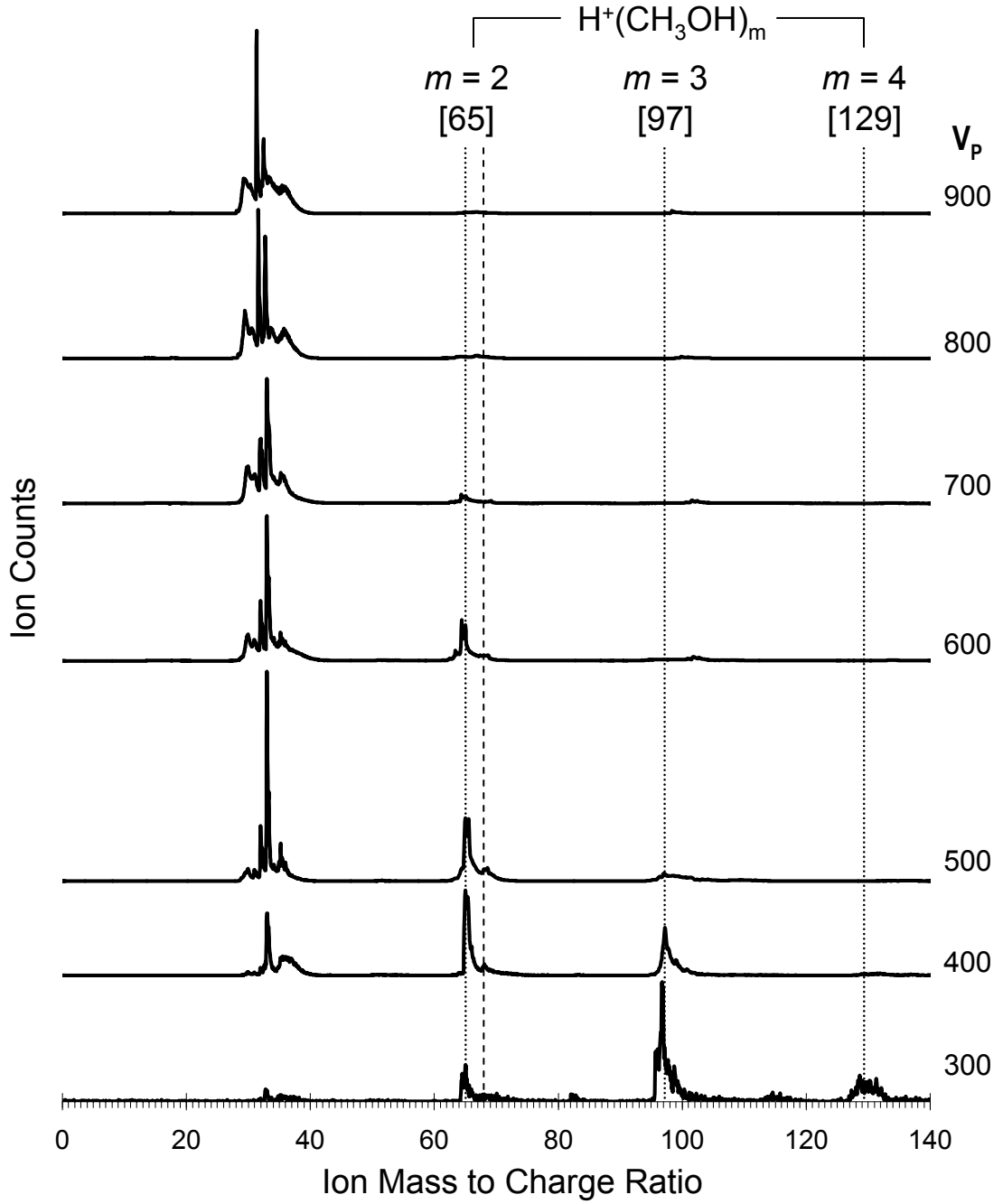

FIGURE 7-2: Pulsed ToF spectroscopy of protonated methanol clusters. Tip temperature is 165 K. $P_{MeOH} = 6x10^{-6}$ Torr. $V_{TIP} = 3000$ V. $V_{CE} = 2600$ V. Counter electrode pulsed negative by V_P given at right. The peak heights are normalized for comparative purposes.

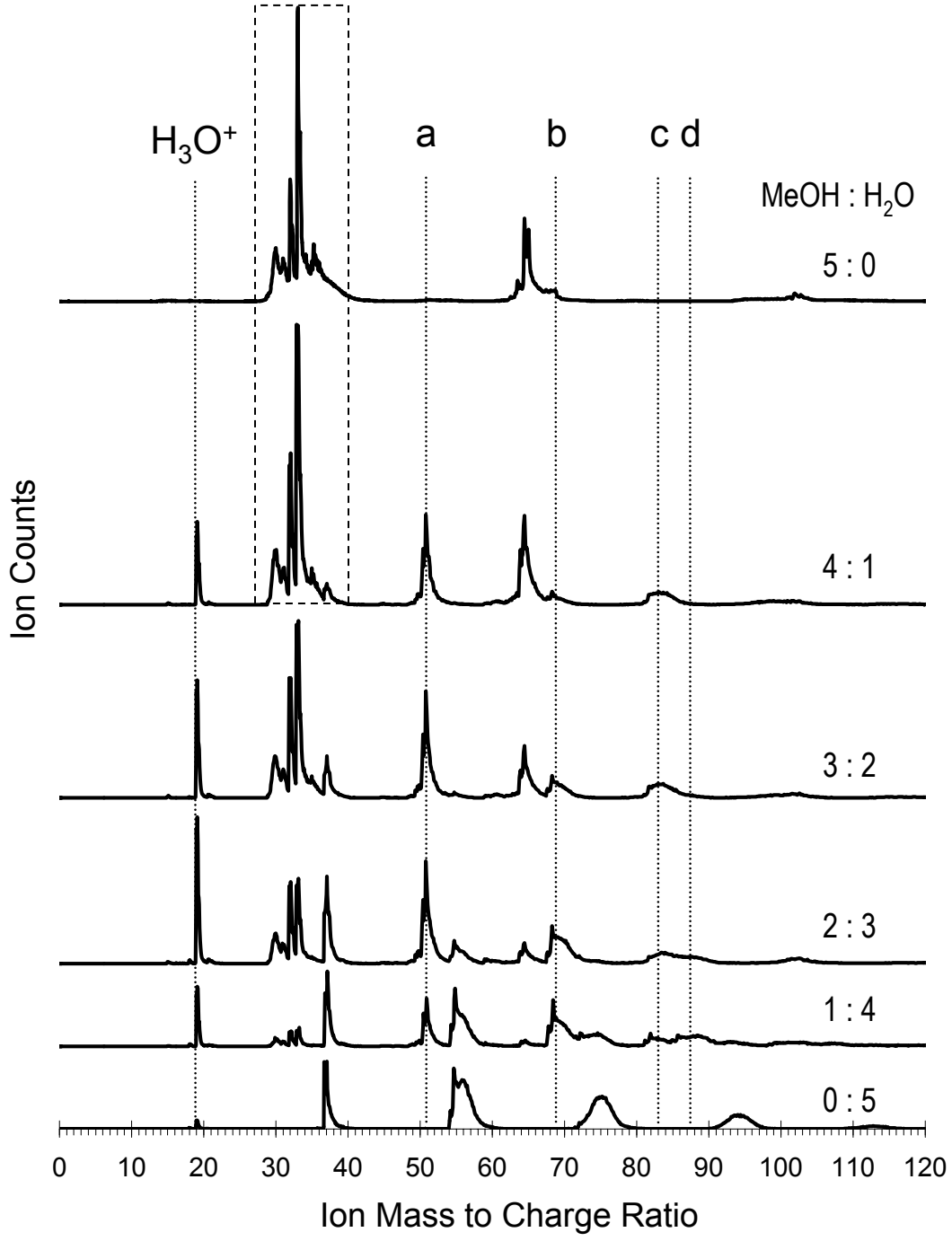

FIGURE 7-3: Pulsed ToF spectroscopy of mixed water / methanol clusters. Tip temperature is 165 K. V_{TIP} = 3000 V. V_{CE} = 2600 V. Counter electrode pulsed negative by V_P = 600 V. Methanol / Water ratio given on right, with $P_{MeOH} + P_{H2O} = 5x10^{-6}$ Torr. Note mixed $H^+(CH_3OH)_m (H_2O)_n$ with [m, n] equal to (a) [1, 1]; (b) [1, 2]; (c) [2, 1]; (d) [1, 3]. Dashed box is expanded in Figure 7-4.

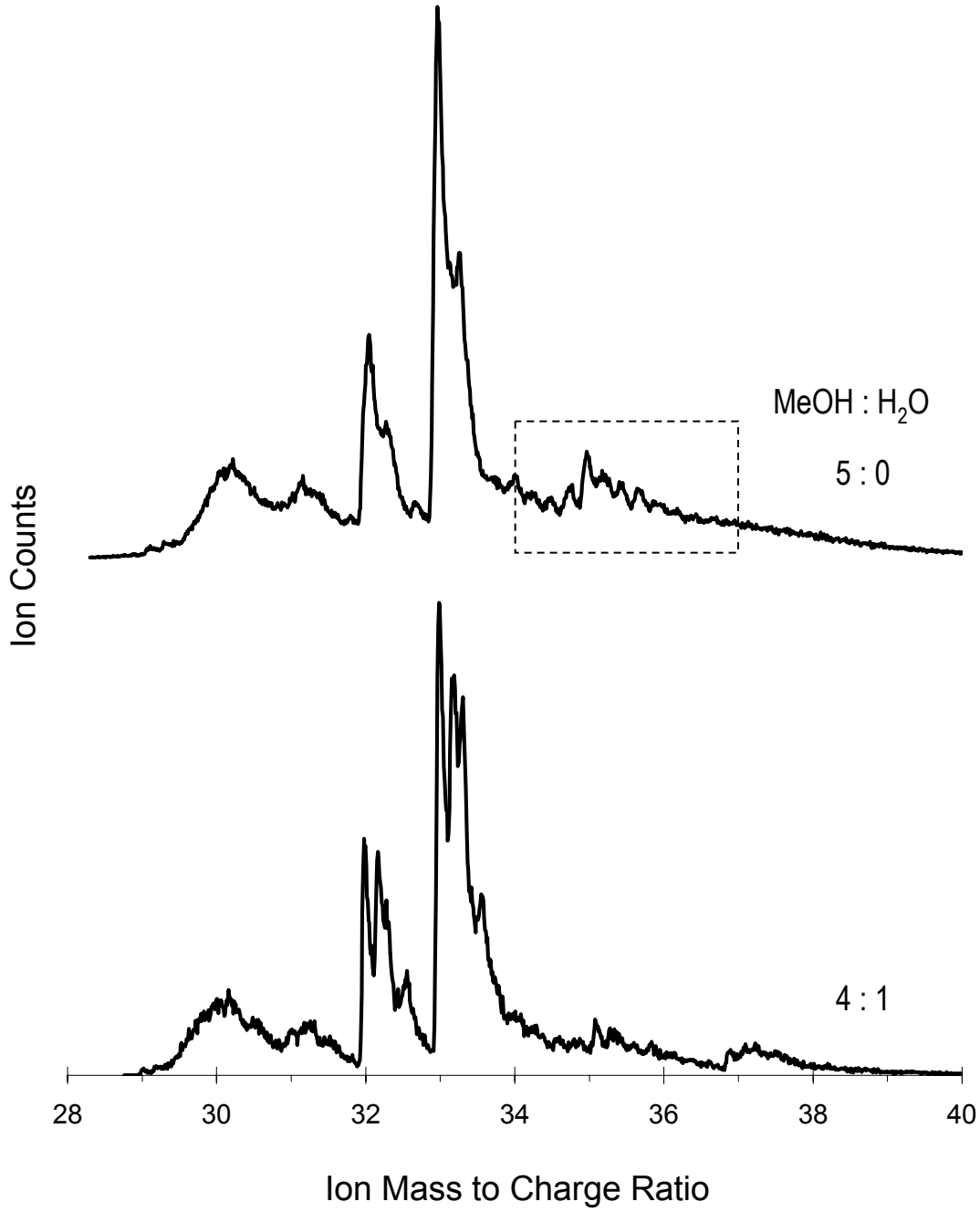

FIGURE 7-4: Mass complexity near *m* = 1 protonated methanol cluster. Expanded from Figure 7-3. Tip temperature is 165 K. V_{TIP} = 3000 V. V_{CE} = 2600 V. Counter electrode pulsed negative by V_P = 600 V. Methanol / Water ratio given on right, with $P_{MeOH} + P_{H2O} = 5x10^{-6}$ Torr. Dashed box expanded in Figure 7-5.

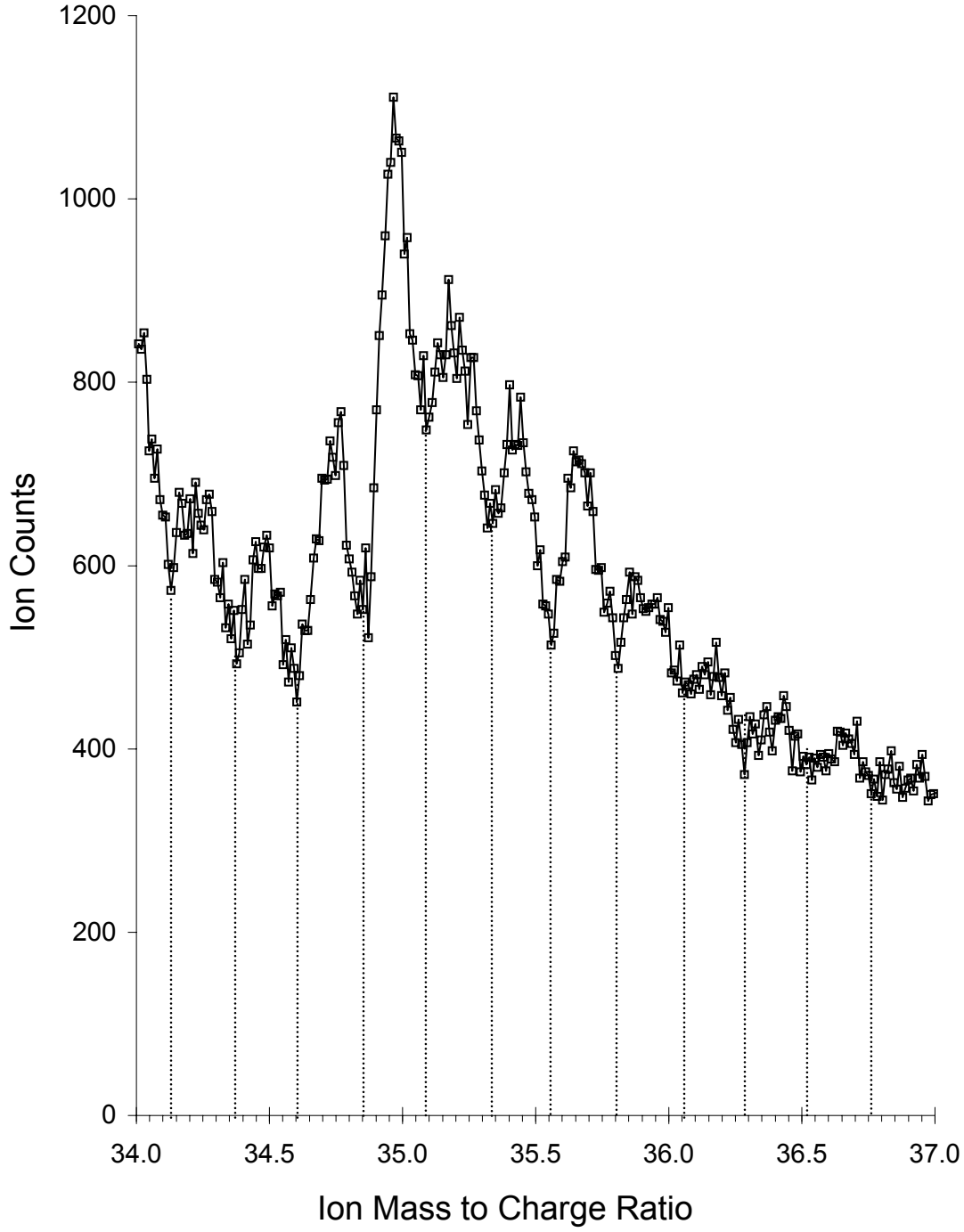

FIGURE 7-5: Mass to charge substructure near mass 35. Drop lines correspond to local minima. Average distance between minima is 0.239 ± 0.017. This corresponds to an average time of flight difference of 29 ± 2 ns based on a mass to charge ratio of 35.

TABLE 7-1: Ion cluster emission energies calculated for protonated methanol clusters.

Ion Cluster	ΔE_{emit} (eV)
H^+	14.19
$H^+(CH_3OH)$	6.81
$H^+(CH_3OH)_2$	5.91
$H^+(CH_3OH)_3$	5.49
$H^+(CH_3OH)_4$	5.28
$H^+(CH_3OH)_5$	5.19
$H^+(CH_3OH)_6$	5.13
$H^+(CH_3OH)_7$	5.11

TABLE 7-2: Excess emission energy $X^{m,n}$ calculated for protonated water / methanol clusters. Values represent the ion cluster emission energy $\Delta E^{m,n}$ minus the proton emission energy ΔE^{H+}. Values are in eV.

water (*n*) \ methanol (*m*)	0	1	2	3	4	5	6	7
0	0.00	-7.38	-8.28	-8.70	-8.91	-9.00	-9.06	-9.08
1	-6.77	-8.04	-8.64	-8.86	-8.99	-9.00		
2	-7.70	-8.51	-8.80	-8.93	-8.93			
3	-8.09	-8.71	-8.85	-8.89	-8.88			
4	-8.41	-8.78	-8.86	-8.85				
5	-8.47	-8.73	-8.84					
6	-8.51	-8.71						
7	-8.53							

TABLE 7-3: Possible ions near mass 32.

Mass	Possible Molecules
30	CH_2O^+, $C_2H_6^+$
31	CH_3O^+, $C_2H_7^+$
32	CH_3OH^+, O_2^+
33	$H^+(CH_3OH)$, $CH_3^+(H_2O)$, HO_2^+
35	$H_3O_2^+$

TABLE 7-4: Ion count ratio for masses 32 and 33 as a function of pulse height V_P.

	Ion Counts by Mass		
V_P	32	33	Ratio
300	9	73	0.12
400	1376	10693	0.13
500	63416	196751	0.32
600	70391	169199	0.42
700	109915	166171	0.66
800	245423	214381	1.14
900	263153	162437	1.62

TABLE 7-5: Ion count ratio for masses 32 and 33 as a function of MeOH to H_2O ratio.

	Ion Counts by Mass		
MeOH:H_2O	32	33	Ratio
1:4	2677	3308	0.81
2:3	14077	16581	0.85
3:2	20754	35109	0.59
4:1	24667	55461	0.44
5:0	70391	169199	0.42

CHAPTER 8: UHV SOLID OXID FUEL CELL STUDIES

The objective of these UHV solid oxide cell studies is to examine the fundamental surface chemistry of hydrocarbon oxidation to elucidate intermediates, reaction pathways, and kinetic parameters in electrocatalytic reactions. Of particular interest are the systems identified by Gorte and Vohs[102-104] and the existence of other fuel/catalyst combinations. Primary questions to be addressed include:

1. What are the surface intermediates and mechanisms involved in ceria-catalyzed direct oxidation of hydrocarbons?
2. Can suitable catalysts be found for direct hydrocarbon oxidation at temperatures lower than 700 °C?
3. What are the relative bond breaking tendencies for C–C, C–H, and C–O bonds in direct oxidation?
4. What is the role of surface/substrate oxygen in direct oxidation?
5. How might fuel properties and composition be tailored to facilitate direct oxidation in fuel cells?
6. Which fuels would be best for proton-conducting electrolytes and which would be best for oxygen ion-conducting electrolytes?

8.1 Technical Approach

Adsorption and subsequent dehydrogenation and decomposition of hydrocarbons and oxygenated hydrocarbons will be examined on a variety of

metal and metal/oxide substrates. The hydrocarbons are selected for their potential use in mid-temperature fuel cells. The substrates include those identified by Gorte and Vohs for direct oxidation SOFC (CeO_2 and Cu/CeO_2) along with potentially more active (and therefore lower temperature) substrates, such as Pt, Pt/CeO_2, and Pt/Al_2O_3. Nickel substrates will also be studied to characterize carbon formation for comparison with the other substrates.

Direct oxidation of hydrocarbons and oxygenated hydrocarbons will be examined to investigate relative tendencies for direct oxidation along with reaction mechanism and intermediates. The oxidizer will be supplied in several forms: O_2 from the gas phase, pre-adsorbed atomic oxygen, oxygen supplied by migration from the support (e.g., oxygen ions pumped through a YSZ electrolyte or supplied by ceria), and water (either coadsorbed or direct from the gas phase). These studies will identify the best candidates for direct oxidation in an SOFC application as well as those for direct oxidation by water in a mid-temperature fuel cell. Any unusually active fuel/catalyst combinations, which would facilitate lower temperature SOFCs, will be automatically identified in these studies. The selection of fuels and substrates is the same as with the adsorption studies.

Two experimental surface analysis chambers are being used for studying the catalytic activity, dehydrogenation and oxidation behaviors of the aforementioned systems. These are a field ionization system and a UHV SOFC system.

8.1.1 Field Ionization System

The influence of temperature and surface electric field on the reaction is being examined with the field emitter tip system. In this system the substrate is a field emitter tip (tip radius 100–1000 Å) for which the temperature and electric field are controlled over the ranges of 30–1200 K and 0–5 V/Å, respectively. The primary investigation techniques are temperature programmed reaction spectroscopy (TPRS) and field programmed reaction spectroscopy (FPRS) in which the temperature or field, respectively, is stepped or ramped to drive surface reactions.

Emitter tips made of Pt (or Ni) and can be oxidized in situ to form oxide coatings. Ceria coated Pt tips can be prepared to study the catalytic properties of ceria and Pt/ceria surfaces. Figure 8-1 shows a diagram of this emitter tip experimental system. A thin layer of ceria (or another oxide) can be deposited on the tip surface, followed by a sub-monolayer coverage of catalyst. Reactants may then be introduced into the vacuum chamber. Surface reaction (at selected field and temperature) leads to products that are field ionized and detected in pulsed mode by time-of-flight mass spectroscopy or in continuous mode by Wien filter (ExB) mass spectroscopy. The product ions may be imaged onto a phosphor screen using field ion microscopy (FIM) so that specific products can be correlated with specific sites on the metal tip. Local work function may be examined by field emission microscopy (FEM) as areas of low work function appear bright while areas of high work function appear dark in FEM images.

8.1.2 UHV SOFC System

A complete solid oxide fuel cell (SOFC) was being developed and built for operation within a UHV chamber to allow surface analysis of the catalyst/oxide surface during cell operation. The working electrode (WE) may then be analyzed either during or after operation with X ray photoelectron spectroscopy (XPS), auger electron spectroscopy (AES) or potentially a variety of other surface analysis techniques such as Fourier transform infrared spectroscopy (FTIR), or photoelectron emission microscopy (PEEM).

8.2 Developmental Progress

8.2.1 Field Ionization System

Two deposition sources were designed and built for use with the emitter tip. The first source was a cerium sublimation coil for deposition of cerium on the emitter tip. The second was a copper sublimation Knudsen tube. A schematic of both sources is shown in Fig. 8-2. The sources were mounted together on a tantalum foil assembly. Power leads were connected to each source and the tantalum foil serves as a common ground for both sources. Images of the assembled sources are shown in Fig. 8-3

A schematic of the cerium source is shown in Fig. 8-4a. It is a simple resistive heating source made of a 0.35 mm tungsten wire wrapped with a smaller 0.075 mm tungsten/rhenium wire. A small piece of cerium foil was placed in the center of the wire wrap to serve as the metal source. The source was heated resistively to sublimate the cerium for deposition on the emitter tip. The tungsten/rhenium wire served to localize the cerium and keep it from

diffusing away along the wire. A second generation of this source was fabricated with a different wire coil pattern to further improve localization.

Fig 8-4b is a schematic of the copper deposition Knudsen tube. A copper pellet was placed in a tantalum foil cylinder (14 mm x 5.8 mm) that can be resistively heated internally by a tungsten filament (0.25 mm) coil. The sublimated copper escapes through a small hole in the front of the cylinder and is deposited on the emitter tip.

Ceria deposition was carried out by first depositing sublimated cerium on the emitter tip and then oxidizing the deposited cerium. The process began by cleaning and imaging a Pt emitter tip to provide a pristine foundation. Fig. 8-5a shows a field emission micrograph of the clean Pt tip, and Fig. 8-5b shows a field ion micrograph of the same [111] oriented tip prior to deposition. The field emission micrograph for the clean Pt was performed at -0.43 V/Å. The emission field is dependent upon the work function of the surface. Cerium was then deposited on the Pt surface while 0.5 μA emission current was maintained on the emitter tip by controlling the applied field. As cerium was deposited, the required field diminished. Roughly one monolayer of coverage was assumed to have been deposited when the required field for maintaining emission current stabilized. After deposition, a third ion micrograph, shown in Fig. 8-5c, was taken. The field required to generate the micrograph (-0.15 V/Å) was roughly 1/3 that required for the clean Pt tip. This decrease was consistent with expectations, as the work function for cerium is lower than Pt. The tip was then annealed during field emission to observe surface diffusivity

of cerium on Pt. It was found that cerium is mobile on the Pt surface at 350 K. Fig. 8-5d shows a micrograph of the same Pt surface after the 350 K anneal.

The change in work function between the clean surface and the cerium coated surface was determined using the Fowler-Nordheim plot in Fig. 8-6. To generate this plot, the total tip current was set to 0.1, 0.3, 0.5 and 1.0 μA, both before and after deposition, and the required tip potentials were recorded. Theory suggests that the ratio of the work functions φ for clean and ceria coated tips is equal to the ratio of their respective Fowler-Nordheim slopes (as graphed) raised to the 2/3 power. Taking the literature value for clean platinum to be 5.65 eV gives an experimental φ for the ceria coated surface of 3.54 eV. The literature value for clean ceria is 2.9 eV.

Next the cerium coated Pt tip was oxidized to form ceria. The tip temperature was set to 450 K while in field emission mode imaging the Ce coated Pt. Oxygen at $5x10^{-5}$ Torr was introduced into the system to oxidize the surface. The FEM image darkened as the oxide formed due to the increased work function of the surface. Following oxidation, the deposition and oxidation procedures were repeated a second and third time each for a total of three layers of ceria. This ceria coated Pt tip is shown in Figure 8-7. Figure 8-7a is a field ion micrograph of the Pt tip imaged in H_2 at 2.2 V/Å and 110 K. Figure 8-7b is the same tip after ceria deposition, again imaged in H_2 under the same conditions. The tip orientation is not identical between Figures 8-7a and 8-7b due to a need to rotate the tip position during deposition. The ceria appears to

have some island structure or localizations, although the surface is reasonably uniform.

8.2.2 UHV SOFC System

The UHV solid oxide fuel cell apparatus has been designed and is shown in Figs 8-8 through 8-10. An initial prototype was machined from aluminum to suggest potential design improvements. A functional apparatus was then fabricated from Macor. The Macor maintains structural stability up to 1300 K which is sufficient for the intended experimental range. The cell was made from 1" OD Macor cylindrical stock, and measured 1.5" long. A 0.5" circular platform on the front of the cell provides support for the SOFC pellet. The pellet will be sealed to the Macor (using either gold or ceramic paster) leaving a 0.4" diameter, 0.3" deep, internal sealed reservoir where oxygen will be fed to the counter electrode, as shown in Fig 8-8b. The oxygen and electrical lead for the counter electrode come down through the top of the apparatus through a ceramic tube. This tube is also sealed to the Macor structure to avoid oxygen release. A nichrome heating wire wraps the outside of the apparatus. Finally nickel or stainless steel foil encases the Macor to aid in heat transfer (not shown) and reduce radiative heat losses.

Figure 8-9 is a top view schematic of the SOFC apparatus. The working electrode (WE) and reference electrode (RE) pass through the Macor structure and emerge near the SOFC pellet through holes at (a) and (b). The nichrome heating coil enters the apparatus through (c), wraps the apparatus ~14 times, and then is fed back through the Macor body and out at (d). The 0.250" and

0.125” concentric circles located at (e) are the oxygen feed through. The 0.125” hole is drilled down into the O_2 reservoir. The 0.250” hole is drilled coaxially to a depth of 0.250” to provide a surface for sealing the O_2 supply line. The temperature of the system is measured immediately above the SOFC pellet through a hole drilled at (f).

A front view of the support apparatus is shown in Figure 8-10. In the center is the platform for the SOFC pellet. Again two concentric holes were drilled to provide a narrow platform for the pellet to rest on. The outer and inner circles have 0.5” and 0.4” diameters respectively.

To achieve sufficient operating temperatures at a reasonable current (3 Amps for 0.5 mm nichrome), the apparatus was wrapped in a covering to simultaneously provide uniform heat transfer and to limit radiative heat loss. Alumina, nickel foil, and stainless steel coverings were tested and provided maximum operating temperatures of 660 K, 762 K and 1023 K, respectively. The stainless steel foil covering was wrapped 5 layers thick in an effort to minimize infrared emission, and was found to be sufficient for experiments.

Currently, SOFC pellets are under construction. A method for sealing the pellet to the apparatus must be found to eliminate crossover of the oxygen and fuel. Connecting the oxygen supply will also be a challenge. After these steps, the apparatus will be ready for experimental use. That will mark the beginning of a very productive investigation into the behavior of an operating solid oxide fuel cell, including the kinetics, reaction mechanisms and surface states for a variety of catalyst / fuel systems.

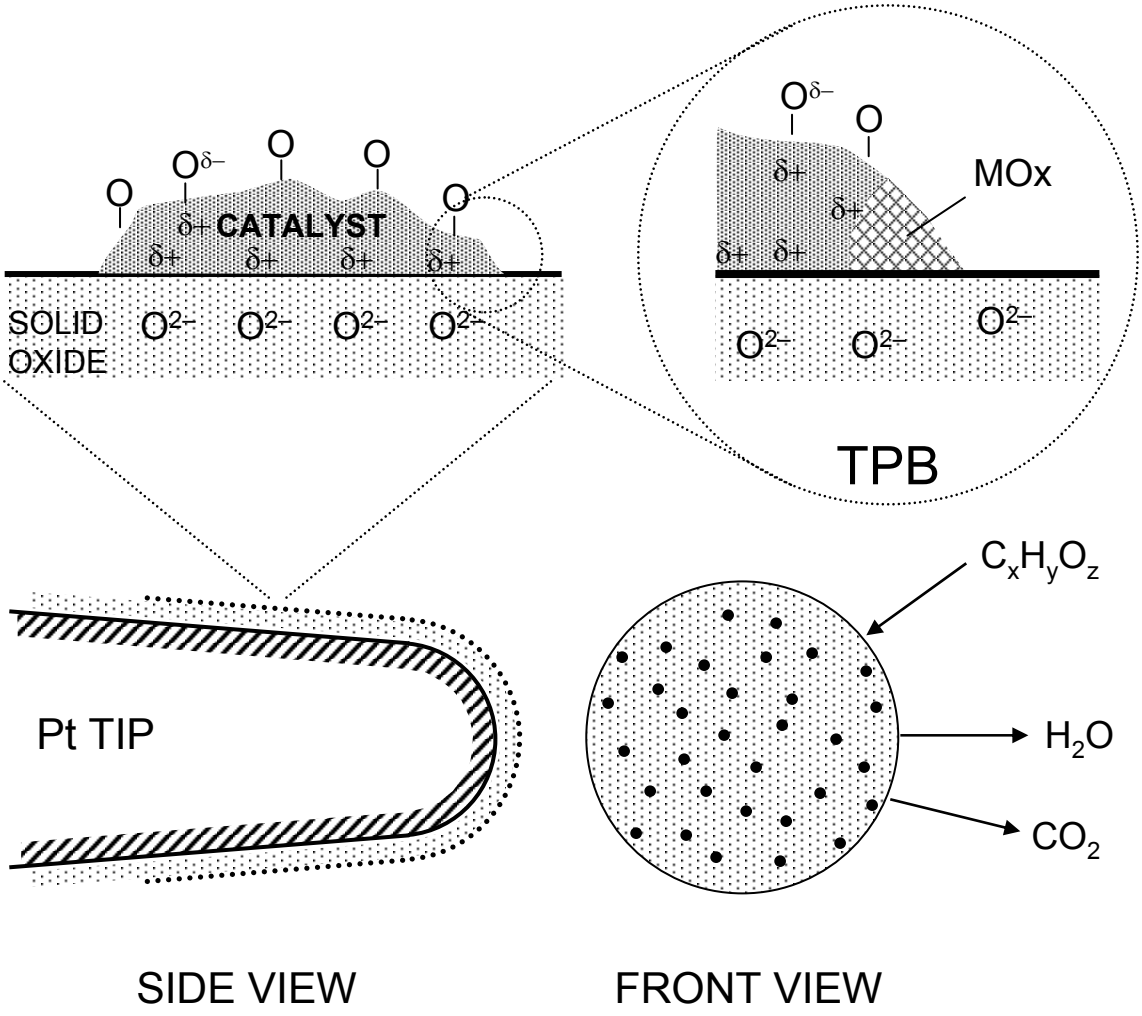

FIGURE 8-1: Pt / Oxide / Catalyst emitter tip design.

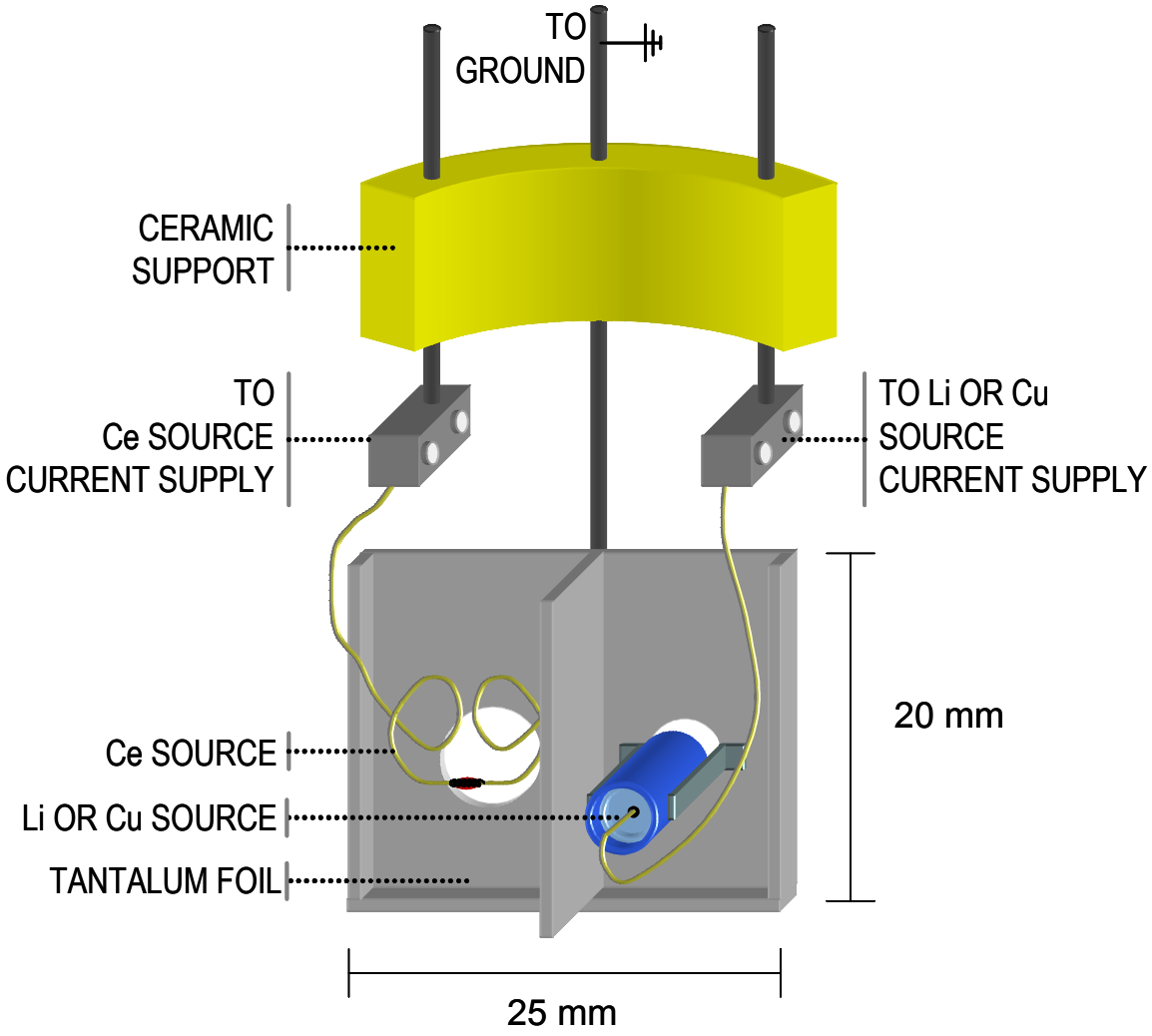

FIGURE 8-2: Source assembly schematic for cerium and copper or lithium source.

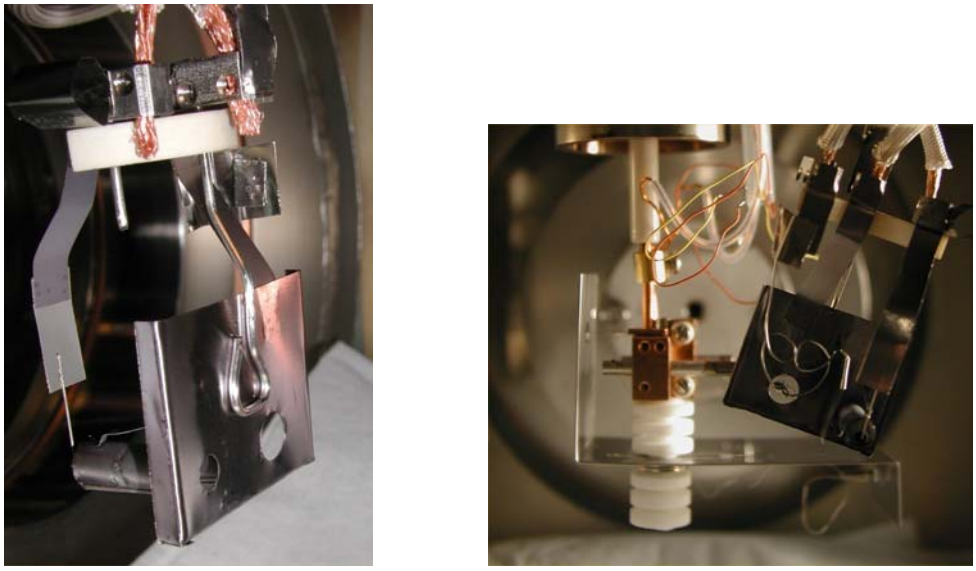

(a) (b)

FIGURE 8-3: Images of source assembly mounted in vacuum chamber. (a) Front view of source apparatus. (b) Rear view of assembly with tip apparatus on left.

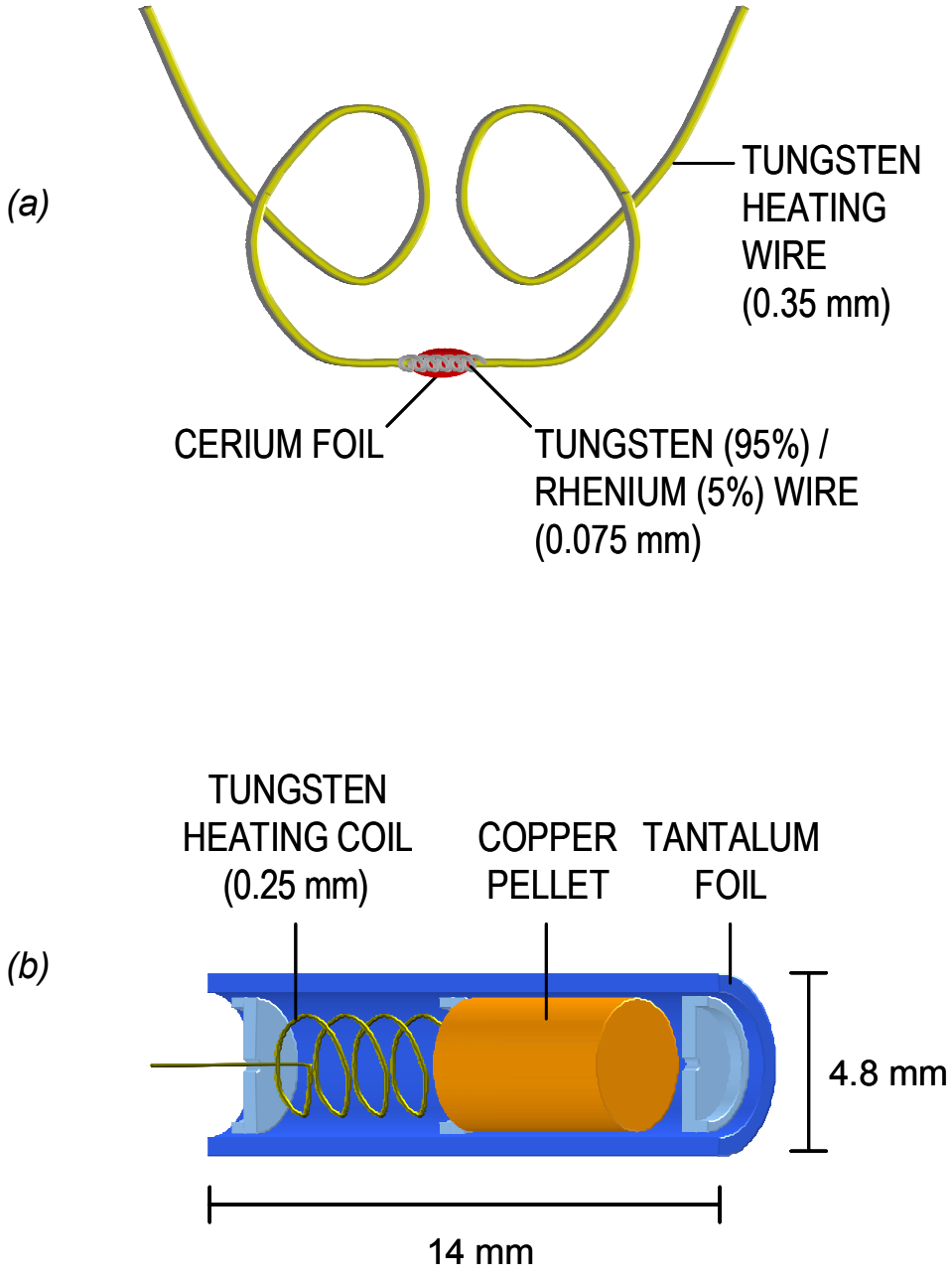

FIGURE 8-4: Source designs. (a) Simple resistive heating wire for cerium sublimation. (b) Copper or lithium source.

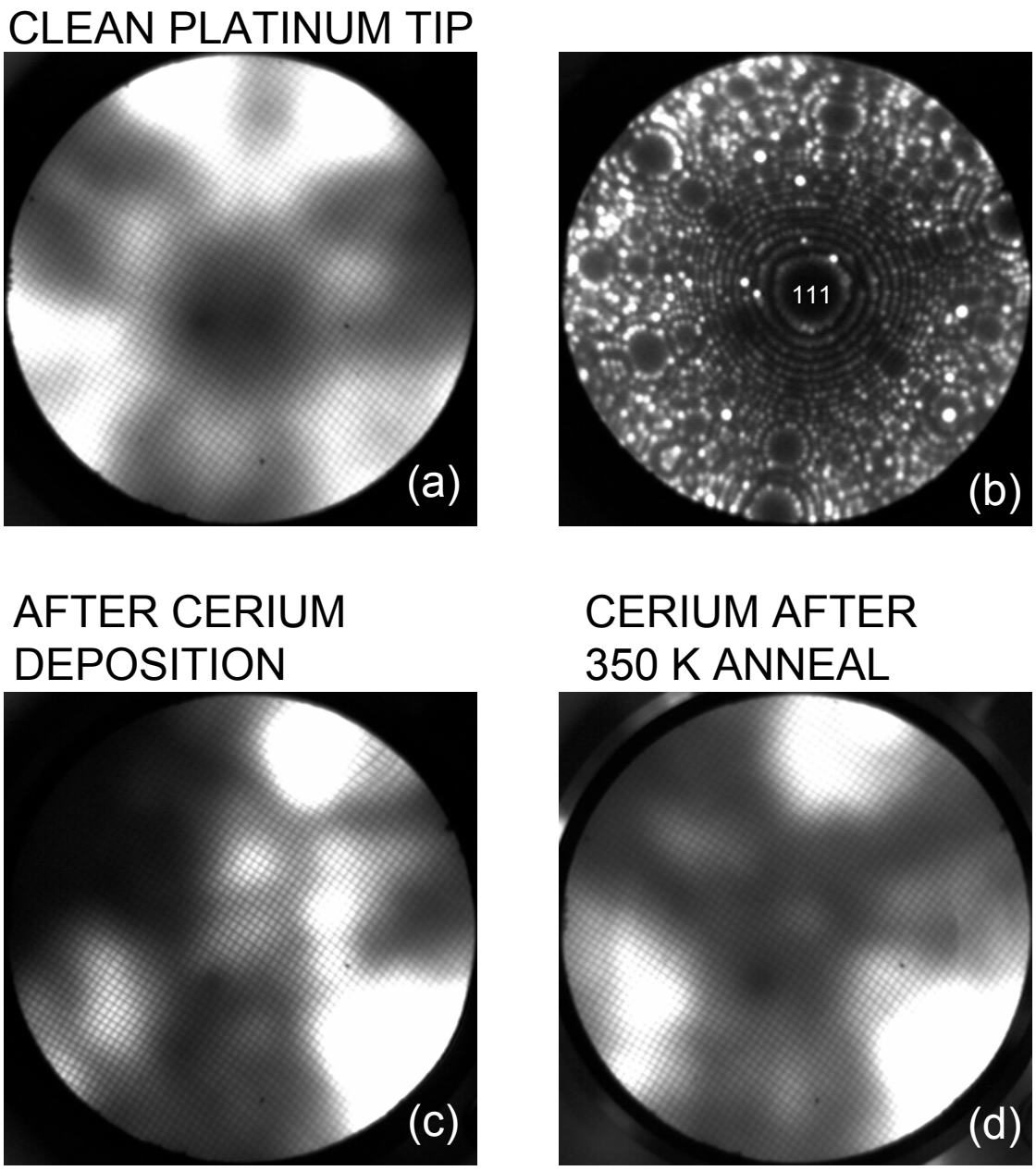

FIGURE 8-5: Micrographs depicting cerium deposition on Pt (111) tip of radius ~ 550 Å. (a) Field emission micrograph of clean Pt tip at -0.43 V/ Å. (b) Field ion micrograph of tip in 10-4 Torr Ne at 3.75 V/ Å. (c) Field emission micrograph of tip after cerium deposition -0.15 V/ Å. (d) Field emission micrograph of cerium coated tip after annealing to 350 K at -0.22 V/ Å.

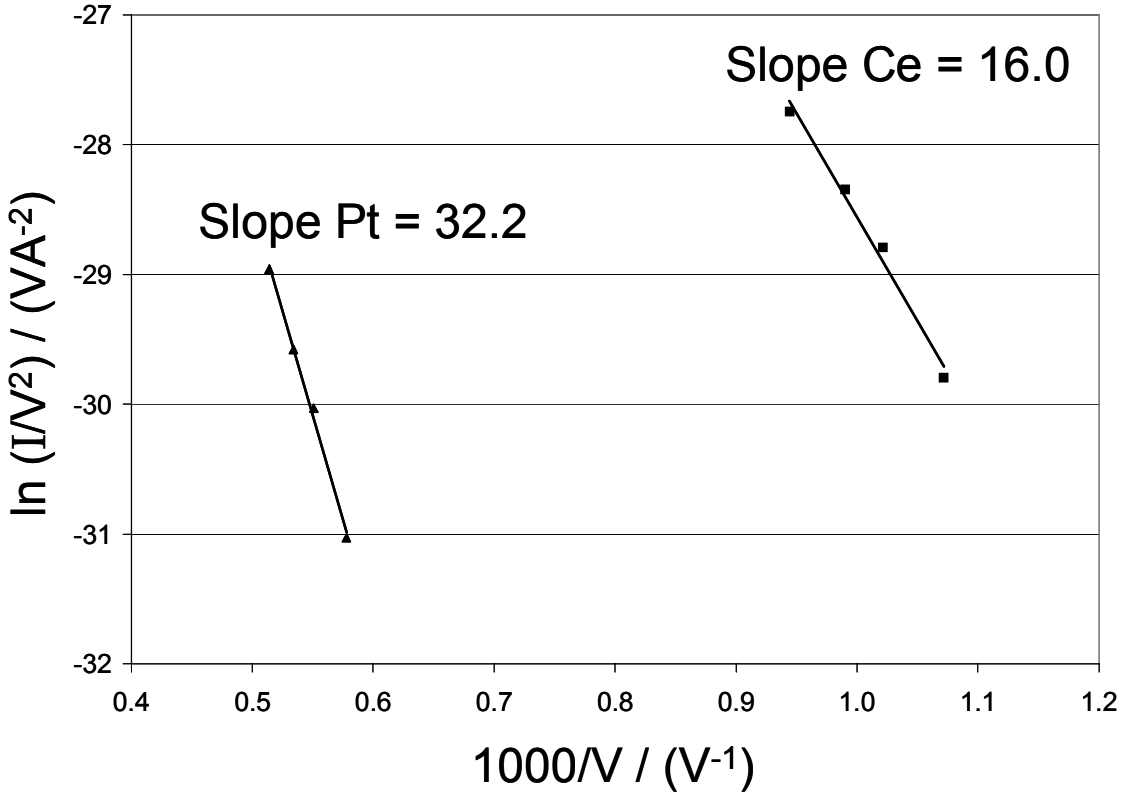

FIGURE 8-6: Fowler-Nordheim plot for calculation the change in work function after ceria deposition.

(a)

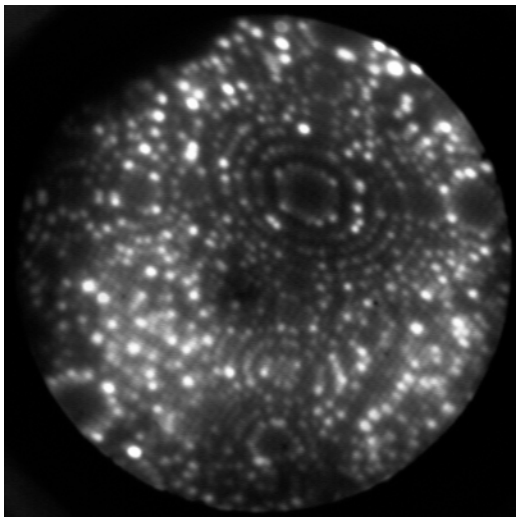

(b)

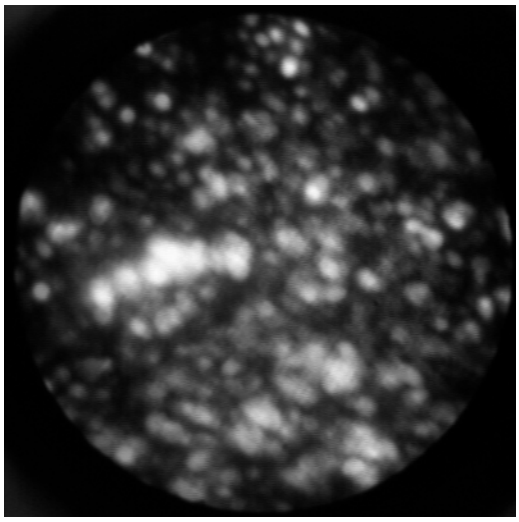

FIGURE 8-7: Field ion micrographs depicting ceria coating on Pt tip. (a) Clean Pt (100) tip imaged in hydrogen. (b) Ceria covered Pt tip imaged in hydrogen.

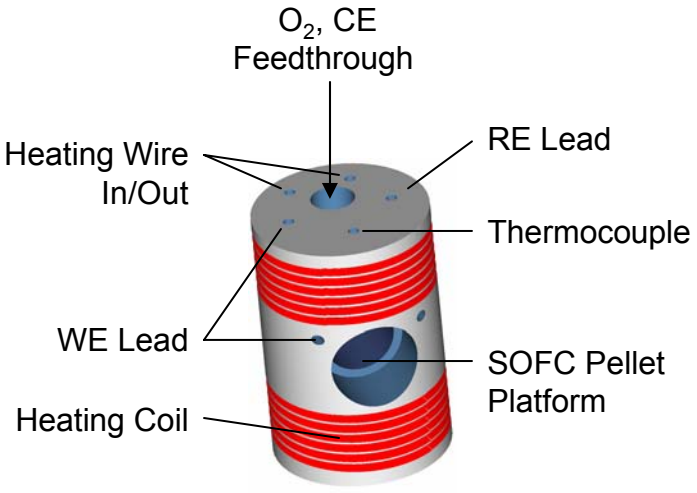

(a)

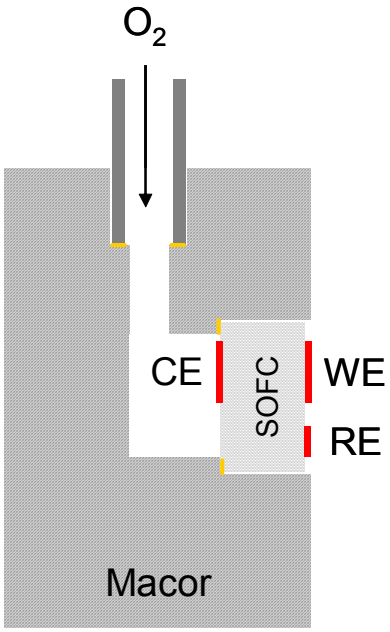

(b)

FIGURE 8-8: UHV SOFC Macor support apparatus schematic. Working, counter and reference electrodes are designated by WE, CE, and RE, respectively.

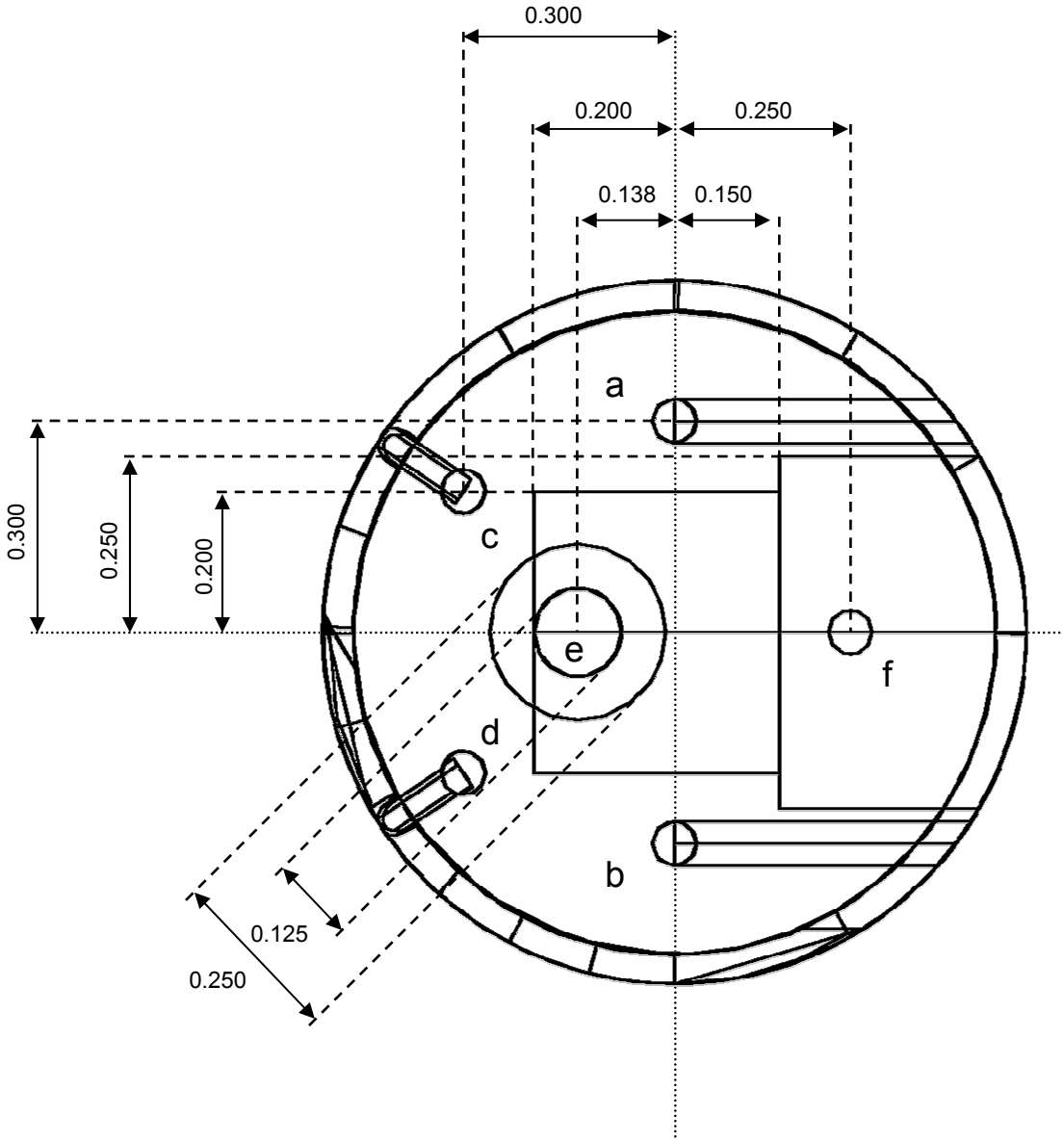

FIGURE 8-9: Top view of SOFC support apparatus (1" outside diameter). a and b are passthroughs for the working electrode (WE) and reference electrode (RE), c and d are the top and bottom feeds for the nichrome heating wire, e is the O_2 feedthrough, and f is a thermocouple access point.

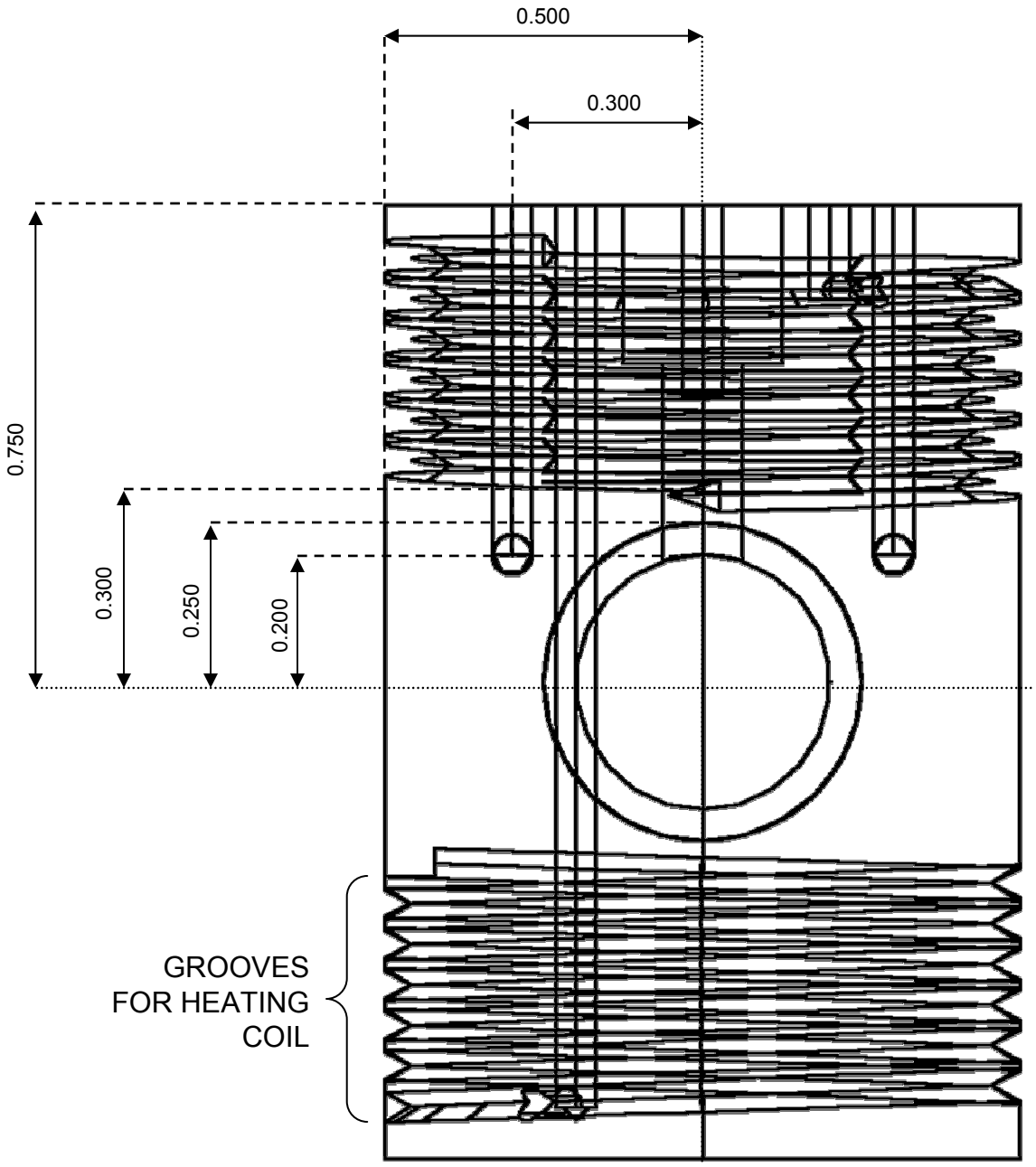

FIGURE 8-10: Front view of macor SOFC support apparatus.

CHAPTER 9: CONCLUDING REMARKS

9.1 Summary of Results

Understanding the behavior of molecules in high electric fields, particularly near catalyst surfaces, is of fundamental importance to electrochemistry and high field surface chemistry. Our recent work on the behavior of water molecules adsorbed on a Pt emitter tip in high fields (~1 V/Å) has provided an understanding of the behavior of water dissociation and ion cluster [$H^+(H_2O)_n$] emission. Water ion emission from an emitter tip has traditionally been treated as a single step event. While differing *n* cluster types have been observed in the past, typically ranging to 10 or above, no detailed explanation of the mechanism for cluster formation has been suggested.

In our experimental work, mass resolved ramped field desorption experiments from field adsorbed water layers (T > 170 K) have provided field dependencies for specific ion cluster masses. Water ion cluster formation in high electric fields was characterized on a Pt emitter tip over temperatures ranging from 170 to 300 K. Ion clusters emitted from the field-adsorbed water layer were mass resolved using a Wien filter. Two series of tests were conducted to characterize the ion cluster formation. In the first, tip temperature and water pressure were held constant while the applied field at the tip was ramped linearly with time. As the field was increased, water ion

clusters $H^+(H_2O)_n$ were emitted, beginning with large *n* clusters (up to 7) and proceeding through each lower *n* cluster in turn. The ion emission onset field was found to depend on the value of *n* and is lower for larger *n* clusters. The onset of ionization for each cluster was observed to be relatively constant as a function of temperature; however, ion signal intensity was temperature dependent. For the second series of tests, tip temperature was cyclically ramped while the applied field was held constant. The cyclical ramping experiments provided Arrhenius graphs showing thermal deactivation energies for ion emission from the tip. The observed deactivation corresponds to thermal desorption of the nth solvating water molecule of the ion cluster, i.e. the energy associated with the solvation of the proton by the nth solvating water molecule. These energies were found to be 0.85 eV, 0.76 eV and 0.55 eV for n = 3, 4 and 5, respectively.

At low temperatures (T < 150 K), for similar experiments, all observed ions appeared simultaneously at a critical onset field as the tip potential was ramped, demonstrating a common limiting reaction step. For these experiments, ramped field desorptions were carried out at 109 and 145 K. As the tip potential was linearly ramped, crystalline ice adsorbed at low temperatures (145 K) was ionized and emitted from the tip as protonated water clusters $H^+(H_2O)_n$. Emitted ions were mass resolved using a Wien filter for *n* up to 7. The onset of ionization occurred at a higher field for the 109 K RFDs (0.44 V/Å) than the 145 K RFDs (0.32 V/ Å). All observed ions for each temperature were observed simultaneously in the onset flash. However,

clusters n = 2 and 3, which were dominant at 109 K, were not observed at 145 K. These results, coupled with previous low temperature (109 - 150 K) ice field desorption data, and higher temperature (170 – 300 K) field adsorbed ion emission data, suggest a two step dissociative ionization/desorption mechanism in which the strongly temperature dependent dissociative ionization event determines emission onset at low temperatures, while the field dependent ion emission event determines emission onset at higher temperatures. In addition, local enhancement of the ionization event was observed by directly imaging ion cluster emission using field ion microscopy.

The experiments were extended to include methanol and mixed water methanol clusters. Pulsed time of flight mass spectrometry results of field adsorbed water / methanol layers on a Pt tip at 165 K demonstrated analogous behavior to the pure water system, but with richer spectra, particularly near mass 33. $H^+(CH_3OH)_m$ clusters were observed for m up to 4. Mixed $H^+(CH_3OH)_m(H_2O)_n$ clusters were also observed. The presence of methanol served to facilitate emission of H_3O^+ under conditions where emission did not occur for water only systems.

In preparation for a transition to high temperature solid oxide fuel cell studies, methods were developed for preparing ceria coated platinum tips. Field emission microscopy work function studies confirmed the deposition of cerium on a platinum tip. The cerium was then oxidized to provide a cerium covered tip, and the deposition was repeated to thicken the layer. Additionally a UHV solid oxide fuel cell experimental system has been designed. The

ceramic support apparatus has been produced and successfully tested at temperatures up to 1000K.

9.2 Conclusions

The two step ion dissociation and emission mechanism outlined in this dissertation provides a framework for explaining observations in previous literature discussing ion cluster emission from emitter tips. In Anway's discussion[79] of the field ionization of water, he suggested an adlayer with "long whiskers of water molecules oriented dipole to dipole" extending out from the tip surface. This provided an explanation of how large clusters could be emitted in a single ionization event, and was consistent with his experimental observations. Significant work by Block's group[80, 93, 94] on field assisted photodesorption of water (and other molecules) from emitter tips was carried out that supported the whisker model. However, there were some suggestions among their results that the whisker model was incomplete. The two step mechanism appears to address these concerns.

The experiments performed by Jaenicke, et al.[80, 93] were carried out at low temperature (80 K) with ice layers deposited in the presence of a field, and a continuous background pressure of water. Molecules were ionized by synchrotron radiation (~ 175 nm) in the presence of an applied field. Looking back on their research in light of our results suggests that they were operating at fields above the desorption barrier for all cluster types, but below the dissociation barrier. The synchrotron radiation provided sufficient energy (and more) for the dissociation event to occur, and then the field was sufficient

for cluster emission. Among their observations are several that should be revisited with consideration of a two step mechanism.

Jaenicke, et al. found that with no field present, only protons were emitted from the surface, while at an applied field of 1 V / Å, protonated water clusters with n up to 16 were observed. While this is consistent with a whisker model, it is also consistent with the two step mechanism. In the absence of a field, protons formed by the dissociating radiation lack further energy for emission from the surface. Jaenicke suggests that emission of protons is simply due to bond cleaving of surface molecules, which is reasonable, especially if it is a multi-photon event. Under field conditions, the whisker model contends that one of the whisker constituents is ionized by the synchrotron radiation, essentially snipping off the whisker at the point of ionization. This provides an explanation for the formation of large clusters in general, but there are a number of areas where it falls short. In particular, there is no way of accounting for the observed ion cluster distributions. In fact they found it[80] "remarkable that under these conditions almost no monomers and very few dimers were detected." Based on the whisker model, it is reasonable to assume that in every situation the monomer and dimer would dominate. This is due to the fact that every n length whisker contains the set of all smaller cluster types. There is no obvious reason why photo-ionization would occur preferentially towards the base of the whisker, so monomers and dimers would be expected in a single step process that does not account for solvation energies. However, in the two step mechanism,

ionization and emission are temporally separated and both strongly influenced by solvation. These photon assisted desorption experiments are analogous to the low temperature ramped field desorption experiments discussed in Chapter 6. However, instead of ramping up to the dissociation barrier, the field is stabilized just below the barrier, and then individual molecules are kicked over it with the radiation.

Dirks, et al.[106] extended this work to include a study of the effect of temperature variation (80 – 140 K). They observed that the cluster size distribution varied with temperature, favoring larger clusters at higher temperatures, which they attributed to the increase in "translational transport". While the translational transport may be able to explain an increase in the higher mass clusters, it does not explain the complete absence of $H^+(H_2O)$ and $H^+(H_2O)_2$ clusters in their 120 K and 140 K spectra. However, Figure 6-5 suggests that at these temperatures, the dissociation barrier is below the emission barrier for $H^+(H_2O)$ and $H^+(H_2O)_2$ clusters, so with the two step mechanism, the surprising lack of low mass clusters is actually expected.

The two step mechanism nicely explains the Block group observations, but it was largely Anway's energy deficit data[77] that led to the acceptance of the whisker hypothesis. The whisker model allowed for ions to form at variable distances from the emitter tip, providing an explanation for the observed energy deficit data. The hump formation and ion dissociation localization described in Chapter 6 provides the same 3 dimensional

characteristics that Anway needed to explain his energy deficits, providing consistency with this earlier work as well.

More recently, Stintz and Panitz[79-81] performed experiments on water ion cluster formation from deposited ice layers on emitter tips. For these experiments the water was deposited under field free conditions and the field was ramped (at a variety of temperatures) to induce ion emission. Their observations included an increased ionization onset field at lower temperatures and a corresponding change in ion cluster distribution consistent with our low temperature work. An examination of these results shows them to be consistent with our proposed mechanism.

On the whole, the proposed mechanism for field induced dissociation and emission of water molecules (and methanol) is capable of explaining the experimental observations discussed in the prior literature, and overcoming the shortfalls of the previous whisker model. This is significant not only in tying up loose ends, but suggests that field adsorbed water layers are even better analogs to the electrochemical double layer than previously thought. Screening and solvation effects are critical to the behavior of the double layer. Under conditions where the behavior of the field adsorbed layer is dominated by solvation and charge screening, the emitter tip provides an excellent test bed for studying these phenomena.

The research in this dissertation suggests that the electrochemical double layer is significantly more complicated than the typical one dimensional field often used to describe it. The field anomalies created by

local dissociation events drive further dissociation events. As a consequence, the dissociation rate that may occur at the onset of dissociative ionization will not be the same as the steady state rate. Additionally, the extent of solvation has been shown to be important to the dissociative ionization. The water / methanol ratio influences the extent of solvation and the local field and the dissociation rate near the electrode surface will be influenced by the water methanol / ratio.

This research fits nicely with the observations of other recent investigations. Weaver, et al. have provided a great deal of insight into the electrochemical double layer through UHV surface science techniques. They have demonstrated (primarily through vibrational spectroscopy) the effect of solvation on surface adsorbed species[107, 108]and how adsorption sites can be shifted in the presence of a solvent[109]. Masel, et al. [110] investigated proton solvation on a platinum surface to determine the nature of the proton on the surface. They found that the simple hydronium was unlikely at that a higher degree of solvation (n = 2 through 4) was the preferred state. The water ion emission results in Chapter 5 support these findings, suggesting that the higher degree of solvation is energetically favorable on the platinum surface. Their earlier investigations into the decomposition of methanol showed a difference in the dehydrogenation mechanism for the UHV and electrochemical systems. They showed that the UHV system begins by breaking the O-H bond, while the electrochemical system begins with one of the C-H bonds. This difference was attributed to the effect of the solvation shell. The emitter tip

system differs from the UHV system examined in Masel's work. For the emitter system, the field adsorbed layer allows for solvation similar to the double layer, suggesting that the methanol dehydrogenation on the emitter surface may also lead with a breaking of the C-H bond.

BIBLIOGRAPHY

1. D. Price and J. W. Halley, Journal of Electroanalytical Chemistry, 1983. **159**: p. 347.
2. J. Kreuzer, Surface Science, 1991. **246**: p. 336-347.
3. W. Schmickler, *Tunneling of electrons through thin layers of water.* Surface Science, 1995. **335**(1-3): p. 416-21.
4. M. J. Weaver and S. A. Wasileski, *Influence of Double-Layer Solvation on Local versus Macroscopic Surface Potentials on Ordered Platinum-Group Metals as Sensed by the Vibrational Stark Effect.* Langmuir, 2000. **17**: p. 3039-3043.
5. J. K. Sass, Vacuum, 1983. **33**: p. 741.
6. E. M. Stuve and N. Kizhakevariam, *Chemistry and physics of the 'liquid'/solid interface: a surface science perspective.* Journal of Vacuum Science & Technology A, 1993. **11**(4): p. 2217-24.
7. M. J. Weaver, N. Kishakevariam, and X. Jiang, *Infrared Spectroscopy of Model Electrochemical Interfaces in Ultrahigh Vacuum: The Archetypical Case of Carbon Monoxide/Water Coadsorption on Pt(111).* Journal of Chemical Physics, 1994. **100**: p. 6750.
8. K. Bange, et al., *The Interaction of Br with Ag(110): Comparison of Electrochemical and Gas-Phase Adsorption Measurements.* Journal of Electroanalytical Chemistry, 1987. **229**: p. 87-98.
9. J. K. Sass, K. Kretzxchmar, and S. Holloway, *Water adsorption on metal surfaces: an electrochemical viewpoint.* Vacuum, 1981. **31**(10-12): p. 483-486.
10. Eric M. Stuve, A. Krasnopoler, and D.E. Sauer, *Relating the In-Situ, Ex-Situ, and Non-Situ Environments in Surface Electrochemistry.* Surface Science, 1995. **335**: p. 177-185.
11. I Villegas and M. J. Weaver, *Infrared Spectroscopy of Model Electrochemical Interfaces in Ultrahigh Vacuum: Roles of Solvation in the Vibrational Stark Effect.* Journal of Physical Chemistry, 1997. **101**: p. 5842-5852.
12. R. Gomer, *Field Emission and Field Ionization*. 1961, Cambridge: Harvard University Press.
13. T.T. Tsong, *Atom-Probe Field Ion Microscopy*. 1990, Cambridge: Cambridge University Press.
14. M. K. Miller, *Atom Probe Tomography. Analysis at the Atomic Level*. 2000, New York: Kluwer Academic / Plenum.
15. H.D. Beckey, *Principles of Field Ionization and Field Desorption Mass Spectrometry*. International Series in Analytical Chemistry, ed. R. Belcher and H. Frieser. Vol. 61. 1977, Oxford: Pergamon Press. 335.

16. V.K. Medvedev, N.N. Popovich, and A.O. Snitko, *Investigation of the supply of the working substance to the vertex of the tip in a cryogenic ion source.* Soviet Physics, Technical Physics, 1991. **36**(2): p. 223-227.
17. R.H. Fowler and L. Nordheim, Proc. Roy. Soc. A, 1928. **119**.
18. E.W. Müller, Z. Physik, 1937. **106**: p. 541.
19. E.W. Müller and T.T. Tsong, *Field Ion Microscopy*. 1969, New York: American Elsevier Publishing Company.
20. E. L. Murphy and R. H. Good, *Thermionic Emission, Field Emission, and the Transition Region.* Physical Review, 1956. **102**(6): p. 1464-1473.
21. Richard G. Forbes, *Refining the application of Fowler-Nordheim theory.* Ultramicroscopy, 1999. **79**: p. 11-23.
22. K. F. Wojciechowski, A. Kiejna, and H. Bogdanow, *Face-dependent work function derived from the local polarization of plasma and the image force action near a metal surface.* Modern Physics Letters B, 1999. **13**(29 & 30): p. 1081-1085.
23. D.L. Scovell, et al., *Field distributions in thin water films - a comparison of theoretical and empirical trends.* Proceedings of the Electrochemical Society, 1999. **5**: p. 6-14.
24. E.W. Müller, Z. Physik, 1951. **131**: p. 136.
25. T.T. Tsong, *Atom-probe field ion microscopy - Field ion emission and surface and interfaces at atomic resolution*. 1990, Cambridge: Cambridge University Press.
26. D. G. Brandon, *The structure of field-evaporated surfaces.* Surface Science, 1965. **3**(1): p. 1-18.
27. Tien T. Tsong, *On the mechanism of field evaporation.* Surface Science, 1968. **10**(1): p. 102-117.
28. P. A. Thiel and T. E. Madey, *The interaction of water with solid surfaces: Fundamental aspects.* Surface Science Reports, 1987. **7**(6-8): p. 211-385.
29. Michael A. Henderson, *The interaction of water with solid surfaces: fundamental aspects revisited.* Surface Science Reports, 2002. **46**: p. 1-308.
30. D.R. Lide, ed. *Handbook of Chemistry and Physics*. 76th ed. 1995, CRC Press: Boca Raton.
31. J. B. Hasted, *Liquid water: Dielectric properties*, in *Water A Comprehensive Treatise*, F. Franks, Editor. 1972, Plenum Press: New York. p. 255-309.
32. K. Ichikawa, et al., *Neutron-diffraction investigation of the intramolecular structure of a water molecule in the liquid-phase at high-temperatures.* Molecular Physics, 1991. **73**: p. 79-86.
33. P.V. Hobbs, *Ice Physics*. 1974, London: Oxford University Press.
34. W. B. Holzapfel, *Evasive ice X and heavy fermion ice XII: facts and fiction about high-pressure ices.* Physica B, 1999. **265**: p. 113-120.
35. C. Lobban, J. L. Finnery, and W. F. Kuhs, *The structure of a new phase of ice.* Nature, 1998. **391**(268-270).

36. M. Benoit, M. Bernasconi, and M. Parrinelio, *New high-pressure phas of ice.* Physical Review Letters, 1996. **76**: p. 2934-2936.
37. S. J. La-Placa, et al., *On a nearly proton-ordered structure for ice IX.* Journal of Chemical Physics, 1973. **58**: p. 567-580.
38. K. Vonnegut, *Cat's Cradle*. 1963, London: Penguin.
39. Z. Dohnalek, et al., *The effect of the underlying substrate on the crystallization kinetics of dense amorphous solid water films.* Journal of Chemical Physics, 2000. **112**(13): p. 5932-5941.
40. R. S. Smith, et al., *The Molecular Volcano: Abrupt CCl4 Desorption Driven by the Crystallization of Amorphous Solid Water.* Physical Review Letters, 1997. **79**(5): p. 909-912.
41. Z. Dohnalek, et al., *Substrate induced crystallization of amorphous solid water at low temperatures.* Journal of Chemical Physics, 1999. **110**(12): p. 5489-5492.
42. R.J. Speedy, et al., *The evaporation rate, free energy, and entropy of amorphous water at 150 K.* Journal of Chemical Physics, 1996. **105**(1): p. 240-244.
43. Greg A. Kimmel, et al., *Control of amorphous solid water morphology using molecular beams. I. Experimental results.* Journal of Chemical Physics, 2001. **114**(12): p. 5284-5294.
44. Greg A. Kimmel, et al., *Control of amorphous solid water morphology using molecular beams. II. Ballistic deposition simulations.* Journal of Chemical Physics, 2001. **114**(12): p. March 22, 2001.
45. R. Scott Smith, et al., *The self-diffusivity of amorphous solid water near 150 K.* Chemical Physics, 2000. **258**: p. 291-305.
46. K. P. Stevenson, et al., *Controlling the morphology of amorphous solid water.* Science, 1999. **283**(5407): p. 1505-1507.
47. P. Jenniskens and D.F. Blake, *Structural transitions in amorphous water ice and astrophysical implications.* Science, 1994. **265**: p. 753-756.
48. P. Jenniskens, et al., *Liquid water in the domain of cubic crystallic ice I_c.* Journal of Chemical Physics, 1997. **107**(4): p. 1232-1241.
49. F. Franks, *Water: A matrix of life 2nd Edition*. 2000, Cambridge: Royal Society of Chemistry.
50. N. Materer, et al., *Molecular surface structure of ice(0001): dynamical low-energy electron diffraction, total-energy calculations and molecular dynamics simulations.* Surface Science, 1997. **381**: p. 190-210.
51. R. Cardenas, J. Lagunez-Otero, and A. Flores-Rivero, *Ab Initio Study of the Reaction Mechanism of Water Dissociation into the Ionic Species OH^- and H_3O^+.* International Journal of Quantum Chemistry, 1998. **68**(4): p. 253-259.
52. P.L. Geissler, et al., *Autoionization in Liquid Water.* Science, 2001. **291**(16 March): p. 2121-2124.
53. Branko Ruscic, et al., *Evidence for a lower enthalpy of formation of hydroxyl radical and a lower gas-phase bond dissociation energy of water.* Physical Chemistry A, 2001. **105**(1): p. 1-4.

54. L. Rene Corrales, *Dissociative model of water clusters.* Journal of Chemical Physics, 1999. **110**(18): p. 9071-9080.
55. Jun-Hyung Cho, Jung Mee Park, and Kwang S. Kim, *Influence of intermolecular hydrogen bonding on water dissociation at the MgO(001) surface.* Physical Review B, 2000. **62**(15): p. 9981-9984.
56. P. J. D. Lindan, et al., *First-principles molecular dunamics simulations of water dissociation on TiO_2 (110).* Chemical Physics Letters, 1996. **261**: p. 246-252.
57. I. M. Brookes, C. A. Muryn, and G. Thornton, *Imaging Water Dissociation on TiO_2(110).* Physical Review Letters, 2001. **87**(26): p. 1-4.
58. Joseph Berkowitz, G. Barney Ellison, and David Gutman, *Three Methods to Measure RH Bond Energies.* Journal of Physical Chemistry, 1994. **98**: p. 2744-2765.
59. M. Meot-Ner, *Comparitive stabilities of cationic and anionic hydrogen-bonded networks. Mixed clusters of Water-Methanol.* Journal of the American Chemical Society, 1986. **108**(20): p. 6189-6197.
60. Michael D. Tissandier, et al., *The proton's absolute aqueous enthalpy and gibbs free energy of solvation from cluster-ion solvation data.* Journal of Physical Chemistry A, 1998. **102**: p. 7787-7794.
61. D.W. Smith, *Ionic Hydration Enthalpies.* Journal of Chemical Education, 1977. **54**(9): p. 540-542.
62. Dongqing Wei and D. R. Salahub, *Hydrated proton clusters: Ab initio molecular dynamics simulation and simulated annealing.* Journal of Chemical Physics, 1997. **106**(14): p. 6086-6094.
63. Diane E. Sagnella and M. Tuckerman, *An emipirical valence bond model for proton transfer in water.* Journal of Chemical Physics, 1998. **108**(5): p. 2073-2083.
64. M. Tuckerman, et al., *Ab initio molecular dynamics simulation of the solvation and transport of hydronum an hydroxyl ions in water.* Journal of Chemical Physics, 1995. **103**(1): p. 150-158.
65. L. A. Montero, J. Molina, and J. Fabian, *Multiple Minima Hypersurfaces of Water Clusters for Calculations of Association Energies.* International Journal of Quantum Chemistry, 2000. **79**(1): p. 8-16.
66. J.A. Mejias and S. Lago, *Calculation of the absolute hydration enthalpy and free energy of H+ and OH-.* Journal of Chemical Physics, 2000. **113**(17): p. 7306-7315.
67. R. E. Kozack and P. C. Jordan, *Empirical models for the hydration of protons.* Journal of Chemical Physics, 1992. **96**(4): p. 3131-3136.
68. Matthew P. Hodges and Anthony J. Stone, *Modeling small hydronium-water clusters.* Journal of Chemical Physics, 1999. **110**(14): p. 6766-6772.
69. A.A. Tsekouras, M.J. Iedema, and J.P. Cowin, *Amorphous Water-Ice Relaxations Measured with Soft-Landed Ions.* Physical Review Letters, 1998. **80**(26): p. 5798-5801.

70. Chigusa Kobayashi, Shinji Saito, and Ohmine Iwao, *Mechanism of fast proton transfer in ice: Potential energy surface and reaction coordinate analyses.* Journal of Chemical Physics, 2000. **113**(20): p. 9090-9100.
71. Friedrich Huisken, Saeed Mohammad-Pooran, and Olav Wehahn, *Vibrational spectroscopy of single methanol molecules attached to liquid water clusters.* Chemical Physics, 1998. **239**: p. 11-22.
72. Takaaki Sato, Akio Chiba, and Ryusuke Nozaki, *Hydrophobic hydration and molecular association in methanol-water mixtures studied by microwave dielectric analysis.* Journal of Chemical Physics, 2000. **112**(6): p. 2924-2932.
73. A. W. Wisniewski, M. A. Hershberger, and A. W. Castleman, *Solvation effects on electronic excited states of methanol: A study of neat and mixed methanol/water clusters.* Journal of Chemical Physics, 2002. **116**(13): p. 5738-5745.
74. Y. J Shi, et al., *A 118 nm vacuum ultraviolet laser/time of flight mass spectroscopic study of methanol and ethanol clusters in vapor phase.* Journal of Chemical Physics, 2002. **116**(16): p. 6990-6999.
75. Muhammad Iraqi and Chava Lifshitz, *Studies of ion clusters of atmospheric importance by tandem mass spectrometry. Neat and mixed clusters involving methanol and water.* International Journal of Mass Spectrometry and Ion Processes, 1989. **88**(1989): p. 45-57.
76. J. R. Stairs, et al., *Calculation to determine the mass of daughter ions in metastable decay.* International Journal of Mass Spectrometry, 2002. **213**: p. 81-89.
77. M.G. Inghram and R. Gomer, Z. Naturforschg., 1955. **10a**: p. 863.
78. W.A. Schmidt, *Massenspektrometrische Untersuchung der Feldionisation von Wasserdampf an Spitzen aus Wolfram, Platin and Iridium.* Z. Naturforschg, 1964. **19a**: p. 318-327.
79. A. R. Anway, *Field Ionization of Water.* The Journal of Chemical Physics, 1969. **50**(5): p. 2012-2021.
80. S. Jaenicke, et al., *Field-induced structural changes in adsorbed layers of polar molecules studied by photon-stimulated desorption.* Journal De Physique, 1988. **49**(C6, Int. Field Emiss. Symp., 35th, 1988): p. 191-196.
81. A. Stintz and J. A. Panitz, *Isothermal ramped field-desorption of water from metal surfaces.* Journal of Applied Physics, 1992. **72**(2): p. 741-5.
82. A. Stintz and J. A. Panitz, *Cluster ion formation in isothermal ramped field-desorption of amorphous water ice from metal surfaces.* Surface Science, 1993. **296**(1): p. 75-86.
83. A. Stintz and J. A. Panitz, *Negative cluster ion formation from water ice in high electric fields.* International Journal of Mass Spectrometry and Ion Processes, 1994. **133**(1): p. 59-64.
84. N. Ernst, et al., *Field ion spectroscopy of oscillating surface reactions: H_2 / O_2 and H_2 / H_2O on platinum.* International Journal of Mass Spectrometry and Ion Processes, 1996. **152**: p. 2-3.

85. V. Gorodetskii, et al., *Field-induced oxygen layer formation from H2O and its titration by hydrogen on a Pt emitter.* Appl. Surf. Sci, 1995. **87**(88): p. 151-8.
86. V. Gorodetskii, J. H. Block, and W. Drachsel, *Isothermal oscillations of the hydrogen-oxidation reaction on platinum: investigations in the field electron and field ion microscope.* Appl. Surf. Sci., 1994. **76-77**(1-4): p. 129-35.
87. N. Ernst, et al., *Oscillating hydrogen-water reactions on a platinum field emitter.* Surface Science, 1994. **318**(3).
88. J.H. Block and A.W. Czanderna, *Field ion mass spectroscopy applied to surface investigations*, in *Methods of Surface Science*, A.W. Czanderna, Editor. 1975, Elsevier scientific publishing company: Amsterdam. p. 379-446.
89. J.H. Block, *Chemical surface reaction in the presence of high electric fields*, in *Chemistry and physics of solid surfaces*, R. Vanselow and S.Y. Tong, Editors. 1977, CRC Press: Cleveland, OH. p. 49-72.
90. D.L. Cocke and J.H. Block, *Field ion and field desorption mass spectrometry of inorganic compounds.* Surface Science, 1978. **70**: p. 363-391.
91. N. Ernst, G. Bozdech, and J. H. Block, *Critical energy deficits during the field ionization and proton capture of noble gases at rhodium and tungsten field emitters.* Int. J. Mass Spectrom. Ion Phys., 1978. **28**(1): p. 33-48.
92. N. Ernst, G. Bozdech, and J. H. Block, *The interaction of molecules with field emitter surfaces studied by field ion appearance spectroscopy.* Ber. Bunsenges. Phys. Chem., 1978. **82**(7): p. 756-66.
93. S. Jaenicke, et al., *Field-assisted photodesorption of ions from metal and semiconductor surfaces.* Journal De Physique, 1986. **47**(Colloque C7): p. 343-347.
94. J. Dirks, W. Drachsel, and J. H. Block, *Photon induced field desorption of water clusters.* Journal de Physique, 1989. **50**(Colloque C8): p. 153-158.
95. B. Sieben, G. Bozdech, and N. Ernst, *Energy resolved field ion spectroscopy of surface reactions: H/sub 2//O/sub 2/ and H/sub 2//H/sub 2/O on platinum.* Journal de Physique IV, 1996. **6**: p. C5-5.
96. D.L. Scovell, et al., *The dielectric response of water in high electric fields: equilibrium water thickness and the field distribution.* Chemical Physics Letters, 1998. **294**: p. 255-261.
97. D.L. Scovell, et al., *Phase transitions in vapor deposited water under the influence of high surface electric fields.* Surface Science, 2000. **457**(3): p. 365-376.
98. T.D. Pinkerton, et al., *Electric Field Effects in Ionization of Water - Ice Layers on Platinum.* Langmuir, 1999. **15**(3): p. 851-856.
99. G. Klesper and F. W. Rollgen, *On the field ionization behavior of cyclohexane on Pt tips.* Surface Science, 1999. **422**: p. 107-117.

100. G. Klesper and F. W. Rollgen, *Field ionization behavior of cyclohexane on Au tips.* International Journal of Mass Spectrometry, 1999. **185/186/187**: p. 189-194.
101. G.F. Rempfer, *Unipotential electrostatic lenses: paraxial properties and aberrations of focal length and focal point.* Journal of Applied Physics, 1985. **57**(7): p. 385-401.
102. M.q Kato and T. Katsushige, *Numerical analysis of trajectories and aberrations of a Wien filter including the effect of fringing fields.* Nuclear Instruments and Methods in Physics Research A, 1990. **298**: p. 296-320.
103. T.D. Pinkerton, *Fundamental Studies of the Effect of Electric Fields on Water-Surface Chemistry*. 1998, Ph.D. Thesis, Department of Chemical Engineering, University of Washington: Seattle. p. 140,
104. D. Eisenberg and W. Kauzmann, *The structures and properties of water*. 1969, New York and Oxford: Oxford University Press.
105. J. Jeans, *The Mathematical Theory of Electricity and Magnetism*. 1966, Cambridge: University Press.
106. Christopher J. Rothfuss, Valentin K. Medvedev, and Eric M. Stuve, *Temperature and field dependence of protonated water cluster emission from field adsorbed water layers on platinum.* Surface Science, 2002. **501**(3): p. 169-181.
107. Geoffrey Taylor, *Disintegration of water drops in an electric field.* Proceedings of the Royal Society of London, 1964. **A 280**(1382): p. 383.
108. M. F. Kropman and H. J. Bakker, *Dynamics of Water Molecules in Aqueous Solvation Shells.* Science, 2001. **291**(16 March): p. 2118-2120.
109. K. Franaszczuk, et al., *A comparison of electrochemical and gas-phase decomposition of methanol on platinum surfaces.* Journal of Physical Chemistry, 1992. **96**: p. 8509-8516.
110. Teresa Iwasita, *Fuel Cells: Spectroscopic Studies in the Electrocatalysis of Alcohol Oxidation.* Journal of the Brazilian Chemical Society, 2002. **13**(4): p. 401-409.
111. B. A. Sexton, K. D. Rendulic, and A. E. Hughes, *Decomposition Pathways of C1-C4 Alcohols Adsorbed on Platinum(111).* Surface Science, 1982. **121**: p. 181-198.
112. Richard M. Felder and Ronald W. Rousseau, *Elementary Principles of Chemical Processes*. 1986, New York: John Wiley & Sons.
113. G. Raina and G. U. Kulkarni, *A molecular beam study of water-methanol clusters.* Chemical Physics Letters, 2001. **337**: p. 269-276.
114. Seungdoo Park, et al., *Direct oxidation of hydrocarbons in a solid oxide fuel cell*
I. Methane Oxidation. Journal of The Electrochemical Society, 1999. **146**(10): p. 3603-3605.
115. Seungdoo Park, John M. Vohs, and Raymond J. Gorte, *Direct oxidation of hydrocarbons in a solid-oxide fuel cell.* Nature, 2000. **404**: p. 265-266.

116. Seungdoo Park, Raymond J. Gorte, and John M. Vohs, *Tape Cast Solid Oxide Fuel Cells for the Direct Oxidation of Hydrocarbons.* Journal of The Electrochemical Society, 2001. **148**(5): p. A443-A447.
117. M. J. Weaver, *Some dielectric solvation effects on the energetics of electrified metal interfaces and related molecular systems.* International Journal of Mass Spectrometry, 1999. **182/183**: p. 403-414.
118. I Villegas and M. J. Weaver, *Infrared spectroscopy of model electrochemical interfaces in ultrahigh vacuum: Surface-cation solvation in the Pt (111) / K^+ - methanol system.* Journal of Chemical Physics, 1995. **103**(6): p. 2295-2307.
119. M. J. Weaver, *Binding sites and vibrational frequencies for dilute carbon monoxide and nitric oxide adlayers in electrochemical versus ultrahigh-vacuum environments: the roles of double-layer solvation.* Surface Science, 1999. **437**: p. 215-230.
120. N. Chen, P. Blowers, and R. I. Masel, *Formation of hydronium and water-hydronium complexes during coadsorption of hydrogen and water on (2 x 1) Pt (110).* Surface Science, 1999. **419**: p. 150-157.

VITA

Christopher Rothfuss was born in Ann Arbor, Michigan in 1972. He lived in Marquette, Michigan until 1985 when he moved to Casper, Wyoming with his family. Chris graduated from Natrona County High School in Casper, and then attended the University of Wyoming where he received a Bachelor of Arts degree in International Studies in 1994 and a Master of Science degree in Chemical Engineering in 1996 under Dr. Chang-Yul Cha. Chris met his wife, Heather while at the University of Wyoming. In 2002 Christopher earned a Doctor of Philosophy in Chemical Engineering from the University of Washington.